

Preparation and properties of high dose nitrogen implanted epitaxially grown gadolinium oxide on silicon

Von der Fakultät für Elektrotechnik und Informatik der Gottfried Wilhelm Leibniz Universität Hannover
zur Erlangung des akademischen Grades

Doktor-Ingenieurin

Dr. –Ing.

genehmigte Dissertation

von

MSc. Anit Joseph

geboren am 27.05.1989

in Thrissur, Kerala-India

2017

Referent: Prof. Dr. H. Jörg Osten

Korreferenten : Prof. Dr. Tobias F. Wietler

Prof. Dr. Jan Schmidt

Tag der Promotion: 22.02.2017

Kurzfassung

Während sowohl Gadoliniumoxid (Gd_2O_3) als auch Gadoliniumnitrid (GdN) bereits umfangreich untersucht wurden, stellt sich die Frage nach dem Übergang zwischen beiden Materialien, also der Herstellung und Untersuchung von Gadoliniumoxynitriden. In dieser Arbeit wurden die folgenden Ansätze zum Stickstoffeinbau in epitaktisch gewachsenes Gadoliniumoxid auf Si (111)-Substraten untersucht:

- Epitaktisches Wachstum in Distickstoffmonoxid (N_2O)-Atmosphäre
- Verwendung von Stickstoff- oder N_2O -Plasma während des Wachstums
- Behandlung der epitaktischen Gd_2O_3 -Schicht mit aktiviertem NH_3
- Stickstoff-Ionenimplantation

Unter Verwendung der ersten drei Methoden war es nicht möglich, erhebliche Mengen an Stickstoff in die Gd_2O_3 -Schichten einzubauen. Der Stickstoffeinbau mit Hilfe der Ionenimplantation stellte sich als die vielversprechendste Methode heraus. Aus diesem Grund wurden die Vor- und Nachteile von Stickstoffeinbau über Ionenimplantation bei hohen Dosen in epitaktische Gd_2O_3 -Filme auf Si (111)-Substraten mit anschließendem Tempern im Detail untersucht. Der Stickstoffgehalt in den Oxidschichten wurde über eine Änderung der Implantationsdosis variiert. Der Einfluss des Stickstoffeinbaus auf die Gd-O-Bindung wird mittels Röntgen-Photoelektronenspektroskopie untersucht, welche deutlich auf das Vorhandensein von Stickstoff in der Schicht hinweist. Augerelekttronenspektroskopie-Tiefenprofile zeigen eine Maximalkonzentration von 11% Stickstoff für die höchste Implantationsdosis. Die Ramanspektroskopie zeigt starke Strukturänderungen. Die neu entstehende Struktur ist kristallin, aber weder in Übereinstimmung mit der bekannten *bixbyite-Struktur* des Gd_2O_3 noch mit der *rocksalt-Struktur* des GdN . Untersuchungen mit Elektronenmikroskopie zeigen die Formierung von Rissen und Bereichen geringerer Dichte bis hin zu Hohlräumen. Diese Struktur besitzt Ähnlichkeiten mit Transmissions-elektronenmikroskopaufnahmen von GdN -Schichten. Die Bandlücke von Gd_2O_3 , die über O1s Plasmonen-Energieverlustmessungen bestimmt wurden, wird durch den Einbau von Stickstoff signifikant reduziert. Die Reduzierung im Valenz- und Leitungsbandoffset wird als Funktion der Implantationsdosis ermittelt.

Abstract

Having both, well-explored gadolinium oxide (Gd_2O_3) and gadolinium nitride (GdN), questions arise about the transition between them, i.e. the possibility to fabricate and the properties of gadolinium oxynitrides. In this work, the following approaches for incorporating nitrogen into epitaxially grown Gd_2O_3 on Si (111) substrates were investigated:

- Epitaxial growth in a N_2O gas ambient
- Use of nitrogen or N_2O plasma during growth
- Exposure of the epitaxial Gd_2O_3 layer to activated NH_3
- Nitrogen ion implantation

Using the first three methods, it was not possible to incorporate substantial amounts of nitrogen into the Gd_2O_3 layers. Nitrogen incorporation by ion implantation turned out to be the most promising method. For this reason, the properties and drawbacks of nitrogen incorporation by high-dose ion implantation in epitaxial Gd_2O_3 films on Si (111) followed by annealing have been investigated in detail. The nitrogen content in the oxide layer has been altered by changing the implantation dose. The impact of nitrogen incorporation on Gd-O bonding is studied using X-ray photoelectron spectroscopy which clearly indicates the presence of nitrogen in the layer. Auger electron depth profiles reveal a peak nitrogen concentration of 11% for the highest implantation dose. Raman spectroscopy reveals heavy structural changes. The newly appearing structure is crystalline, but not in agreement with either the known *bixbyite* (Gd_2O_3) or *rocksalt* (GdN) structure. Electron microscopic investigations reveal the formation of cracks and small areas with lower densities or even voids. That structure exhibits similarities with transmission electron microscopy images of gadolinium nitride (GdN) layers. The electronic band gap of Gd_2O_3 estimated from O1s plasmon energy loss measurements was found to decrease significantly by the incorporation of nitrogen. Reduction in the valence band and conduction band offset is obtained as a function of implantation dose.

Keywords: Nitridation, Gadolinium oxide (Gd_2O_3), nitride and oxynitride, ion implantation

Schlagwörter: Nitridierung, Gadoliniumoxid (Gd_2O_3), Nitrid und Oxynitrid, Ionenimplantation

Table of Contents

| | |
|---|-----------|
| 1 Introduction..... | 5 |
| 2 Rare Earth- Oxides, Nitrides and Oxynitrides..... | 9 |
| 2.1 Rare earth oxide-Gd ₂ O ₃ | 9 |
| 2.2 Rare earth nitrides- GdN..... | 13 |
| 2.3 Rare earth oxynitrides- Gd _x O _y N _z | 16 |
| 3 Characterization Techniques..... | 17 |
| 3.1 X-ray diffraction..... | 17 |
| 3.2 X-ray photoelectron spectroscopy..... | 23 |
| 3.3 Auger electron spectroscopy..... | 25 |
| 3.4 Raman Spectroscopy..... | 27 |
| 3.5 Transmission electron microscopy..... | 29 |
| 3.6 Atomic force microscopy..... | 32 |
| 4 Epitaxial growth of Gd₂O₃ layers..... | 34 |
| 4.1 Molecular Beam Epitaxy- DCA S 1000..... | 37 |
| 4.2 Gd ₂ O ₃ epitaxy on silicon..... | 41 |
| 4.3 Sample preparation..... | 42 |
| 4.4 Results..... | 43 |
| 5 Nitridation of epitaxial Gd₂O₃ films..... | 47 |

| | |
|---|-----------|
| 5.1 Growth in a N ₂ O gas ambient..... | 48 |
| 5.1.1 Sample preparation..... | 49 |
| 5.1.2 Results..... | 50 |
| 5.2 Nitrogen and N ₂ O plasma during growth..... | 56 |
| 5.2.1 Sample preparation..... | 58 |
| 5.2.2 Results..... | 59 |
| 5.3 Exposure to activated NH ₃ | 63 |
| 5.3.1 Sample preparation..... | 63 |
| 5.3.2 Results..... | 64 |
| 5.4 Discussion | 68 |
| 6 Ion implantation into epitaxial Gd₂O₃ films..... | 73 |
| 6.1 Ion implantation process..... | 74 |
| 6.1.1 Implantation parameters..... | 77 |
| 6.1.2 Process flow..... | 81 |
| 6.1.3 Reactive ion etching..... | 83 |
| 6.1.4 Rapid thermal annealing | 84 |
| 6.2 Characterization of N- implanted Gd ₂ O ₃ layers..... | 84 |
| 6.2.1 Structural evolution..... | 85 |
| 6.2.2 XPS results..... | 90 |

| | |
|---------------------------------------|------------|
| 6.2.3 Band structure..... | 92 |
| 6.2.4 Gd, O and N concentration | 94 |
| 6.3 Summary..... | 97 |
| 7 Summary and outlook..... | 99 |
| References..... | 101 |
| Publications..... | 115 |
| Acknowledgements..... | 116 |

List of abbreviations

| | |
|-------|--|
| AES | Auger Electron Spectroscopy |
| AFM | Atomic Force Microscopy |
| BE | Binding Energy |
| BF | Bright Field |
| CCD | Charge- Coupled Device |
| CDC | Central distribution Chamber |
| CET | Capacitor Equivalent Thickness |
| CMOS | Complementary Metal Oxide Semiconductor |
| DF | Dark Field |
| DRAM | Dynamic Random Access Memory |
| EELS | Electron Energy Loss Spectroscopy |
| EOT | Effective Oxide Thickness |
| ESCA | Electron Spectroscopy for Chemical Analysis |
| FCC | Face Centered Cubic |
| FW | Frank- van-der Merwe mode |
| HBM | High Brightness Mode |
| HBT | Heterojunction Bipolar Transistor |
| HF | Hydrofluoric acid |
| HRTEM | High Resolution Transmission Electron Microscopy |
| LBM | Low Brightness Mode |

| | |
|--------|---|
| LD | Laser Diode |
| LED | Light Emitting Diode |
| MBE | Molecular Beam Epitaxy |
| MESFET | Metal Semiconductor Field Effect Transistor |
| MNOS | Metal-Nitride-Oxide-Silicon |
| MOS | Metal Oxide Semiconductor |
| MOSFET | Metal Oxide Semiconductor Field Effect Transistor |
| NIMS | National Institute of Material Science |
| ON | Oxide - Nitride |
| ONO | Oxide- Nitride- Oxide |
| PD | Photo Detector |
| PECVD | Plasma Enhanced Chemical Vapor Deposition |
| PHEMT | Pseudomorphic High Electron Mobility Transistor |
| PIII | Plasma Immersion Ion Implantation |
| RCA | Radio Corporation of America |
| REO | Rare Earth Oxides |
| RES | Rare Earth Sesquioxides |
| RF | Radio Frequency |
| RGA | Residual Gas Analyzer |
| RHEED | Reflection High Energy Electron Diffraction |
| RIE | Reactive Ion Etching |

| | |
|------|--------------------------------------|
| RMS | Root Mean Square |
| RRAM | Resistive Random Access Memory |
| RTA | Rapid Thermal Annealing |
| SK | Stranski Krastanov |
| SPM | Scanning Probe Microscopy |
| SRIM | Stopping and Range of Ions in Matter |
| TED | Transient Enhanced Diffusion |
| TEM | Transmission Electron Microscopy |
| TRIM | Transport of Ions in Matter |
| UHV | Ultra High Vacuum |
| VB | Valence Band |
| VBM | Valence Band Maximum |
| VLSI | Very Large Scale Industry |
| VW | Volmer-Weber |
| Vos | Oxygen Vacancies |
| XPS | X-ray Photoelectron Spectroscopy |
| XRD | X-ray Diffraction |
| XRR | X-ray Reflectometry |



1 Introduction

Over the past half century the economics of the semiconductor industry have been driven by the principle of Moore's law. [1] The very authentic trend of doubling the number of devices per unit area biannually, first proposed by Gordon Moore in 1965, has perpetuated steadily through micron to nanometer scale and hope it will continue very soon to angstrom scale. Keeping in mind the end goal to proceed with device scaling to the 45nm and below, semiconductor device makers have implemented high-k materials. [2] Logic circuits in microprocessors, computers, tablets, cell phones, memory technologies like resistive random access memory (RRAM), have also migrated to high-k dielectrics. [3, 4] High-k dielectrics refers to a class of simple binary and ternary metal oxide insulators with a relative dielectric constant greater than about 9 and comprising transition metals from groups III-V the lanthanides and aluminium (Al). The main motivation for the migration to high-k materials was to continue scaling the effective oxide thickness (EOT) of devices while maintaining a low leakage current. [5]

Rare-earth oxides (REO) form a very interesting group of insulators for epitaxial growth on silicon. It is extremely important and desirable to integrate these highly functional metal oxides into mature semiconductor technology. In particular, epitaxial growth of gadolinium oxide on silicon with the Gd_2O_3 stoichiometry in the cubic *bixbyite* structure has been investigated in great detail. [6] This material has a large band gap of about 6 eV and nearly symmetrical band offsets as well as a low lattice mismatch of about -0.4 % to Si. [7] Layers grown by an optimized process can display a sufficiently high-k value to achieve equivalent oxide thickness values below 1 nm, combined with ultra-low leakage current densities, good reliability, and high electrical breakdown voltages. A variety of metal oxide semiconductor (MOS) devices has been fabricated based on such layers. [8]

Generally, metal oxides grown on Si often exhibit poor electrical properties, such as instability in the threshold voltage, high leakage current density and poor reliability. [9, 10] The most common electrically active defects are found to be the omnipresent oxygen vacancies (V_{Os}). In case of various high-k oxides (e.g. HfO_2 , ZrO_2 , etc.) it is reported that the presence of V_{Os} gives rise to degradation of the electrical properties by inducing localized energy states within the band gap. [11] Recent studies demonstrated that the incorporation of nitrogen into the high-k dielectric interface with the Si substrate could be very effective in suppressing crystallization of

metal oxide, [12] decreasing dopant penetration into bulk Si, [13] inhibiting interfacial reaction with the Si substrate, [14] and also improving the electrical performance of the devices. [15–17] It is reported that the improvement in the electrical properties of various oxides is due to the reduction in V_{Os} caused by the incorporation of nitrogen. [18–20] It is important to consider that the nitrogen incorporation can also influence the electrical properties of high-k oxides by changing their electronic structure resulting in the reduction of band gap and the valence band (VB) offset with Si. [21] Also, photoemission investigations show nitrogen incorporation to be a reason for the reduction in both VB offset and conduction band offset of HfSiON gate dielectrics. [16]

On the other hand, rare-earth nitrides have also been studied for a long time, but only recently it became possible to establish their properties confidently. This group of materials exhibits a versatile set of properties, which in turn have a potentially wide range of applications including electronics, optoelectronics and spintronics. Gadolinium nitride (GdN) is the most thoroughly studied candidate. [22] This material crystallizes in the cubic *rocksalt* structure, displaying a lattice mismatch of $\sim 7.5\%$ to silicon. Recent measurements indicate that GdN is ferromagnetic with a Curie temperature of 69 K. The band gap is 1.3 eV in the paramagnetic phase and redshifts to 0.9 eV in the spin-split bands below the Curie temperature. [23]

Having both, well-explored gadolinium oxide and nitride, questions arise about the transition between both, i.e. the properties of gadolinium oxynitrides. It has been shown that epitaxial Gd_2O_3 films grown on Si can be improved significantly by incorporation of a small amount of nitrogen. [21] In addition, there are some results about the incorporation of small amounts of oxygen ($< 5\%$) into gadolinium nitride. Oxygen substitution leads to the incorporation of additional electrons, causing paramagnetism and short-range antiferromagnetic order. [24]

Not much is known about gadolinium oxynitrides with comparable O and N concentrations. It is reported that the solubility limit of GdO in GdN depends on the preparation temperature, but can be up to $GdN_{0.65}O_{0.35}$. In a recent paper, Wang et al. [25] demonstrated nitrogen plasma immersion ion implantation into gadolinium oxide. However, the authors did not give any evidence about the composition of the formed ternary $Gd_xO_yN_z$ layer.

In this dissertation, I attempt to fabricate and characterize gadolinium oxynitride layers with similar O and N concentrations using various growth techniques as well as post-grow processing

steps like annealing in different ambient and high-dose nitrogen implantation into crystalline Gd_2O_3 layers.

In chapter 2, I summarize the relevant knowledge about rare earth oxides and rare earth nitrides and at the same time more specific about Gd_2O_3 and GdN . Chapter 3 reviews the different characterization techniques used in my investigation. That chapter is followed by a description of the epitaxial growth of Gd_2O_3 layers using molecular beam epitaxy (MBE). Then I summarize the different approaches used for nitridation of epitaxial Gd_2O_3 films (chapter 5). In the earlier reports about the effect of nitrogen doping on the electrical properties of epitaxial Gd_2O_3 thin films, the authors grew epitaxial Gd_2O_3 :N thin films on Si (111) substrates by solid source MBE using nitrous oxide as the nitridation agent which resulted in substantial reduction of the leakage current density and disappearance of hysteresis in capacitance-voltage characteristics. They also claimed that nitrogen incorporation in Gd_2O_3 effectively eliminates the adverse effects of the oxygen vacancy induced defects in the oxide layer. [26] The same idea was used for the preparation of nitrogen rich Gd_2O_3 layers or an oxynitride layer described in detail in chapter 5.

Sen et al. [27] reported the effect of nitrogen implantation on thin lanthanum oxide (La_2O_3) films grown by e-beam evaporation. The amount of nitrogen incorporated in the oxide film by Plasma immersion ion implantation is found to be quite low (3% near the surface) and they also published that the introduction of nitrogen atoms into the La_2O_3 network results in reduction in the oxide traps and enhancement in electrical properties. Since gadolinium also belongs to lanthanide series, the hope to form an oxynitride layer was immense.

The main aim of this work is to incorporate nitrogen into epitaxially grown Gd_2O_3 layer on silicon or in other words an oxynitride layer. It needs much effort. I tried four different methods to incorporate nitrogen into the oxide layer. Growth in a N_2O gas ambient, use of nitrogen and N_2O plasma during growth, exposure to activated NH_3 and nitrogen ion implantation are the four different nitridation processes studied in the framework of my PhD. The outcomes of all four methods were described in detail. The results were compared and chose the most promising method and discussed its drawbacks.

Out of these four methods nitrogen ion implantation seems to be most promising. Implantation dose and energy are the two important parameters for effective incorporation of nitrogen. The implantation parameters which were extracted using SRIM software were also described briefly

in chapter 6. Epitaxially grown Gd_2O_3 layer were subjected for different processing steps like capping with screening oxide (SiO_2), ion implantation process, removal of SiO_2 by reactive ion etching (RIE) method and post implantation annealing.

The curiosity to know more about gadolinium oxynitride layer i.e.; the transition between Gd_2O_3 and GdN was the real motivation behind this work. But incorporating nitrogen in an epitaxially grown Gd_2O_3 layer was really challenging which leads to try out different nitridation methods. The results of these methods will cover the last two chapters.

2 Rare Earth – Oxides, Nitrides, and Oxynitrides

2.1 Rare earth oxides - Gd_2O_3

Rare earth elements are a group of seventeen chemical elements. The group consists of yttrium and the 15 lanthanide elements (lanthanum, cerium, praseodymium, neodymium, promethium, samarium, europium, gadolinium, terbium, dysprosium, holmium, erbium, thulium, ytterbium, and lutetium). The International Union of Pure and Applied Chemistry include scandium in their rare earth element definition. The rare earth elements are all metals, and the group is often referred to as the "rare earth metals." The rare earth elements are often subdivided into "Heavy Rare Earths" and "Light Rare Earths." Lanthanum, cerium, praseodymium, neodymium, promethium and samarium are the "light rare earths." Yttrium, europium, gadolinium, terbium, dysprosium, holmium, erbium, thulium, ytterbium, and lutetium are the "heavy rare earths." Although yttrium is lighter than the light rare earth elements, it is included in the heavy rare earth group because of its chemical and physical associations with heavy rare earths in natural deposits. Rare earth metals and alloys that contain them are used in many devices that people use every day such as computer memory, DVDs, rechargeable batteries, cell phones, catalytic converters, magnets, fluorescent lighting and much more. [28] Most rare earth oxides are thermally stable, as well as chemically active. Oxidation states of rare earth ions in oxides can be understood in terms of reduction potentials. The rare earth oxides (REO) can have different oxygen compositions REO_x , with x ranging from 1 to 2 due to the multiple oxidation states (+2, +3, and +4) of the rare-earth metals. [6, 29] This leads to oxides with different stoichiometries (REO , RE_2O_3 , REO_2). All known RE (II) oxides, like EuO , are not insulating. Therefore, they will not be considered here any further. For application in a Si-based device fabrication process, all lanthanide oxides exhibiting more than one valence state (+3 and +4) are not the best choice as epitaxial high-k materials because of the coexistence of phases with different oxygen content. For example, cerium(IV) oxide (CeO_2) can release oxygen under reduction conditions forming a series of reduced oxides with stoichiometric cerium(III) oxide (Ce_2O_3) as an end product, which in its turn easily takes up oxygen under oxidizing conditions, turning the cerium(III) oxide back into CeO_2 . In addition, stable mixed valence-state structures can occur for some REO's. For example, the mixed valence-state Pr_6O_{11} is the most stable phase for praseodymium oxide. For those highly ionic oxides, the position of the charge neutrality level depends strongly on the

stoichiometry. [30] Thus, also the band alignment to silicon and, finally, the leakage behavior become strongly dependent on the oxygen content. All rare earth oxides displaying only one valence state are easier to handle due to the absence of transitions between phases with different oxygen content. Based on that argument, we will focus our discussion mainly on RE (III) oxides (occurring as RE₂O₃). These so-called *sesquioxides* RE₂O₃ exist for all rare earth ions. [31]

The RE₂O₃ oxides can occur in different structural phases, [32] like the manganese oxide (Mn₂O₃) or *bixbyite* structure. Some of these oxides also crystallize in the hexagonal lanthanum oxide structure, which is suitable for epitaxy only on Si (111). Also, monoclinic phases are known for various RE (III) oxides. Different crystallographic structures are accompanied by different properties. Several rare earth oxides can undergo structural phase transformation within a temperature range, typical for complementary metal oxide semiconductor (CMOS) processing (see Figure 2.1); these oxides are not very well suited for technological applications.

Lighter rare earth ions, from La³⁺ to Nd³⁺ give A-form (hexagonal). These ions have happened to be seen to form the C-type (cubic) structure, but this observation seems to be due to impurity stabilization or a metastable phase. An example of the B-type (monoclinic) oxide is given by Sm₂O₃. Other rare earth sesquioxides yield the C-type oxides. [33–36]

Due to high direct tunneling current, [37] silicon dioxide thinner than 1.5 nm cannot be used for the gate dielectric of CMOS devices. [38] High-dielectric-constant oxides offer an alternative to SiO₂ in very-large-scale integrated (VLSI) devices. The basic concept for using high dielectric-constant materials is increasing the film thickness to reduce the tunneling leakage current and improve the reliability while scaling the capacitance equivalent oxide thickness (CET) below the direct tunneling limit of SiO₂. [39] Rare earth oxides have received much attention due to their many advantages: high dielectric constant, [40–42] sufficiently high breakdown strength, extremely low leakage current, and well-behaved interface properties. Rare earth oxides, [43, 44] such as La₂O₃, [45] and Gd₂O₃ [6, 46], have been studied in detail. There are also reports about the dielectric properties of Pr₂O₃, [47] Er₂O₃, [48] Sm₂O₃, [49] Lu₂O₃, [50] and Sc₂O₃. [51]

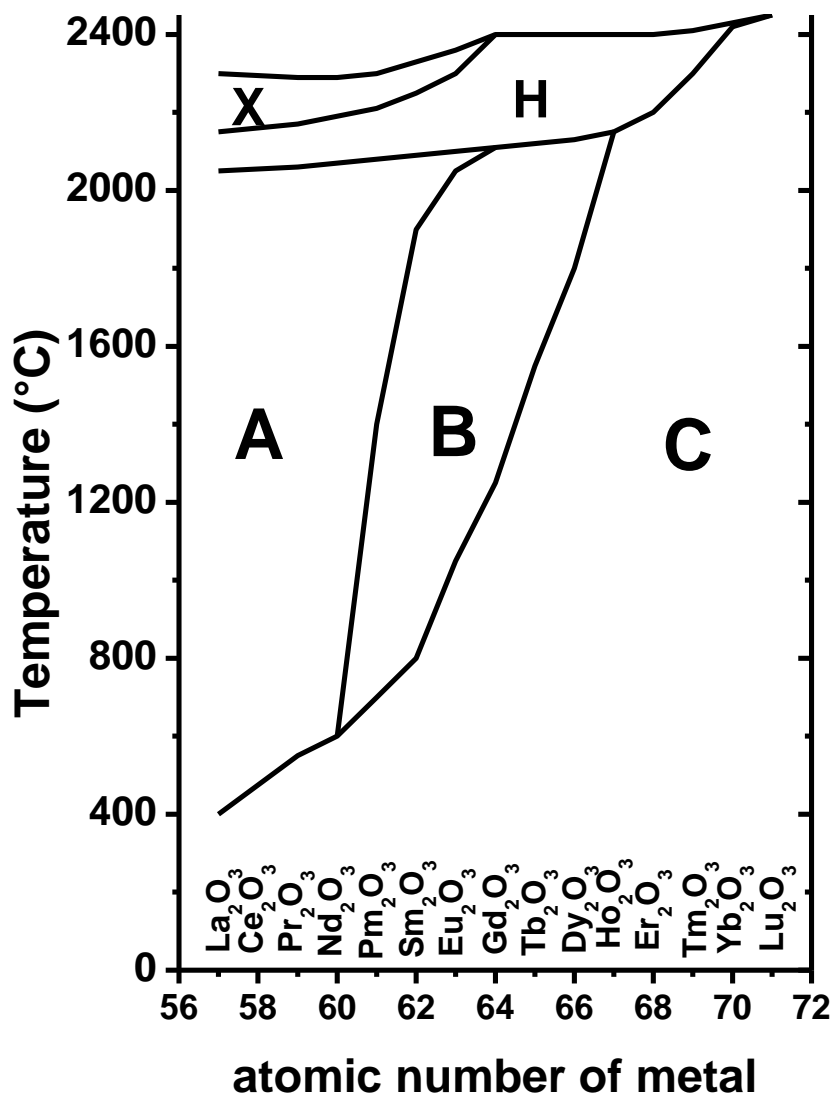


Fig. 2.1: Structural phase transitions in lanthanide oxides (based on Ref. [32])

A: hexagonal, B: monoclinic, C: cubic

H, X high-T modifications

Gadolinium Oxide (Gd₂O₃)

Gadolinium oxide is an inorganic compound with the formula Gd₂O₃. Gadolinium oxide adopts three structures. They are cubic, hexagonal and monoclinic structures. At room temperature, the cubic structure is more stable. Above 2100 °C to the melting point at 2420 °C, a hexagonal phase dominates. The cubic structure features two types of gadolinium sites, each with a coordination number of 6 but with different coordination geometries. [35]

Epitaxial growth of crystalline Gd₂O₃ on silicon in the cubic *bixbyite* structure has been widely investigated. [6] This material has a large band gap of about 6 eV and nearly symmetrical band offsets as well as a low lattice mismatch of about -0.4 % to Si. [7] Layers grown by an optimized process can display a sufficiently high-k value to achieve equivalent oxide thickness values below 1 nm, combined with ultra-low leakage current densities, good reliability, and high electrical breakdown voltages. A variety of MOS devices has been fabricated based on these layers. [8]

Additionally, the high refractive indices lead to applications in optics, such as antireflection coatings, switches, filters and modulators. [52, 53] Semicore f-levels determines many properties of rare-earth *sesquioxides*. It is reported that rare-earth atoms are usually not participating in bonding and electronic conduction while being localized, f-shell electrons are available for optical transition and can establish strong magnetic order. [52] The lattice constant of cubic Gd₂O₃ is reported as 10.8 Å (a=b=c). [55] A. Laha et al. [54] reported that Pt/Gd₂O₃/Si (111) and Pt/Gd₂O₃/Si (110) metal oxide semiconductor heterostructures show promising electrical properties and hence, could be considered for future generation of complementary metal oxide semiconductor devices. The obtained values for capacitance equivalent oxide thicknesses estimated from capacitance versus voltage characteristics are 0.97, 1.12, and 0.93 nm for the films grown on Si (001), Si (111), and Si (110) substrates, respectively. They also reported that the films exhibit good insulating properties with leakage current densities of 0.4, 0.5, and 4.5 mA/cm² respectively.

2.2 Rare earth nitrides-GdN

The rare-earth mononitrides were first investigated in the 1960s. Currently, the field of research into the rare earth nitrides (RENs) is becoming quickly, roused by the materials requests of proposed electronic and spintronic devices. Both semiconducting and ferromagnetic properties have been established in some of the RENs which thus attract interest for the potential to exploit the spin of charge carriers in semiconductor technologies for both fundamental and applied science. The present enthusiasm for the capability of spintronic devices has raised the level of direness in the investigation of intrinsic ferromagnetic semiconductors, of which the RENs offer a rich arrangement of illustrations. However their potential has been ineffectively investigated up to this point, regardless of EuO having turned into an outstanding intrinsic magnetic semiconductor. [56] The RENs form in the face-centered (FCC) cubic *rocksalt* structure with lattice constants ranging from 5.305 Å for LaN to 4.76 Å for LuN, in total a 5% difference across the series and less than 0.5% between nitrides of neighboring atomic species. [56] One of the major hurdles in growing REN thin films, either epitaxial or in polycrystalline form, is their propensity to form nitrogen vacancies and to decompose in air into RE oxide/hydroxides. [57, 58] Each RE atom is coordinated by 6 nitrogen atoms and, conversely, each nitrogen atom is coordinated by 6 RE atoms. The extensive distinction in electronegativity between nitrogen (3.0) and RE (1.1–1.5) leads to a strong affinity and a dominatingly ionic character (more than 50%) of the RE-N bonds. [59] Regardless of endeavors to enhance crystal quality, just little is known about the basic defects in the RENs. This is fundamentally because of the instability of RENs in air which makes high resolution transmission electron microscopy challenging. In any case, for a portion of the RENs, for example, GdN, the oxidation rate is adequately moderate to permit cross-section scanning electron microscopy. [60, 61]

Gadolinium Nitride (GdN)

GdN, with its half-filled 4f shell, is by far the most thoroughly investigated of the RENs. It has the highest Curie temperature among the RENs, [62] with reports as high as 90 K. [63, 64] GdN is a soft ferromagnet, with the low temperature in-plane coercive fields of recent thin films reported as ranging from approximately 10–220 Oe. [65] GdN is considered as a ferromagnetic semiconductor where both semiconducting and ferromagnetic characteristics are exhibited simultaneously. [23] Very recently, it has been found that the temperature dependent optical and magnetic properties of thin GdN films show a red shift in both the majority and minority spin gaps; there is also a clear spin splitting in the band structure of GdN. These results demonstrate that GdN is an intrinsic ferromagnetic semiconductor. [66]

According to Trodahl et al. [23] the direct gap in GdN is seen at 1.3 eV (e.g. semiconducting) in the paramagnetic phase at 300 K, and on entering the ferromagnetic phase it falls to 0.9 eV. X-ray photoelectron spectroscopy (XPS) results by Leuenberger et al. [64] provided the first information about the filled states, locating the Gd 4f levels about 8 eV below the Fermi level.

However results demonstrate epitaxial GdN thin films grown by molecular beam epitaxy (MBE). [63] Considering the electronic properties of GdN, dozens of different publications have been presented over the years, disagreeing in most respects. In principle elastic neutron scattering in zero external field should solve the problem, but Gd has largest neutron absorption cross sections and no neutron scattering is possible. [67]

According to P. Wachter [68] stoichiometric GdN for temperatures near zero and magnetic fields toward zero (10 Oe) is an antiferromagnet, but becomes ferromagnetic above magnetic fields of about 3 kOe. He suggested that the correct term is metamagnetism and the electric behavior is metallic (semi metallic). Comparison between Gd_2O_3 and GdN is presented in table 2.1.

| Properties | Gadolinium Oxide (Gd₂O₃) | Gadolinium Nitride (GdN) |
|---------------------|---|-------------------------------------|
| Material type | Insulator | Semiconductor |
| Crystal structure | Cubic <i>bixbyite</i> | Cubic <i>rocksalt</i> |
| Lattice constant | 10.8 Å (cubic Gd ₂ O ₃) | 5.08 Å |
| Lattice mismatch | 0.5 % with Si | 7.5 % with Si |
| Band gap | 6 eV | 1.3 eV |
| Dielectric constant | 13.7 | 6.7 |
| Density | 7.407 g/cm ³ | 9.10 g/cm ³ |
| Refractive index | 1.8±0.1 | 2.0±0.1 |
| Mass | 362.50 g/mol | 171.927 g/mol |
| Melting point | 2420°C | 2900°C |
| Appearance and odor | White powder (odorless) | Black powder (slight ammonia odor) |

Table 2.1: Comparison of gadolinium oxide [Ref. 6, 7] and gadolinium nitride [Ref. 22, 23]

2.3 Rare earth oxynitrides-Gd_xO_yN_z

Recent studies demonstrated that the incorporation of nitrogen into the high-k dielectric film is a suitable solution for the previously stated problems. [15] Here is the importance of rare earth oxynitrides (REONs). Oxynitride thin films have been tested in a wide range of electronic, optoelectronic devices and gas sensors. For example silicon oxynitride is a very attractive material for integrated optics application, because of its excellent optical properties (optical loss below 0.2 dB/cm). [69]

Coming to the rare earth materials one of the key necessities for the high-k dielectric is thermal stability after a 1000°C rapid thermal annealing which is an irreplaceable procedure for source/channel dopant activation. Despite the fact that, the pseudo binary alloys meet a large number of the necessities for the advanced gate dielectric, the carrier mobility degradation and the degradation of transistor performance due to gate dielectric crystallization and metal penetration into the underlying channel are still significant concerns. [70, 71]

In addition to the general thoughts about REONs, there is also a reported work on samarium oxynitrides (prepared by heating mixtures of the oxide, nitride and metal in sealed tantalum tubes at 1280-1340°C) that provides evidence for a continuous range of oxygen solubility in the nitride. They reported a decrease in the lattice parameter of the oxynitride from 5.046 Å at the nitride to 4.978 Å at SmN_{0.5}O_{0.5}. [72] A more comprehensive study [24] revealed a linear decrease in the lattice parameter of GdN_xO_y with increase in $y/(x + y)$, leading to equilibrium mixtures of gadolinium metal and either GdN_{0.65}O_{0.35} ($a = 4.944$ Å) plus cubic Gd₂O₃ at 1200°C, or GdN_{0.72}O_{0.28} ($a = 4.952$ Å) plus monoclinic Gd₂O₃ at 1600°C. Ren et al. [73] reported gadolinium oxide resistive random access memory (RRAM) with nitrogen plasma immersion ion implantation (PIII) treatment technique which results in the formation of Gd_xO_yN_z layer by controlling the implantation voltage whereas the nitrogen ions exist near the surface of gadolinium oxide. They claimed that the nitrogen incorporation can reduce the leakage current to reach a low current and power consumption operation. In addition, the retention and endurance characteristics were also improved. It needs more research on gadolinium oxynitride layers in light of the fact that the stoichiometry and properties of the layers require more examination.

3 Characterization Techniques

To characterize nitrided epitaxially grown Gd_2O_3 on silicon, different techniques were used. This chapter describes the theoretical foundations of the characterization techniques used in this work, so that it makes easier access to the interpretation of the results described in chapters 5 and 6. Described here are the basic principles of measurement techniques, any additional information can be found in the cited literature.

3.1 X-ray Diffraction

The discovery of X-ray diffraction (XRD) by crystals was made in April 1912 in the Institute of Theoretical Physics at the University of Munich. The experiment was proposed by Max von Laue and performed by Walter Friedrich and Paul Knipping. [74] After the discovery of the diffraction of X-rays by crystals in 1912, W. L. Bragg derived his famous law, which relates the wavelength of X-rays to the glancing angle of reflection. In 1913 W. H. Bragg built the first X-ray spectrometer, which he initially used to study X-ray spectral distributions. Within several years they were able to use this instrument and Bragg's law to derive the structure of crystals and show the exact positions of atoms. Subsequently, they demonstrated that the properties and behavior of a large variety of substances can be related to the position of their constituent atoms. The mathematical form of Bragg's Law can be explained as:

$$n\lambda = 2d_{hkl} \cdot \sin\theta \quad (3.1)$$

where

- n is an integer determined by the order.
- λ is the wavelength of X-rays, and moving electrons, protons and neutrons.
- d_{hkl} is the spacing between the planes in the atomic lattice.
- θ is the angle between the incident ray and the scattering planes. [75]

The mathematical form of Bragg's law is represented schematically in figure 3.1. A diffraction pattern is obtained by measuring the intensity of scattered waves as a function of scattering angle. Very strong intensities known as Bragg peaks are obtained in the diffraction pattern when

scattered waves satisfy the Bragg's Law. For Gd_2O_3 with the cubic bixbyite structure (having lattice constants $a=b=c$), the interplanar spacing (d_{hkl}) rewrites as follows:

$$d_{hkl} = \frac{a}{\sqrt{h^2 + k^2 + l^2}} \quad (3.2)$$

Where h, k, l are miller indices.

When X-ray beams are shot through a crystal of the atom, the crystal causes the beam of X-ray to diffract in a predictable pattern based on their crystal lattice structure which resulted in a diffraction pattern. Diffracted photons can add and subtract, giving different areas of photon intensities. Because X-rays are bundles of separate waves, each wave can interact with one another either constructively or destructively. The interaction between waves is called interference. Constructive interference occurs when there is a collision of photons in a way that their intensities combine. If the waves are out of phase, then destructive interference occurs and the amplitude of the resultant wave will be reduced.

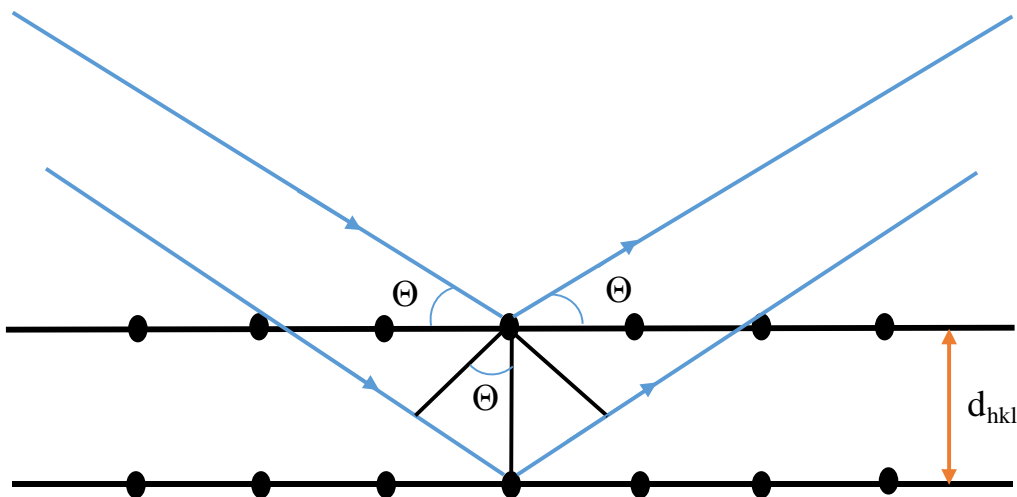


Fig. 3.1: Schematic representation of Bragg- condition for diffraction of X-rays.

3.1 X-ray diffraction

Let's assume that a single monochromatic wave (of any type) is incident on aligned planes of lattice points, with separation d , at angle θ . The difference in the optical path between the wave reflected on the upper and that reflected on the lower netplane is $2d \cdot \sin(\theta)$. Both waves undergo constructive interference, if and only if this path difference is equal to any integer value of the wavelength, i.e. $n \lambda = 2d \cdot \sin(\theta)$, which is Bragg's law.

All the X-ray measurement results presented in this thesis were measured using BRUCKER D8 DISCOVER XRD instrument shown in figure 3.2.

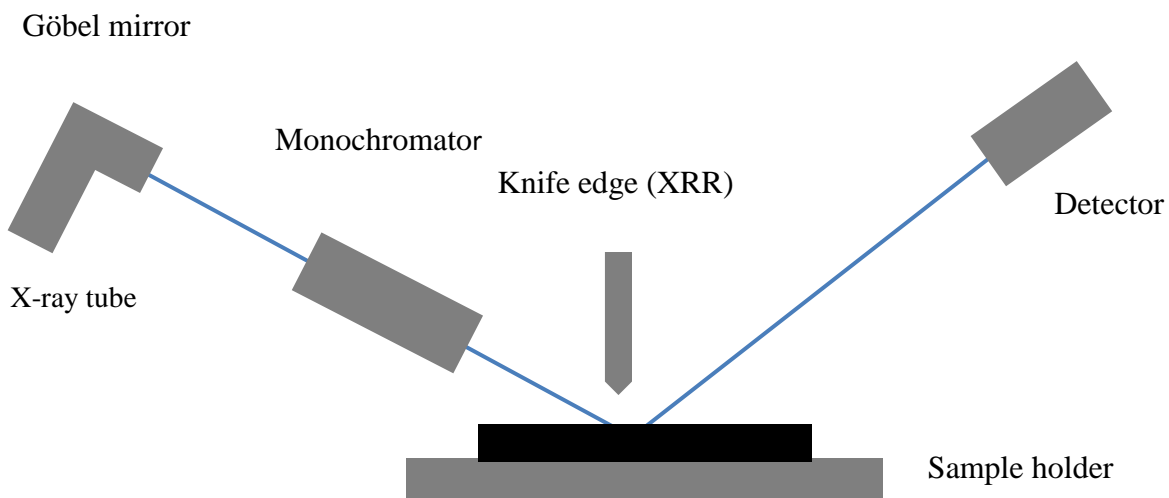


Fig. 3.2: Schematic representation of X-ray diffractometer

The basic parts of an X-ray diffractometer consists of an X-ray tube with copper anode and a Göbel mirror for line focus and an asymmetric monochromator. The detector can be operated with a variable slit and for X-ray reflectometry knife edge is available.

$\theta/2\theta$ - Measurement

$\theta/2\theta$ – Measurement can be explained on the basis that the scattered intensity relies on the distance from the sample to the detection system. We along these lines ought to design the instrument with the end goal that we can scan the space around the sample by keeping the sample–detector distance constant. This measure guarantees that any intensity variation observed is due to the interference function and is not caused by a dependency on sample–detector distance. The working principle of a $\theta/2\theta$ scan is depicted in figure 3.3 in the hemisphere of the sample reference frame.

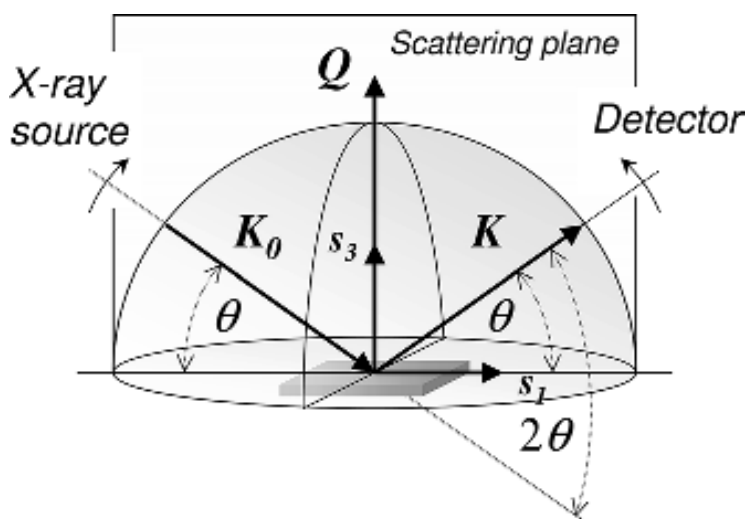


Fig. 3.3: Schematic representation of a $\theta/2\theta$ scan from the viewpoint of the sample reference frame. (From Ref. [76])

S_1 and S_3 - sample coordinate vectors

K_0 and K - scattering plane

Q - Scattering vector

The sample is placed in the center of the instrument and the X-ray beam is incident on the sample surface at an angle θ and the detector monitors the scattered radiation at the same angle. It can be simply said that throughout the scan the angle of the incident and exiting beam are continuously changed, but they remain same through the entire scan. The output or the variation of exit angle is determined with respect to the extended incident beam and this angle is 2θ . The results are

3.1 X-ray diffraction

commonly depicted as a component of $I(2\theta)$. In a $\theta/2\theta$ scan the scattering vector Q is always parallel to the substrate normal S_3 . [76] This gives the information about the quality of the material. The intensity of the peak is usually proportional to the thickness of the layers. The result of a $\theta/2\theta$ scan of a 19 nm thick Gd_2O_3 film on Si (111) is shown in figure 3.4. The measurement was done using the characteristic radiation of a copper x-ray tube having λ ($Cu\ K\alpha$) = 0.154 nm. Various interesting features are realized from this plot, which displays five Bragg reflections in the scattering angle range from 20° to 100° .

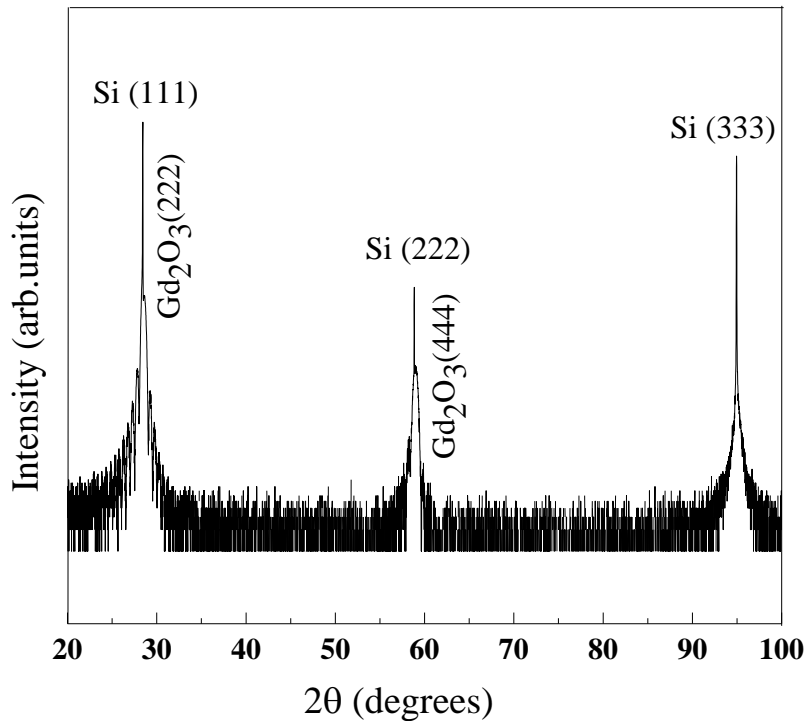


Fig. 3.4: X-ray diffraction result ($\theta/2\theta$ scan) of a 19 nm thin Gd_2O_3 film on Si (111) measured with $Cu\ K\alpha$ radiation

X-ray reflectometry

X-ray reflectometry (XRR), sometimes called grazing incidence X-ray reflectometry is basically used to measure thickness, density and roughness of layers on semiconductor substrates. It can be performed on both crystalline and amorphous materials. [77, 78] For angles larger than the critical angle, θ_c , regular fringes appear called Kiessig fringes from which the period

measurement allows the layer thickness determination. [79]The XRR strategy is not constrained by the degree of crystallinity of the materials under examination since it adequately gives a measure of density difference. In any case, the appropriateness of XRR is constrained, and thickness determination is impossible for films with rough interfaces or with a large thickness, as the X- ray beams are not reflected adequately. [80]

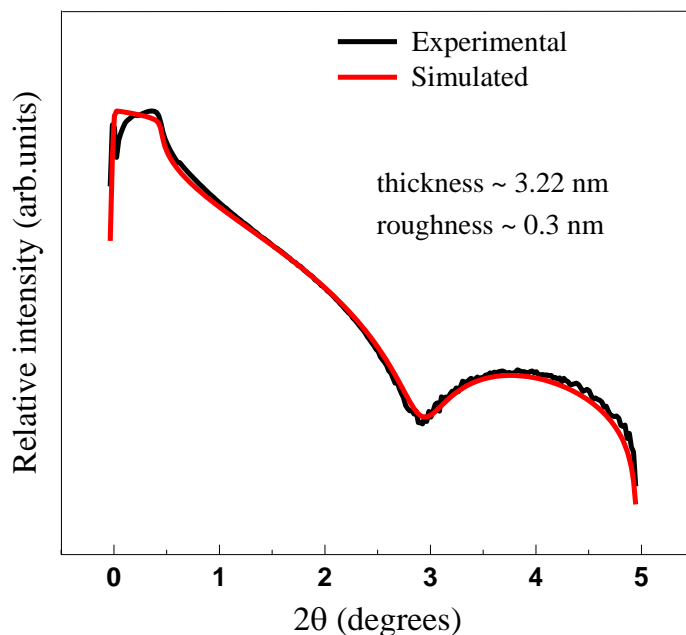


Fig. 3.5: Thickness measurement using X-ray reflectivity

The evaluation is carried out using the LEPTOS program from BRUKER, by generating a layered model and an associated simulation curve. Through different optimization algorithms the simulation curve approximates with the measurement curve which then obtain parameters such as layer thickness and roughness. The measurement curve and the corresponding simulated data of Gd_2O_3 layer on Si (111) is shown in figure 3.5 which yielded the parameters thickness and roughness of the layer.

3.2 X-ray Photoelectron Spectroscopy

In 1905 Albert Einstein published a paper that explained experimental data from the photoelectric effect as the result of light energy being carried in discrete quantized packets. This discovery led to the quantum revolution. The photoelectric effect refers to the emission, or ejection, of electrons from the surface of, generally, a metal in response to incident light. Energy contained within the incident light is absorbed by electrons within the metal, giving the electrons sufficient energy to be 'knocked' out of, that is, emitted from, the surface of the metal. Einstein described the photoelectric effect using a formula that relates the maximum kinetic energy (K_{\max}) of the photoelectrons to the energy of the absorbed photons (E) and the work function (ϕ) of the surface:

$$K_{\max} = E - \phi \quad (3.3)$$

The first term energy (E) of the absorbed photons can be rewrite with frequency (f) or wavelength (λ): [81]

$$E = hf = h(c/\lambda) \quad (3.4)$$

X-ray photoelectron spectroscopy (XPS) is an important and widely used surface analysis technique that operates on the principle of previously described photoelectric effect. In this process a primary excitation of electrons happened due to X-ray irradiation which ejects electrons (photoelectrons) of discrete energy, consists of chemical information regarding the surface analyte. In this emission process, an atom absorbs a photon of energy ($h\nu$) resulting in an ejection of a core level electron, which is detected and its energy measured. The energy level schematics for XPS binding energy measurements were depicted in figure 3.6. E_k^1 relative to the vacuum level, E_v . [82]

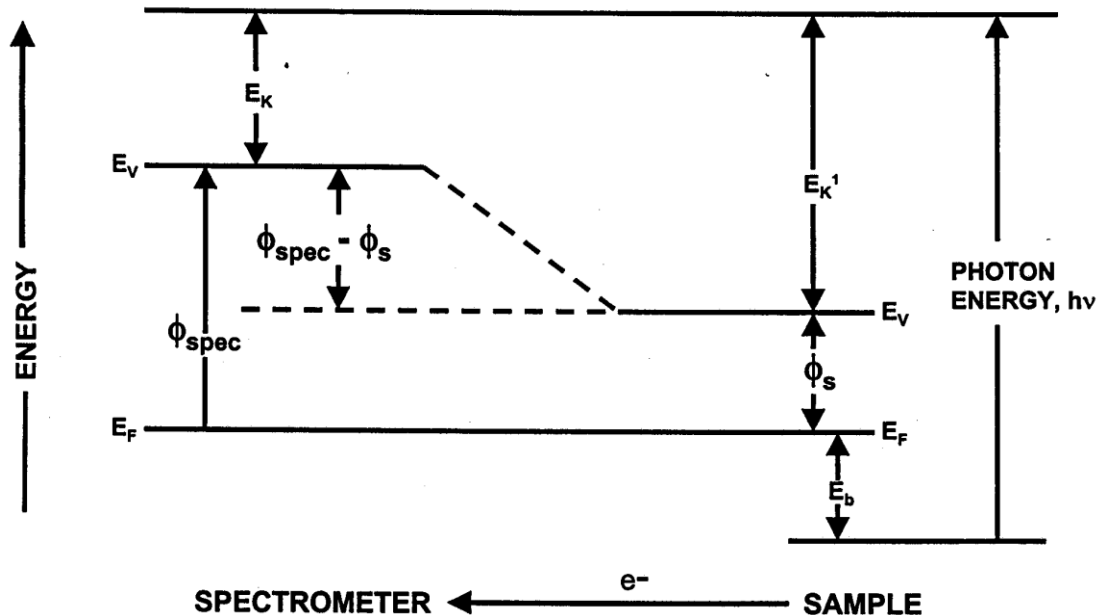


Fig. 3.6: Energy level schematic for XPS binding energy measurements (from Ref. [82])

- E_k^1 -Kinetic electron energy at the sample surface
- E_k - Kinetic energy of the electron
- E_b - Binding energy
- Φ_{spec} - Spectrometer work function
- Φ_s - Sample work function
- $E_k = E_k^1 - (\Phi_{\text{spec}} - \Phi_s)$
- $h\nu = E_b + E_k + \Phi_{\text{spec}}$

All XPS measurements in this work were done using the source Mg $K\alpha$ radiation ($h\nu = 1253.6$ eV) for the excitation of photoelectrons.

Chemical shift

It was discovered in the early 1920's that the wavelength of X-ray and the position of absorption edge depend on the chemical environment of the atom. [83] The chemical shift in X-ray absorption was first discovered on the observations made on chlorine by finding the position of X-ray absorption edge that depends on the chemical valence. [84] Surface charging results in the shift of the XPS peaks to higher binding energy. In this case, the binding energy has to be calibrated with an internal reference peak. The core electron of an element has a unique binding energy, which seems like a "fingerprint". The same atom is bonded to the different chemical species, leading to the change in the binding energy of its core electron. The variation of binding energy results in the shift of the corresponding XPS peak. Therefore, XPS is also known as electron spectroscopy for chemical analysis (ESCA). [85]

Since the number of photoelectron of an element is dependent upon the atomic concentration of that element in the sample, XPS is used to not only identify the elements but also quantify the chemical composition.

3.3 Auger electron spectroscopy

This is a surface based technique that occurs when a core level of surface atom is ionized by an impinging electron beam, the atom may decay to a lower energy state which further results in the ejection of an Auger electron. Auger electron spectroscopy (AES) provides quantitative elemental and chemical state information from surfaces. It is the kinetic energy of the Auger electron which is the characteristic material quantity irrespective of the primary beam composition (i.e., electrons, X-rays, ions) or its energy. For this reason Auger spectra are always plotted on a kinetic energy scale. [86] The main advantages of AES characterization technique are surface sensitivity, possibility of elemental and chemical composition analysis by comparison with standard samples of known composition, detection of elements heavier than Lithium, depth profiling analysis, spatial distribution of the elements etc.. Schematic representation of Auger process is shown in figure 3.7.

Quantitative analysis

AES analysis results can be quantified by using the area under the peaks in the AES spectrum after appropriate background subtraction and corrections based on the sensitivity factor of the elements in that area. A first order approximation to quantitative analysis can be accomplished through comparison of the Auger signal from the sample to the Auger signal from a pure elemental standard. Hence atomic concentration of element X can be obtained by:

$$C_x = I_x/I_{x, STD} \quad (3.5)$$

Atomic concentration can also be explained in terms of sensitivity factor as following:

$$C_x = (I_x/S_x d_x) / \sum_{\alpha} (I_{\alpha}/S_{\alpha} d_{\alpha}) \quad (3.6)$$

Whereas S is the sensitivity factor, d is the scale factor and I is the intensity. [87]

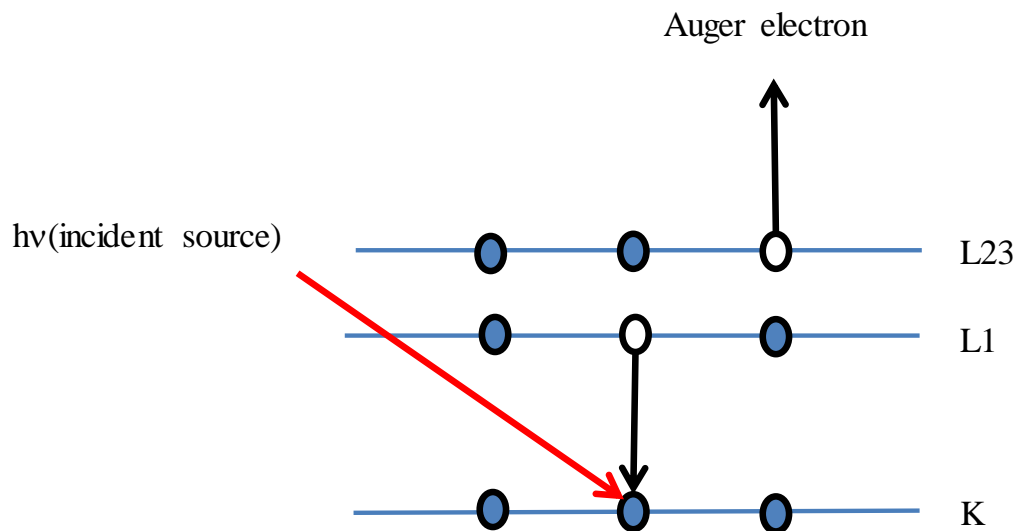


Fig. 3.7: Schematic representation of Auger process

Depth profiling

To analyze samples in depth, Auger instruments incorporate ion beam sputtering. Material is removed from the sample surface by sputtering with an energetic ion beam concurrent with successive AES analyses. This process measures the elemental distribution as a function of depth into the sample. [88]

3.4 Raman spectroscopy

Raman spectroscopy provides information about molecular vibrations that can be used for sample identification and quantitation. The technique involves a monochromatic light source (i.e. laser) which is focused on a sample and then detecting the scattered light. The Raman phenomenon was detected in 1928 by the Indian physicist C. V. Raman and Krishnan. [89] Independently of this work, the phenomenon was also reported by Grigory Landsberg and Leonid Mandelstam. [90]

The characteristic Raman frequencies provide the composition of material whereas the width of the Raman peak pointed to the crystal quality and the intensity of Raman peak give idea about the amount of material. Stress and strain states can be easily identified by observing the changes in the frequency of Raman peak. In Raman spectroscopy the scattered light having a frequency different from that of incident light is used to construct a Raman spectrum. Spectra obtained due to the inelastic collision between incident monochromatic radiation and molecules of sample.

When a monochromatic radiation strikes at sample, it scatters in all directions after its interaction with sample molecules. Much of this scattered radiation has a frequency which is equal to frequency of incident radiation and constitutes Rayleigh scattering. Only a small fraction of scattered radiation has a frequency different from frequency of incident radiation and constitutes Raman scattering. When the frequency of incident radiation is higher than frequency of scattered radiation, Stokes lines appear in Raman spectrum. But when the frequency of incident radiation is lower than frequency of scattered radiation, anti-Stokes lines appear in Raman spectrum. Scattered radiation is usually measured at right angle to incident radiation. The magnitude of Raman shifts does not depend on wavelength of incident radiation. Raman scattering depends on wavelength of incident radiation. [91–93] The energy level diagram of the entire transitions is shown in figure 3.8.

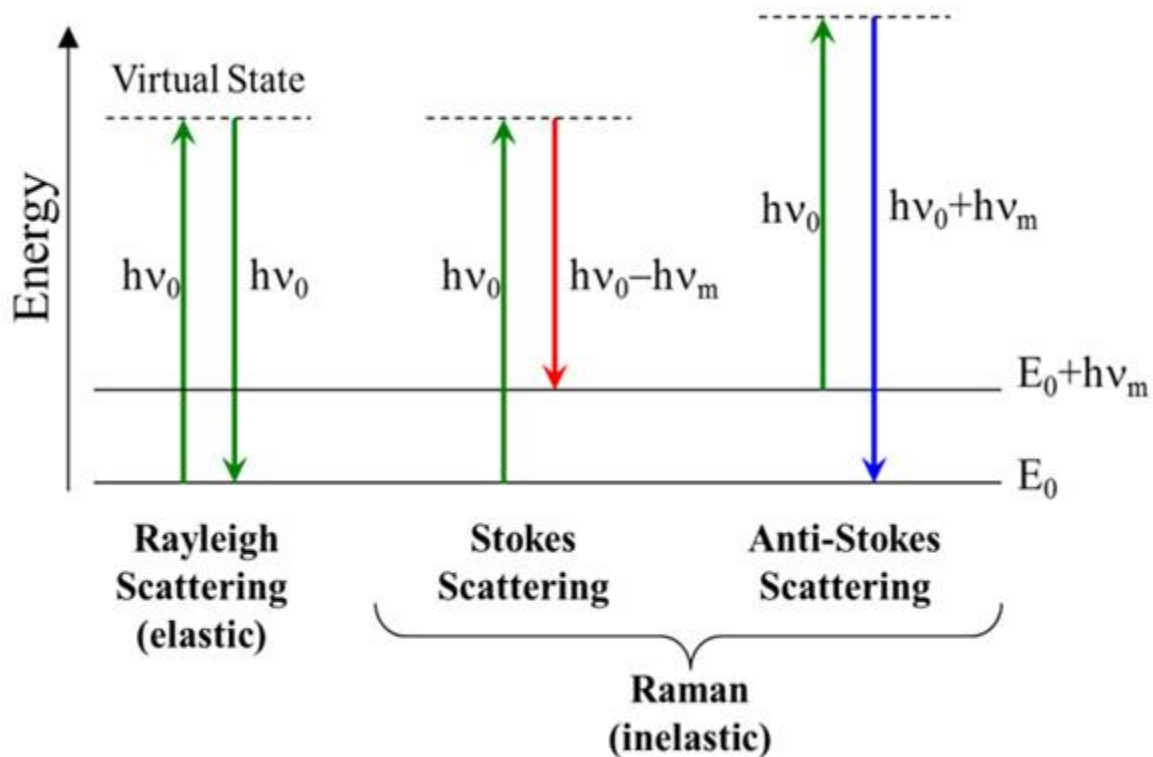


Fig. 3.8: Jablonski diagram of quantum energy transitions for Rayleigh and Raman scattering.

Raman spectra

Raman spectra is typically a plot of signal intensity vs Raman shift (wavenumber, cm^{-1}). This is an excellent tool for distinguishing and quantifying. Figure 3.9 shows the Raman spectra of silicon that reveals crystalline and amorphous nature. In crystalline silicon the well-ordered bond angles, bond strength and bond energy results in very sharp peak centered at $\sim 520 \text{ cm}^{-1}$ [94]. In non-crystalline (i.e., amorphous) silicon the varying bond angles leads to broad diffuse spectral features around 480 cm^{-1} . [95]

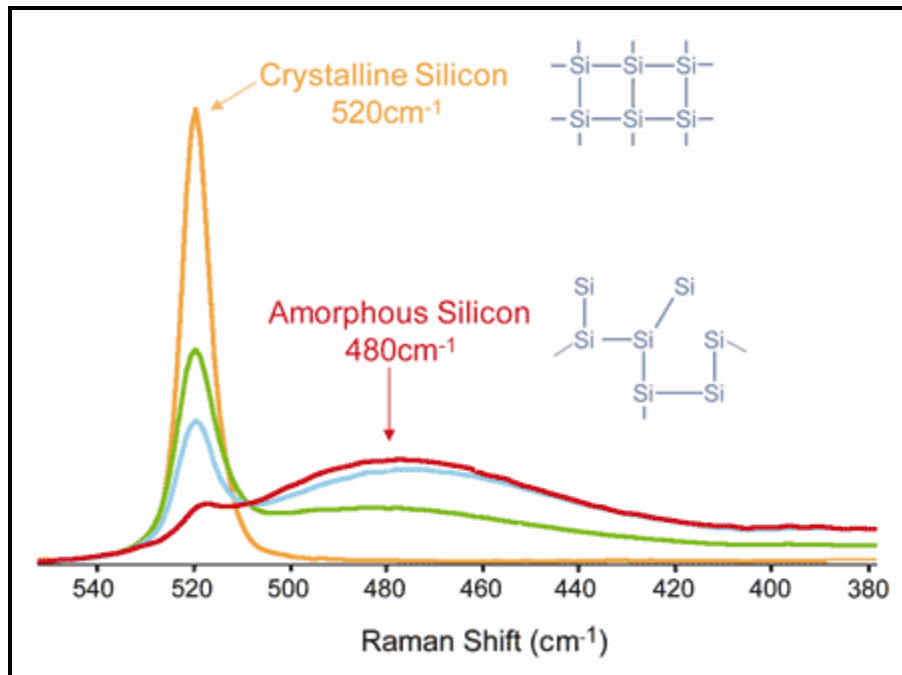


Fig. 3.9: Raman spectra revealing the presence of highly-crystalline (orange) and non-crystalline (green, cyan, red) material. (Data and image courtesy of Thermo Fisher Scientific, www.thermo.com/dxr and semrock.com)

Detailed descriptions about Raman spectroscopy can also be found in [96, 97]

3.5 Transmission electron microscopy

The historical background of electron microscopy started with the improvement of electron optics. In 1926, Busch studied the trajectories of charged particles in axially symmetric electric and magnetic fields. Almost at the same time, the French physicist de Broglie presented the idea of corpuscle waves. [98] These two thoughts laid foundation to shape an electron microscope. In 1932, Knoll and Ruska tried to find the resolution limit of the electron microscope [99], and their work resulted in the construction of first transmission electron microscope with a magnification of 16 in 1931. [100, 101]

Transmission electron microscopy (TEM) is a thorough method that has an uncommon capacity to give the majority of the structural, phase and crystallographic data of materials down to atomic levels. The TEM operates on the same basic principles as the light microscope however utilizes

electrons rather than light. Since the wavelength of electrons is much smaller than that of light, the optimal resolution attainable for TEM images is many orders of magnitude better than that from a light microscope. Thus, TEMs can uncover the finest details of the sample. Schematic representation of transmission electron microscope is shown in figure 3.10. TEM imaging system can be operated in two modes: diffraction mode and imaging mode.

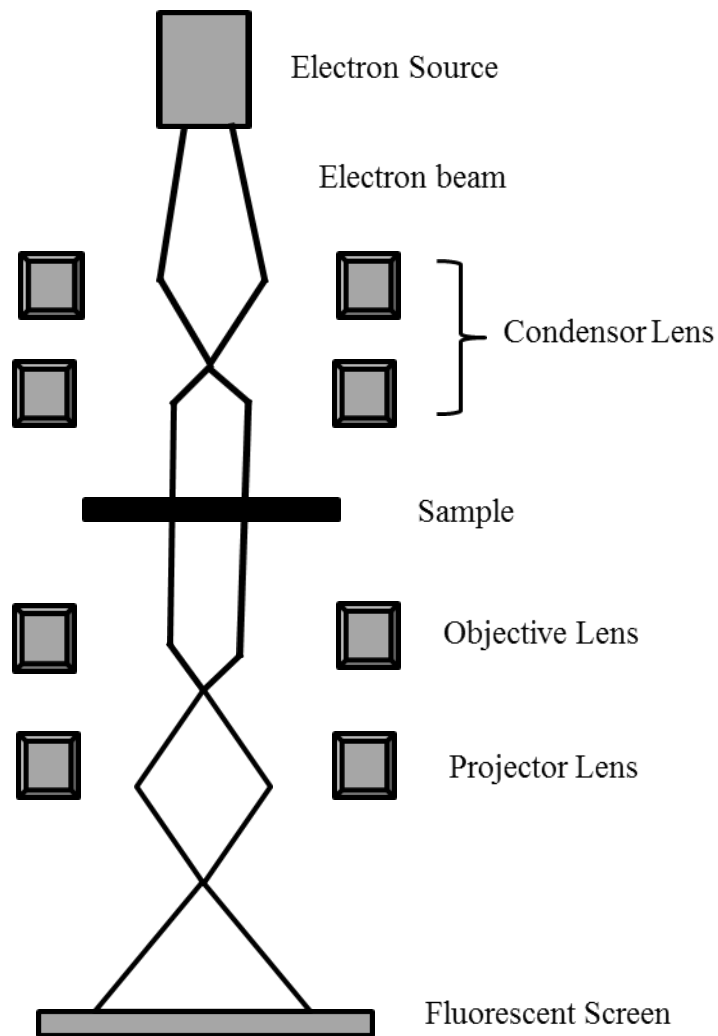


Fig. 3.10: Schematic representation of transmission electron microscope

Imaging modes

The contrast in conventional TEM is mainly due to diffraction/scattering contrast and mass-thickness contrast. This primarily depends on the scattering cross sections of the atom in the sample and the number of scattering atoms in the direction of propagation of electron beam. Samples with heavy elements or areas with large thickness scattered more which then provides darker contrast in the bright-field image. Based on the diffraction spot that contributes image formation, images are mainly classified into bright-field (BF) and dark-field (DF) images.

- Bright-field imaging mode:

This is the most common mode which provides contrast formation directly by diffraction and absorption of electrons in the sample. Thicker regions of the sample or regions with a higher atomic number will appear dark, while regions with no sample in the beam path will appear bright.

- Dark-field imaging mode:

In dark field (DF) images, the direct beam is blocked by the aperture while one or more diffracted beams are allowed to pass the objective aperture. Since diffracted beams have strongly interacted with the specimen, very useful information is present in DF images, e.g., about planar defects, stacking faults or particle size. As more of the deflected or scattered electrons are eliminated using smaller objective lens apertures, contrast will increase.

- High-resolution transmission electron microscopy (HRTEM):

This is also an imaging mode which is actually an interference pattern between the forward-scattered and diffracted electron waves from the sample. During transmission the incident electron wave is scattered (or diffracted in the case of a crystal) at the potentials of the atoms, and thereby the phase of the electron wave is changed. Hence it is also known as phase contrast mode.

[102] The schematic representation of all the three modes is shown in figure 3.11

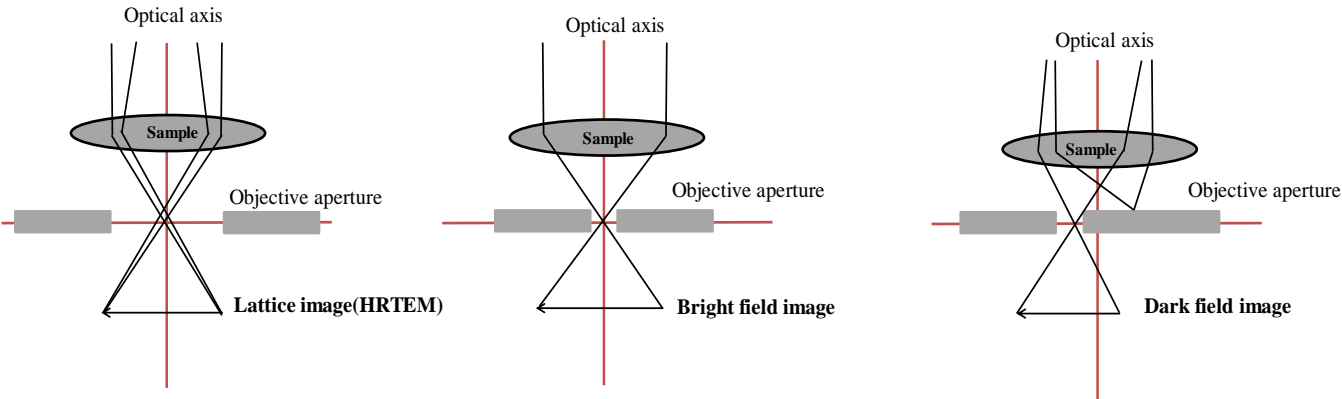


Fig. 3.11: Schematic representation of different imaging modes in transmission electron microscopy

3.6 Atomic force microscopy

Atomic force microscopy (AFM) is a type of scanning probe microscopy (SPM) where a small probe is scanned over the sample to obtain surface information. It operates by measuring force between the probe and the sample. Schematic representation of basic working principle of AFM is shown in figure 3.12.

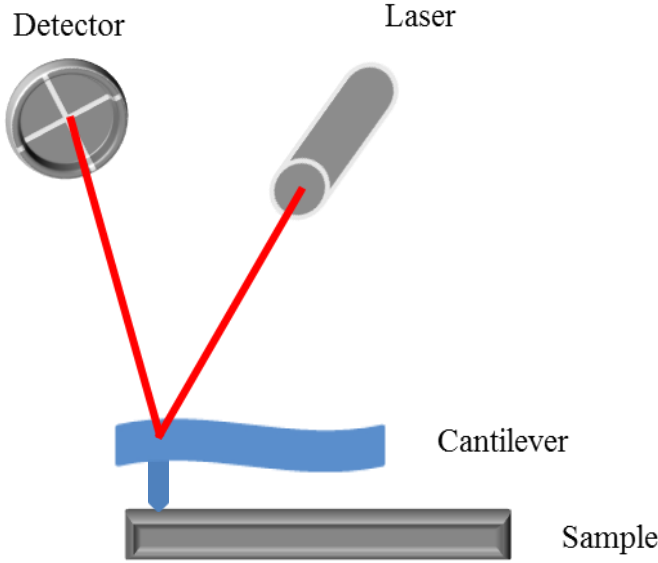


Fig. 3.12: Schematic representation of working principle of AFM (idea from Ref. [103])

3.6 Atomic force microscopy

For the surface sensing an AFM uses a cantilever with a very sharp tip to scan over the sample surface. When the tip approaches the surface, the attractive force between the surface and the tip makes the cantilever to deflect towards the surface. However, as the cantilever is conveyed considerably nearer to the surface, to such an extent that the tip makes contact with it, increasingly repulsive force takes over and causes the cantilever to deflect away from the surface. The laser beam is used to detect the cantilever deflections towards or away from the surface which is then monitored by the detector. [103] AFM can work in three different modes such as contact mode, tapping mode and non-contact mode. Only contact mode has been used in this work. In contact mode the AFM probe is scanned at a constant force between the probe and the sample surface which creates a topographical image. The scanner adjusts the probe position when the cantilever is deflected by topographical changes. [88, 104]

The force-distance curve shown in figure 3.13 depicts the interaction between the probe and the sample surface. When the probe and sample are far apart, weak attractive interactions exist and when it come closer (the separation distance decreases), the attractive force increases and began to interact and electrostatically repel each other. When the repulsive force is predominant, the tip and sample are considered to be in “contact”. A wide variety of image manipulations are available for AFM data. Lateral spacing, step height, and surface roughness can be easily obtained. More detailed descriptions about AFM can be found in. [105–107]

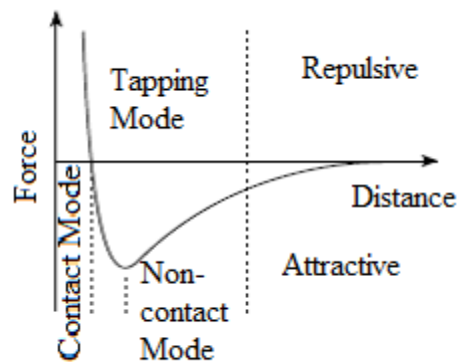


Fig. 3.13: Force-Distance curve that shows three modes in AFM (from Ref. [104])

4 Epitaxial Growth of Gd_2O_3 layers

Epitaxy in general is a process of crystal growth with a well-controlled phase transition that leads to single crystalline layer. The newly formed layer is known as epilayer or epitaxial layer. The orientation of the epitaxial layer depends on the underlying structure which is known as substrate. Epitaxy is generally classified as homoepitaxy and heteroepitaxy. If the substrate and epitaxial layer are of same material then it is known as homoepitaxy and if they are of different material then it is heteroepitaxy. [108] Epitaxial growth is useful for applications that place stringent demands on a deposited crystalline layer of high purity, low defect density, abrupt interfaces, controlled doping profiles, high repeatability and uniformity, safe and efficient operation. Osten et al. [6] reported the growth of crystalline rare earth oxides (REO) on Si by solid source molecular beam epitaxy (MBE). In this work, i used MBE for the growth of Gd_2O_3 film on crystalline Si substrates. In MBE beams of atoms or molecules in an ultra-high vacuum (UHV) environment are incident upon a heated crystal that has previously been processed to produce a nearly atomically clean surface. The arriving constituent atoms form a crystalline layer i.e., an epitaxial film. Because of the cleanliness of the growth environment and precise control over composition, MBE structures closely approximate the idealized models used in solid state theory. [109] Series of surface reactions [108] take place during the epitaxial growth is schematically represented in Figure 4.1. The basic physical processes in MBE vacuum chamber can be divided into three different zones: [110]

- First zone: Generation of molecular beams.
- Second zone: Mixing zone (molecular beams intersect one another).
- Third zone: epitaxial growth on the substrate which includes a series of following processes.
 - Adsorption of the constituent atoms or molecules.
 - Surface migration and dissociation of the adsorbed molecules.
 - Incorporation of the constituent atoms into the crystal lattice of the substrate or the epilayer already grown.

- Thermal desorption of the species not incorporated into the crystal lattice.

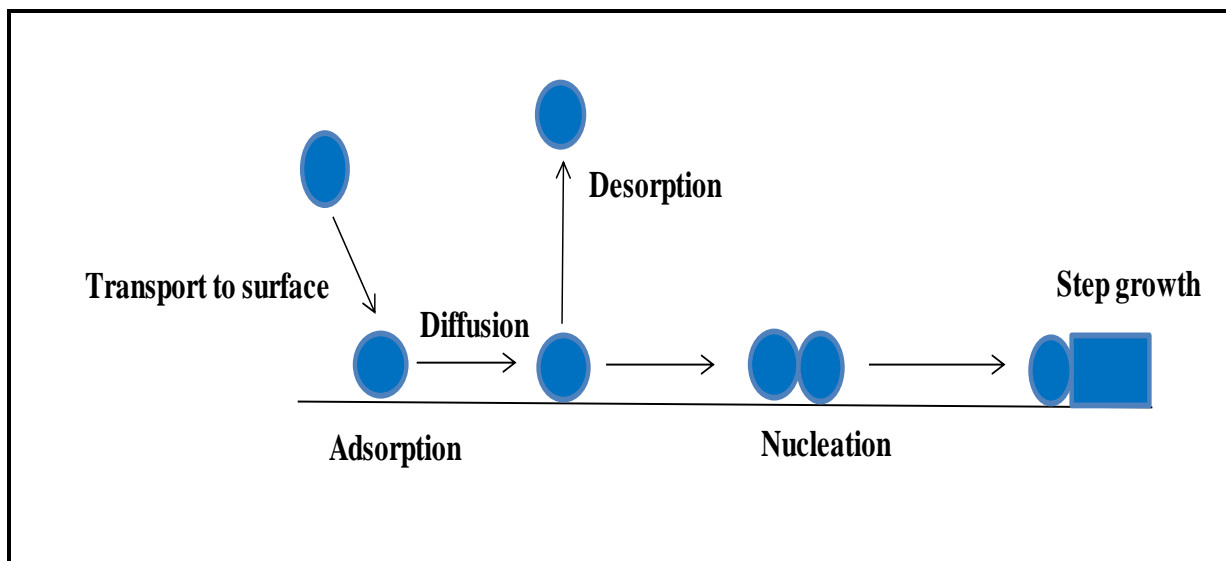


Fig. 4.1: Schematic representation of surface reactions during the epitaxial growth

Growth modes

Generally, three important modes of crystal growth may be distinguished in thin film deposition (depicted in Figure 4.2). These are: the Volmer-Weber mode (VW-mode, three-dimensional growth or islanding), [111] the Frank-van der Merwe mode (FM-mode, two-dimensional growth, smooth flat layer), [112] the Stranski Krastanov mode (SK-mode, a mixed mode, starting 2D and

later converting into islanding), [113] Which of these modes occurs depends on the relations of the surface energies:

$$\Delta\sigma = \sigma_{\text{sub}} - (\sigma_{\text{film}} + \sigma_{\text{IF}}) \quad (4.1)$$

where σ_{sub} is the surface energy of the substrate, σ_{film} that of the deposited film, and σ_{IF} is the interface energy. If $\Delta\sigma > 0$ (i.e. $\sigma_{\text{sub}} > \sigma_{\text{film}} + \sigma_{\text{IF}}$) perfect wetting occurs and the film grows two-dimensional. Opposite for $\Delta\sigma < 0$ (i.e. $\sigma_{\text{sub}} < \sigma_{\text{film}} + \sigma_{\text{IF}}$) we expect islanding.

For epitaxial growth, the same basic considerations hold. In addition, the mode by which the epitaxial film grows depends upon the lattice misfit between substrate and film, the supersaturation (the flux) of the crystallizing phase, the growth temperature and the adhesion energy. In the VW-mode, or island growth mode, small clusters are nucleated directly on the substrate surface and then grow into islands of the condensed phase. This happens when the atoms, or molecules, of the deposit are more strongly bound to each other than to the substrate. Volmer-Weber ("isolated islands") growth mode the adsorbate-adsorbate interactions are stronger than adsorbate-surface interactions, hence "islands" are formed right away. In Frank-van-der-Merwe ("layer-by-layer") growth mode the adsorbate-surface and adsorbate-adsorbate interactions are balanced. This type of growth requires lattice matching, and hence considered an "ideal" growth mechanism. Stranski–Krastanov growth ("joint islands" or "layer-plus-island"). In this growth mode the adsorbate-surface interactions are stronger than adsorbate-adsorbate interactions.

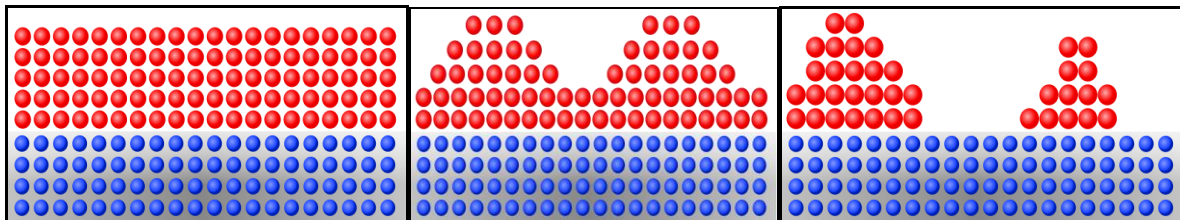


Fig. 4.2: Schematic representation of three different growth modes: Frank-van-der-Merwe mode (left), Stranski-Krastanov mode (middle) and Volmer-Weber mode (right). (Source Wikipedia, by David W, via Wikimedia Commons)

According to Hermann et al. [110] the important feature of all MBE techniques is the beam nature of the mass flow toward the substrate. It is important to consider the vacuum conditions,

i.e., the pressure of the residual gas in the vacuum reactor, which has to be ensured in order to preserve the beam nature. The mean free path and the concentration of the gas molecules are the two important parameters for the characterization of the vacuum. MBE, as the denomination suggests, uses localized beams of atoms or molecules in an ultra-high vacuum (UHV) environment to provide a source of the constituents to the growing surface of a substrate crystal. The beams impinge on the crystal kept at a moderately elevated temperature that provides adequate thermal energy to the arriving atoms for them to migrate over the surface to lattice sites. The UHV environment minimizes contamination of the growing surface. In the UHV environment, the beam atoms and molecules peregrinate in proximately collision-free paths until arriving either at the substrate or else at chilled walls of the chamber where they condense and are thus efficaciously abstracted from the system. When a shutter is interposed in a beam, that beam is efficaciously turned off instantly. These features make it possible to grow the films very gradually without contamination, and, most importantly, to transmute the composition of the arriving atom stream very abruptly; in fact, the composition of the flux can be transmuted in times much shorter than that needed to grow a single atom layer of the film. [109] Accurate selection and precise control on substrate temperature and source of constituent beams have direct role in growth process. The uniformity in thickness and composition of the films grown by MBE depends on the uniformities of the molecular beam fluxes and on the geometrical relationship between the configurations of the sources and the substrate. [110]

4.1 Molecular Beam Epitaxy-DCA S1000

For the epitaxial growth of Gd_2O_3 layer on Si (111) substrate we used DCA S 1000, multi chamber MBE system. The system allows maximum substrate size of 200 mm and includes UHV metallization, X-ray photoelectron spectroscopy (XPS) analysis and high temperature pre-cleaning facilities. The wafer handling is fully automatic and based on a UHV cluster tool. The main features of DCA S 1000 MBE system are large capacity effusion cells and electron guns, side mounted e-guns for easy access and service, multi-zone substrate heater up to $1000^\circ C$, magnetically coupled linear shutters, water or liquid Nitrogen

cooled cryo-panels. The schematic representation of DCA S1000 MBE system is shown in figure 4.3. The representation shows central distribution chamber which includes metal chamber, analysis chamber, load lock and preparation chamber. The growth chamber of the system is internally connected with the central distribution chamber. The growth chamber shows four electron guns and other 5 sources. The loads lock in this system provides fast substrate loading and unloading.

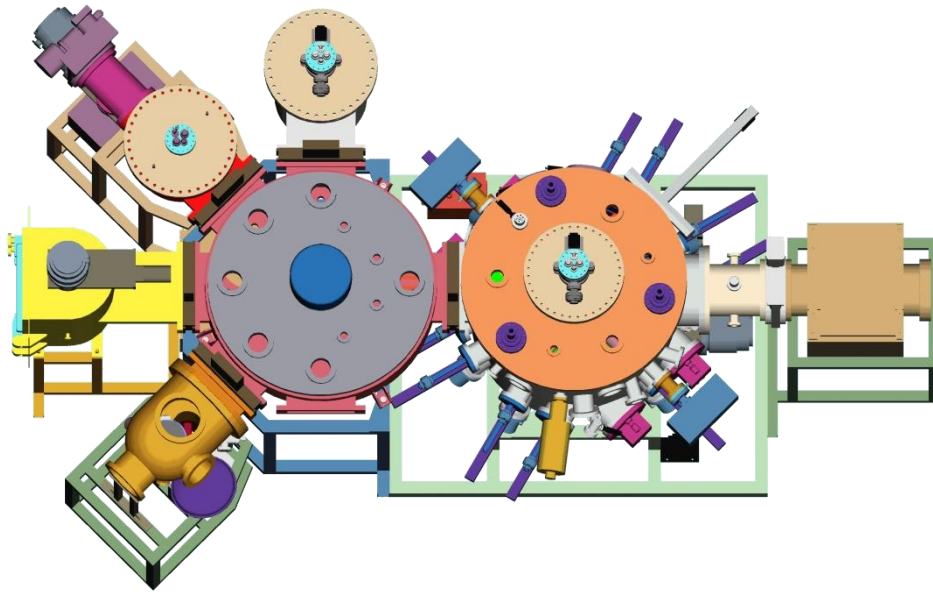


Fig. 4.3: Schematic representation of DCA S1000 MBE system.(Image source-DCA Instruments)

To obtain high-purity layers, it is critical that the material sources be extremely pure and that the entire process be done in an ultrahigh vacuum environment. Another important feature is that growth rates are typically on the order of a few $\text{\AA}/\text{s}$ and the beams can be shuttered in a fraction of a second, allowing for nearly atomically abrupt transitions from one material to another.

Growth Chamber

The growth chamber of DCA S 1000 system has a base pressure of 1.10^{-10} Torr. This is a 1000 mm vertical chamber which has a source port for 4 electron guns like Ge, Gd_2O_3 , Si, and Nd_2O_3 . All source ports located symmetrically around the chamber axis. The substrate growth surface is facing down during growth and during substrate loading/unloading procedures. The basic configuration of SGC 1000 consists of substrate manipulator, motorized main shutter, X-tal rate monitor, e-gun control system, High voltage reflection high energy electron diffraction (RHEED) unit, 200 amu residual gas analyzer (RGA), ion pump, turbo pump, cryo pump and vacuum gauging. In addition to electron guns 5 other sources like carbon, boron, plasma, Gd cell and Nd cell are also mounted. The e-gun features true 270° beam deflection and has maximum power rating. Maximum high voltage for the e-gun is 9 kV and an emission current of 0 to 670 mA at 9 kV. An electron beam is a stream of energetic charged particles flowing from a cathode emitter and accelerated by a high voltage direct current (DC) power supply. The kinetic energy of this stream of charged particles becomes random energy (heat) when the electrons strike the surface and this energy which is dissipated into the surface can melt and evaporate any material. Each effusion cell port is focused at the centre of the substrate having the same angle to the vertical. This has connecting flanges also which allows the use of high capacity effusion cells with integrated water cooling system. The schematic representation of growth chamber is shown in figure 4.4. It shows the electron guns and the effusion cells mounted to the growth chamber. Shutters are not shown in the figure. Liquid N_2 cryopanel surrounds internally both the main chamber wall and the source flange. Since MBE is a cold wall technique, cryopanel prevents re-evaporation from parts other than the hot cells. Besides, they provide thermal isolation among the different cells, as well as additional pumping of the residual gas. [114] The substrate manipulator consists of a hollow shaft inverted rotary motion feedthrough and a high temperature heater stage.

RHEED

RHEED stands for reflection high energy electron diffraction. Staib instruments RHEED gun is the main and essential part. While during the growth we normally set RHEED voltage as 18 kV and current 1.6 A. RHEED voltage can safely go up to 25 kV. High voltage power supply with focus and beam energy control eases the operation. XY beam position controller can be used to adjust according to the requirements. One of the main features of RHEED unit is the 100 mm

phosphorus screen with manual viewport shutter. The fluorescent screen is taken up directly by a charge coupled device (CCD) camera. The diffraction patterns are transmitted directly to a computer connected with evaluation software.

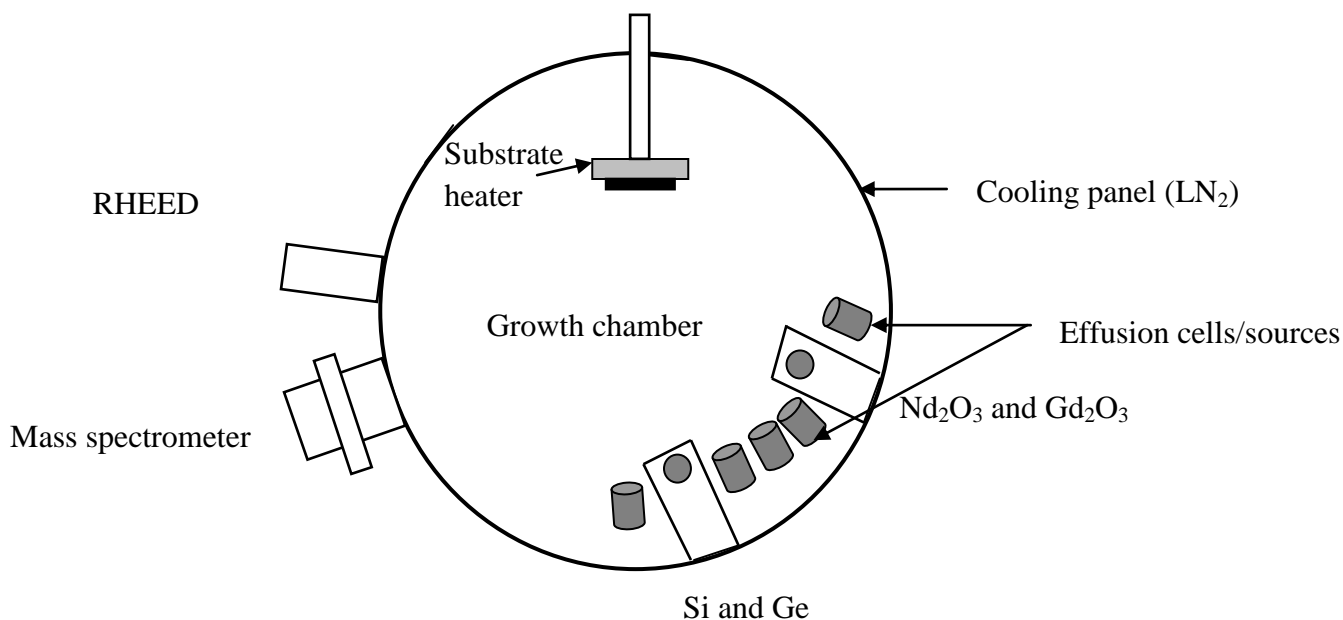


Fig.4.4: Schematic representation -basic configuration of growth chamber SGC 1000

Metal chamber

After the growth process, the sample can directly be subjected for in situ metallization process by transferring from growth chamber to the central distribution chamber (CDC) then to the metal chamber. The metal chamber contains a TELEMAR 568 e-beam evaporation system. It has the capacity of holding four metals such as Aluminium, Platinum, Tungsten, and Tantalum. Through this metallization process we deposit a layer of metal on the top. Metal is melted in vacuum and transported to the sample through vacuum. Deposition rate depends on pressure, temperature and atomic mass of species.

4.2 Gd₂O₃ epitaxy on silicon

Commonly, epitaxial heterostructures are evaluated on the basis of lattice matching, with the misfit defined as the relative difference in the lattice constants (a_{film} and a_{Si}). Here, the lattice mismatch would be identical for all three epitaxial relationships, i.e. (100)//(100), (110)//(110), and (111)//(111). All other combinations violate symmetry matching. This concept is misleading, because epitaxial growth is also governed by the surface and interface energetics. In case of rare-earth oxides, the surface energy of the (100) surface is much higher than that of Si (100). [115] That could result in a 3-dimensional growth mode or in a change of the growth direction towards a low-energy surface orientation. The later is observed for the growth on Si (100) for most of the lanthanide oxides, where the oxides were found to grow in (110) orientation. For the understanding of the Gd₂O₃ (110)/Si (100) interface formation we have to consider that the lattice is made up of metal atoms occupying the positions of a face-centered cubic lattice with a lattice constant a_{film} , where the tetrahedral holes are occupied by oxygen atoms. However, the growth of gadolinium oxide is based on the deposition of metal oxide molecules. Due to the existence of highly ionic Gd—O bonds in combination with the high bonding strength of the covalent Si—O bonds, we can assume that the interface is predominantly formed by Si—O—Gd bonds. Therefore, the matching of the oxygen atoms is the important parameter. The complete crystallographic structure can also be described by two non-identical metal and oxygen lattices, respectively. The arrangement of the oxygen atoms forms a simple cubic lattice with a lattice constant of $a_{\text{film}}/2$. Thus, the interesting matching condition for epitaxial growth is the Gd₂O₃ (110)[100]//Si (100)[110] relation. In that case, nearly 1:1 matching should occur along one direction. In the other direction, there would be roughly a 3:2 matching relation. Layers grown in this orientation exhibit mostly two types of (110)-oriented domains, with two orthogonal in-plane orientations (found experimentally for a large variety of binary metal oxides on Si (100), like Er₂O₃ [48], Sm₂O₃ [49], Lu₂O₃ [50, 116], Sc₂O₃ [51], Gd₂O₃ and Y₂O₃ [117]). That is even enforced by the Si (100) dimer (2x1) surface reconstruction. Dimer rows on adjacent terraces are oriented perpendicular to each other and nucleation of the oxide on Si (100) follows the dimer orientation, what results in the domains on stepped surfaces. [118] Due to the 45° rotation of the (110) plane relative to the substrate, the mismatch for the 1:1 matching is identical to that one obtained from applying the lattice constant concept.

To avoid all problems connected with the domain formation as described above, we use exclusively Si (111) as the substrate. Here the situation is much easier: *Bixbyite* Gd_2O_3 grows epitaxially on (111) oriented Si surface. However it is known, that the single crystalline layer exhibits an A/B twining relationship where B orientation is related to the substrate A by 180° rotation around the Si (111) surface normal. The in-plane epitaxial relationship between the films and Si (111) substrate is $\text{Gd}_2\text{O}_3(111)[-110]//\text{Si}(111)[1-10]$. [54]

4.3 Sample preparation

Substrate

P-type boron doped 100 mm Si (111) substrates are used for the growth of Gd_2O_3 layers. The resistivity of the wafers ranges from 0.2-0.3 Ωcm and the thickness is 525 μm . Wafers are formed of highly pure (99.9999999% purity); nearly defect-free single crystalline material. [119]

Wafer Cleaning

Wafers were cleaned wet chemically prior to loading into the molecular beam epitaxy system. The native oxide of the wafer is first removed by using 0.175% dilute hydrofluoric acid (HF). The wafers are then oxidized selectively in an UV/ozone environment and, finally with a further HF cleaning which removes the carbon contaminants from the surface. [120] Hydrogen terminated silicon wafers were loaded into UHV system.

Growth process

Substrates were annealed at 790°C in situ for 10 minutes; this transforms the initial hydrogen-terminated (1x1) surface structure into the (7x7) superstructure indicating a clean and well-ordered surface. Commercially available, granular Gd_2O_3 material was evaporated using an electron-beam evaporator with a gun power of 11.4%. Growth temperature was 650°C and additional oxygen was supplied during growth with a partial pressure of $5 \cdot 10^{-7}$ Torr. Oxygen supply during growth improves the dielectric properties significantly; however, too high oxygen partial pressures lead to the formation of interfacial layer. [121] The thickness of the layer was estimated by X-ray reflectometry. With the same growth conditions, i

prepared different samples by varying the growth time and thus the layer thickness. On (111) oriented Si surface, cubic *bixbyite* Gd_2O_3 grows epitaxially when the substrate temperature is above 600 °C. The grown samples were characterized using X-ray diffraction, Atomic force microscopy, X-ray photoelectron spectroscopy.

4.4 Results

Structural Evolution:

Figure 4.5 shows the structural evolution of epitaxial layer on Si (111) substrate. The RHEED pattern shows the 7×7 reconstructed surface layer and the final layer which describes the good crystalline quality of the layer grown on Si substrate. The streaky RHEED pattern shows the 2-dimensional growth of the layer on Si (111). The streaky bright patterns indicate a rather smooth surface of the epitaxial crystalline oxide layer. [122]

Figure 4.6 shows the X-ray (θ - 2θ scan) diffraction patterns of Gd_2O_3 thin films grown on Si (111) substrate. The layers on the Si (111) substrate also exhibit single orientation without any indication of disoriented crystallites. The peaks at 28.5° and 59.4° correspond to $d(222)$ and $d(444)$ interplanar spacing. [123]

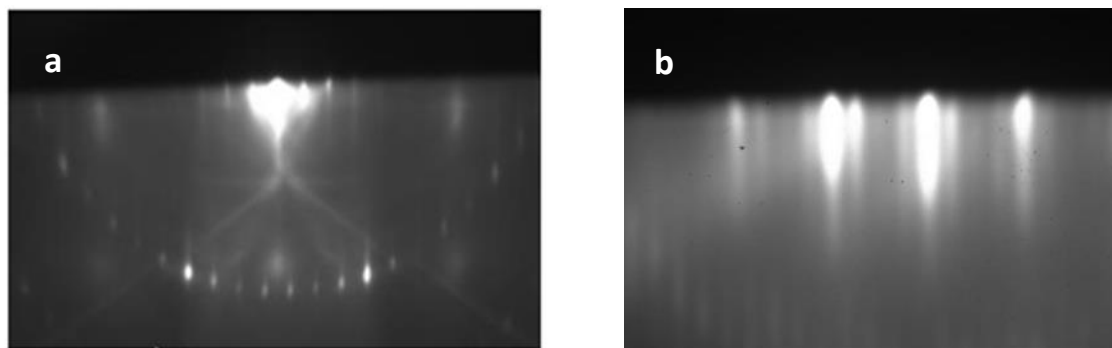


Fig. 4.5: RHEED pattern shows a) reconstructed surface b) RHEED pattern along $\langle 110 \rangle$ azimuth of final epitaxial layer

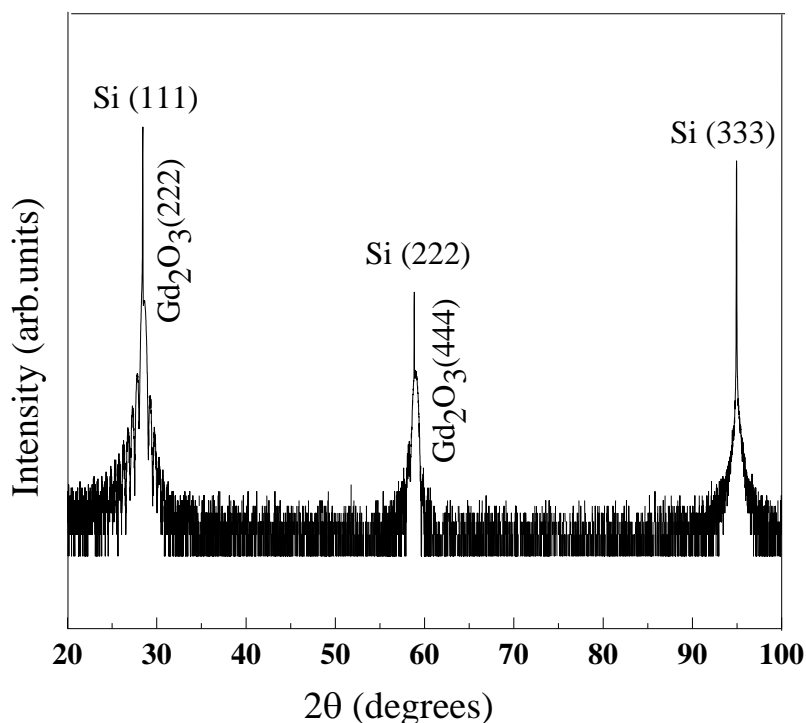


Fig. 4.6: XRD pattern of epitaxial Gd₂O₃ on Si (111) Substrate

XPS Results:

Figure 4.7 shows the O 1s (left) and Gd 4d (right) XPS spectra of Gd₂O₃ thin films with fitted curve. These confirm that Gd metal with binding energy (BE) 140.0 eV is fully oxidized Gd⁺³, ~143.4 eV with corresponding chemical shift of 3.4 eV toward higher binding energy. O 1s gave a peak at 531.2 eV agrees well with literature. [124] Emission of an electron from a core level of an atom that itself has a spin can create a vacancy in two or more ways. The coupling of the new unpaired electron left after photoemission from the orbital with other unpaired electrons in the atom can create an ion with several possible final state configurations. This results in a photoelectron line which splits asymmetrically. [125] Gd 4d gives a broad structure due to the doublet appearance.

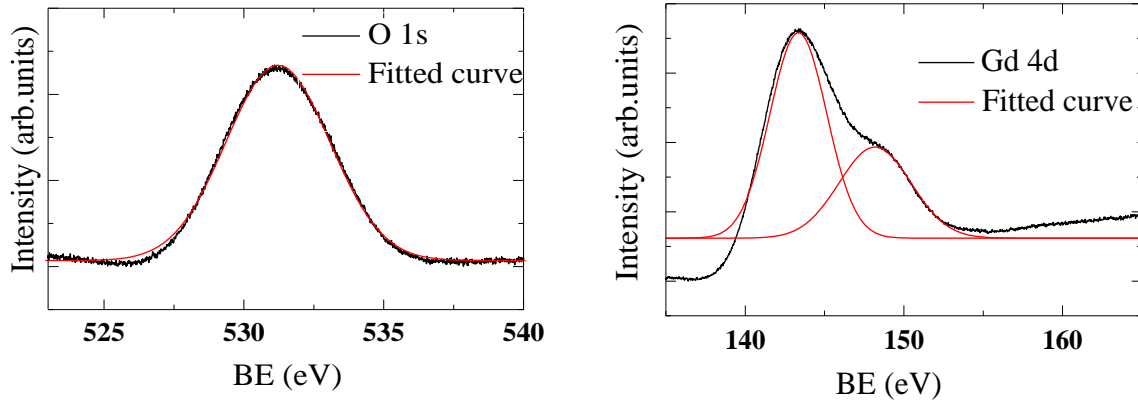


Fig. 4.7: X-ray photoelectron spectra of O 1s level (left) and Gd 4d level (right) with fitted - curve (red)

Surface Morphology:

AFM image depicted in figure 4.8 shows very good surface quality with a root mean square roughness $R_{rms} = 0.8$ nm. The expected step height for Si (111) is 0.3 nm. [126] The measured step height is ~ 0.5 nm for the first step. (shown in profile 1)

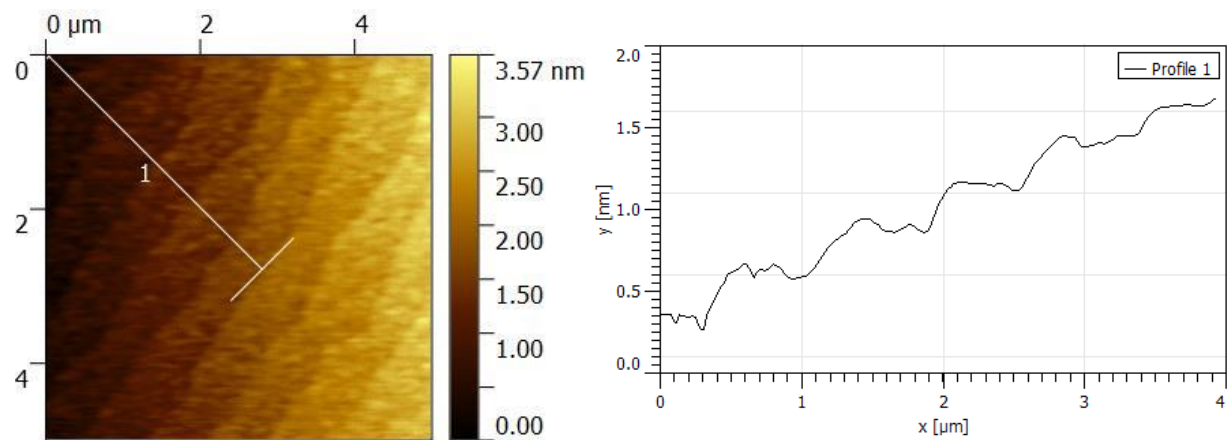


Fig. 4.8: AFM surface morphology of Gd_2O_3 layer on Si (111) substrate with white mark used for line scan (left) and the line scan profile which gives step height on Y- axis (right)

Summary

To summarize the epitaxial growth, MBE growth and research is found to be an asset for the production of semiconductor devices that has wide applications in the field of optoelectronics, high speed transistors etc. MBE technique can be easily applied for growing layers with different compositions, thickness and differing bandgaps. The unique combination of ultra-high vacuum conditions, low growth temperatures, in situ surface analysis tools and precise control on source are all the characteristic tool of MBE approach.

DCA S 1000 mbe system which we used for the epitaxial growth possess all these characteristic feature of MBE. Integration of high dielectric materials on silicon substrates is widely investigated. Gadolinium oxide which is very well known as the most promising candidate in future electronics is grown by molecular beam epitaxy method.

Gadolinium oxide on Si (111) substrate was characterized using RHEED, XRD, XPS and AFM techniques which depicts the formation of high quality crystalline epitaxial film on silicon substrate which agrees well with the literature values.

5 Nitridation of epitaxial Gd_2O_3 films

Why nitridation of epitaxially grown Gd_2O_3 is important can be explained on the basis of both the positive and negative sides of high-k materials. Epitaxial growth of crystalline oxides on Si attracts intensive research due to its epitaxial nature that results in an interface structure without (or with a very few) dangling bonds, which can possess low interface trap density and high carrier mobility for devices. [127] Growing epitaxial high-k oxides on silicon is also a promising approach for nanostructure formation of crystalline silicon quantum-wells. [6] Gottlob et al. [128] have demonstrated for the first time a fully functional n-MOSFET (metal oxide semiconductor field effect transistor) with a TiN/ Gd_2O_3 /Si (001) system. Appreciating their excellent structural qualities, most of the REOs grown epitaxially on Si exhibit some disadvantages like poor electrical properties, instability in the threshold voltage, high leakage current density, etc. [9, 10] The most commonly found electrically active defects are the omnipresent oxygen vacancies (v_{os}). The presence of oxygen vacancies gives rise to the degradation of electrical properties. [11] Here comes the importance of nitridation process. To be more precise, studies demonstrated that the incorporation of nitrogen into the high-k dielectric interface with the Si substrate could be very effective in suppressing crystallization of metal oxides, [12] decreasing dopant (in this work nitrogen) concentration into bulk Si, [13] inhibiting interfacial reaction with the Si substrate, [13,14] and also improving both the material and electrical performance of the device. [15–17] Liu et al. [129] reported that nitrated GdO dielectric with post-deposition annealing in NH_3 is a promising candidate as the charge storage layer of advanced Metal-Oxide-Nitride-Oxide-Silicon (MONOS) nonvolatile memory devices. On the other hand REN eg. Gadolinium nitride (GdN) is the most thoroughly studied candidate for high-k dielectrics. [22] Not much is known about gadolinium oxynitrides with comparable O and N concentrations. It is reported that the solubility limit of GdO in GdN depends on the preparation temperature, but can be up to $\text{GdN}_{0.65}\text{O}_{0.35}$. [24] In a recent paper, Wang et al. [25] demonstrate nitrogen plasma immersion ion implantation into gadolinium oxide.

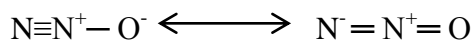
However, the authors did not give any evidence about the composition of the formed ternary Gd_xO_yN_z layer. Combinations of nitride and oxide layers (for example SiON) have been used for years in various applications like oxide-nitride (ON) or oxide-nitride-oxide (ONO) DRAM capacitor dielectric, or metal-nitride-oxide-silicon (MNOS) stacks for memory devices. [130] It could be very interesting to try different methods for oxynitride formation, specifically rare earth oxynitride.

In this chapter, i tried to incorporate nitrogen into Gd₂O₃ layers. Different methods of nitridation processes were tested to evaluate the possibilities to fabricate gadolinium oxynitride layers. The following four different nitridation processes were studied:

- Growth in a N₂O gas ambient
- Use of nitrogen and N₂O plasma during growth
- Exposure to activated NH₃
- Ion Implantation Process (chapter 6)

5.1 Growth in a N₂O gas ambient

Nitrous Oxide (N₂O) widely known as laughing gas is used for the nitridation process. Nitrous oxide represents a classic example of a molecule that resonates between two valence bond structures with different bond distributions. [131] Nitrous Oxide is 36% oxygen by weight. Nitrous Oxide is composed of 2 parts nitrogen and 1 part oxygen.



At room temperature, N₂O is quiet unreactive. When heated sufficiently, N₂O decomposes into N₂ and O₂. Several approaches are available in order to simulate the gas phase decomposition of the N₂O molecule. The approach of Ellis and Buhrman [132] depicts N₂O gas phase decomposition can be simulated with a simple eight reaction scheme. The first step in the decomposition of N₂O is dissociation into N₂ and O (atomic oxygen)



The atomic oxygen liberated in (R₁) is rapidly take part in one of the following reactions

5.1.1 Sample preparation



Factor M corresponds to the different collision partners and is equal to the sum of the different species in the chamber. During the decomposition process, five different compounds are generated: molecular nitrogen (N_2), molecular oxygen (O_2), nitric oxide (NO), nitrogen dioxide (NO_2) and atomic oxygen (O). [133] The basic chemistry while passing N_2O gas is that it decomposes exothermically and reacts with metal Gadolinium resulting in the epitaxial growth of the film which incorporates oxygen and nitrogen along with gadolinium (because here i use metallic Gd instead of Gd_2O_3). One of the main advantages of gas nitriding is that precise control throughout the growth process by controlling the flow rate of N_2O gas.

5.1.1 Sample Preparation

After HF and UV/ozone cleaning process, Si (111) substrate was introduced into the load lock of the MBE (DCA instruments) system. Placing the sample inside the deposition chamber the sample preparation process was as follows:

Firstly increase the substrate temperature $T_s = 720^\circ\text{C}$, and performed silicon surface preparation for 20 minutes to transform the initially hydrogen-terminated (1x1) surface structure into the (7x7) surface superstructure, which indicates a clean and well-ordered surface. Then the substrate temperature is reduced to 650°C for the growth process. [121] The effusion cell which contains metal Gd crucibles is heated up slowly. For nitridation of the Gd_2O_3 layers, molecular N_2O was introduced into the chamber during growth using a piezo leak valve. [21] The growth parameters were set as:

- Growth Temperature=650°C
- Gd Cell temperature=1250°C
- Partial Pressure of N₂O, P_{N₂O} ~ 8·10⁻⁷ Torr

During the 2 hour process, the evolution of epitaxial layers was monitored by in-situ RHEED.

5.1.2 Results

Structural Evolution:

Figure 5.1 (a), (b) shows the structural evolution of epitaxial layer on Si (111) substrate. The RHEED pattern shows the 7x7 reconstructed surface layer and the final layer which describes the good crystalline quality of the layer grown on Si substrate. The streaky RHEED pattern shows the 2-dimensional growth of the layer on Si (111) and indicates rather smooth surface of the epitaxial crystalline oxide layer. [122]

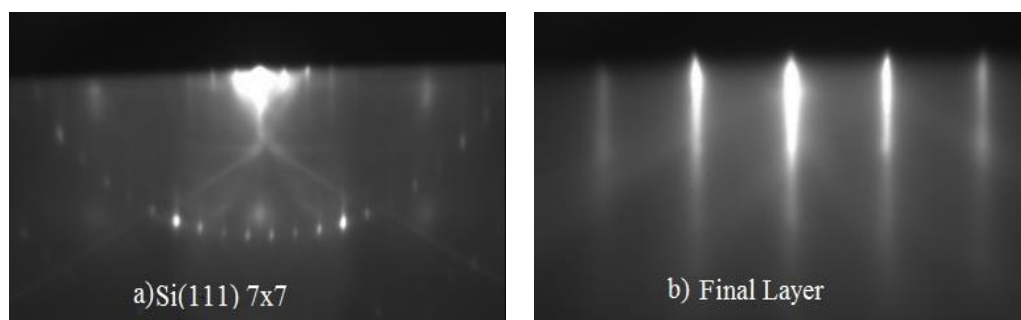


Fig. 5.1: (a) RHEED pattern shows reconstructed surface (b) RHEED pattern along <110> azimuth of final epitaxial layer.

Figure 5.2 shows the X-ray diffraction pattern of the layer after nitridation and an XRD pattern of reference Gd₂O₃ sample. In both cases the crystalline nature of the epitaxial layer grown on the Si (111) substrate depicts here. The thickness of the layer after nitridation is found to be ~3.2 nm using X-ray reflectometry (XRR) is shown in figure 5.3. The shoulder observed at 2 Θ ~ 28.9° beside the Si (111) peak corresponds to the (111) oriented epitaxial growth of Gd₂O₃ with cubic *bixbyite* type of structure. [21]

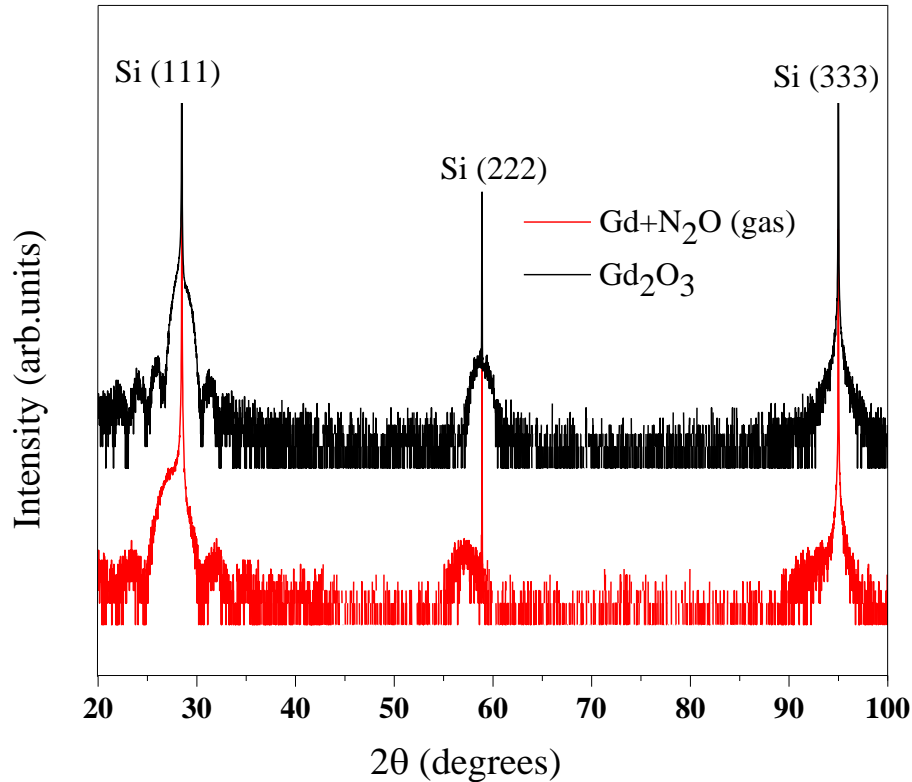


Fig. 5.2: XRD pattern of epitaxial Gd_2O_3 and $\text{Gd}+\text{N}_2\text{O}$ layer on Si (111) Substrate

The Gd_2O_3 (444) peak is normally observed at $2\theta \sim 59.05^\circ$ which we can see in reference Gd_2O_3 sample, [123] but for this sample which is nitrided in the presence of molecular N_2O shows the shoulder peak in the region of Si (222) is at $2\theta \sim 57.2^\circ$. So here we observed a shift of $\sim 1.85^\circ$. The shift in the peak is may be due to the incorporation of nitrogen or due to some lattice strain during the growth. For the clarification we performed other characterization techniques that reveal the composition of the layer.

TEM Investigations:

The epitaxial growth of oxide layer is confirmed from the TEM structural investigations (done by Dr. Eberhard Bugiel) shown in figure 5.4 (a), (b). The thickness of the layer is estimated as ~ 3.5 nm. In the layer disturbances are embedded, which regularly present to the crystal orientations parallel to the 110-directions. HRTEM images show a defined orientation to the substrate. The defect seen here in the interface is suspected to be a silicide formation, but the chance of oxide formation cannot be excluded. It is striking that these crystallites are grown in the

Si substrate and in the oxide layer. Single domain cubic Gd_2O_3 thin films were epitaxially grown, in the bixbyite structure on Si (111) due to their low lattice mismatch. An important parameter to succeed in high quality growth without any interface layer formation is the partial oxygen pressure. [121]

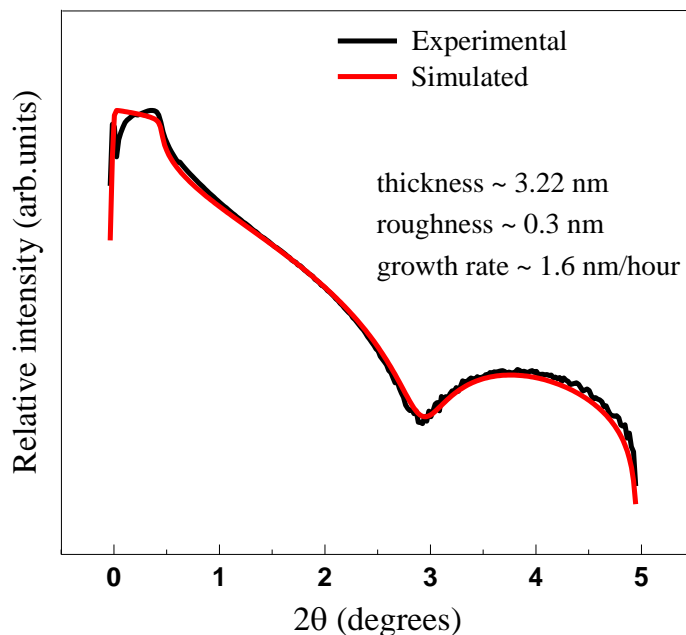


Fig. 5.3: X-ray reflectivity thickness measurements

In this process i don't provide any additional Oxygen during the growth instead we pass N_2O gas which provides two functions. One nitridation and second is layer quality by providing oxygen due to the decomposition of N_2O . Enough oxygen chemical potential is needed to avoid the silicidation of the Si surface, which will lead to a Volmer–Weber growth of Gd_2O_3 because of its wetting behavior on Si surface. [134]

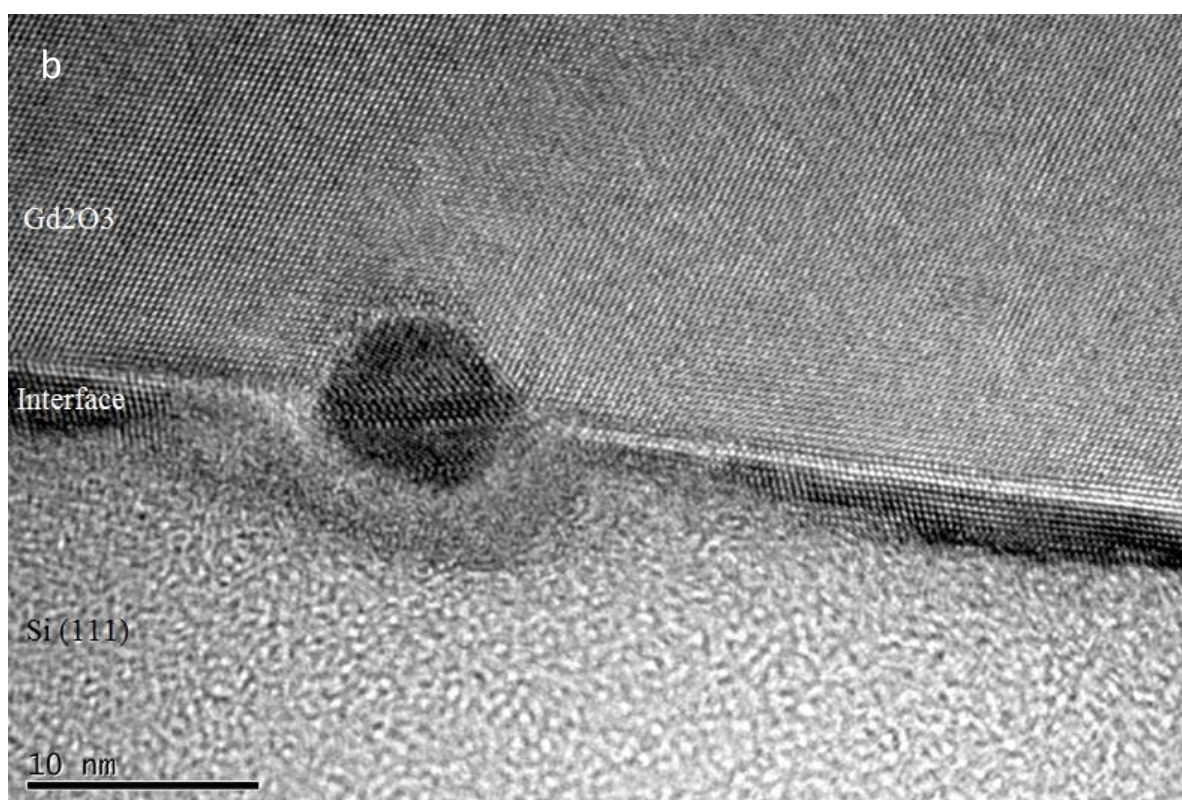
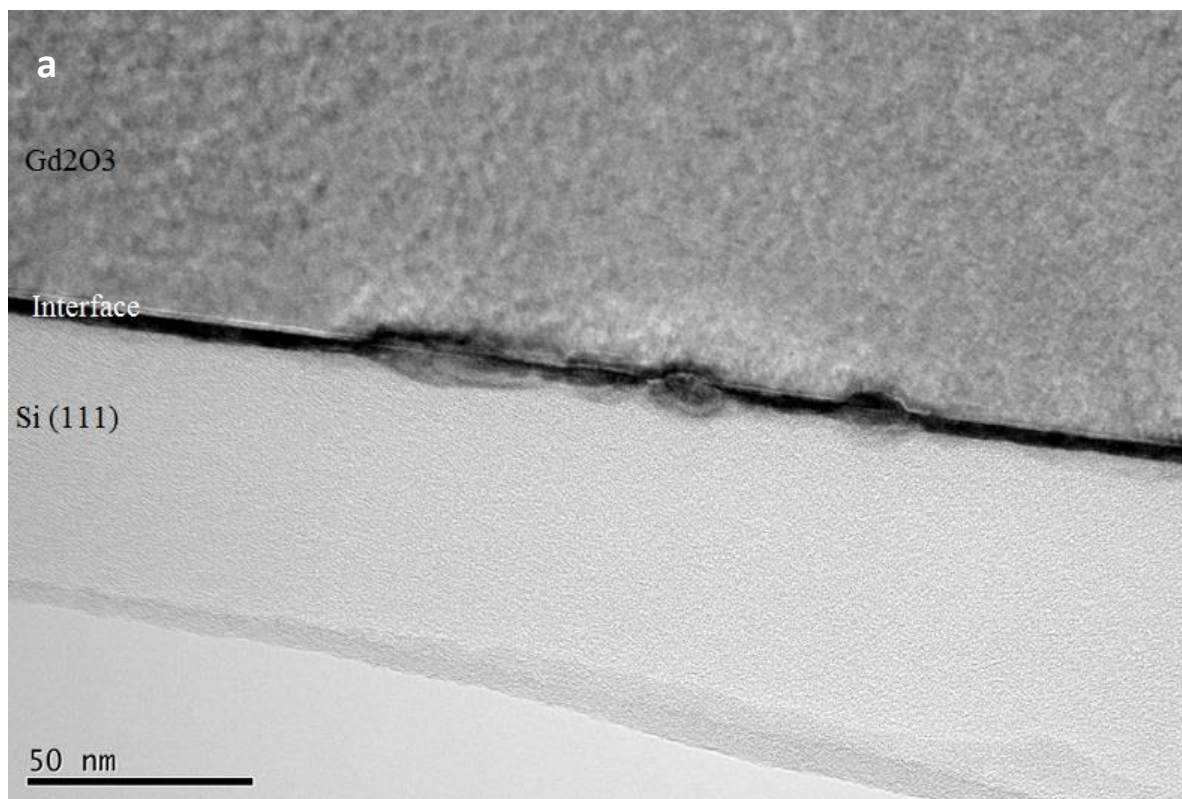


Fig. 5.4: a) TEM investigation of the epitaxially grown layer b) HRTEM showing defects in the interfacial region.

XPS Result:

To know more about the composition of the layer on Si (111), X-ray photoelectron spectroscopy (XPS) technique is used. XPS measurements were performed at Gd 4d, O 1s and Si 2p levels using the Mg $k\alpha$ source (1253.6 eV) with pass energy of 80 eV. Figure 5.5: a) shows the Gd 4d level. Here Gd 4d peak is obtained at 143.7 eV with a correction factor of ± 0.2 eV. Database gives a value ranges from 143.5 eV-144 eV for the Gd_2O_3 compound which we also observed in our reference sample without any nitridation step. [124] Hence the peak at 143.7 eV shows Gd-O bonding. There are no traces of nitrogen incorporation. If nitrogen makes a bond with gadolinium then we observe a shift in the peak. Figure 5.5: b) shows the O 1s level. The peak we obtained here agrees well with the databases. The peak for O 1s level at ~ 531.1 eV defines Gd-O bond and in case of Si, after the peak fitting session shown in figure 5.5: c), it obtained peaks at ~ 99.9 eV and 103.3 eV. Peak at 99.9 eV corresponds to Si-Si bonds from the bulk silicon wafer beneath the oxide layer and the signal at 103.3 eV corresponds to the SiO_2 in the oxide layer. [6,135]

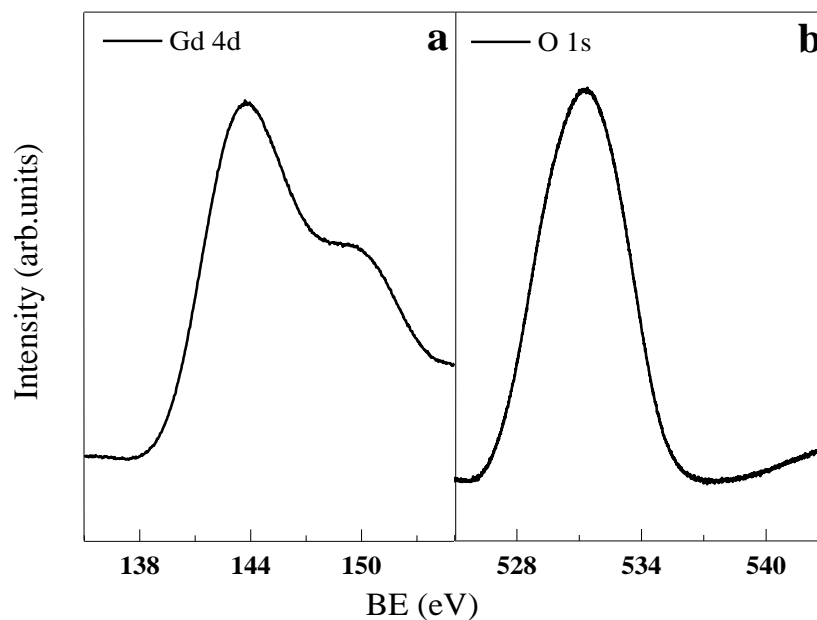


Fig. 5.5: X-ray photoelectron spectra of a) Gd 4d level b) O 1s level

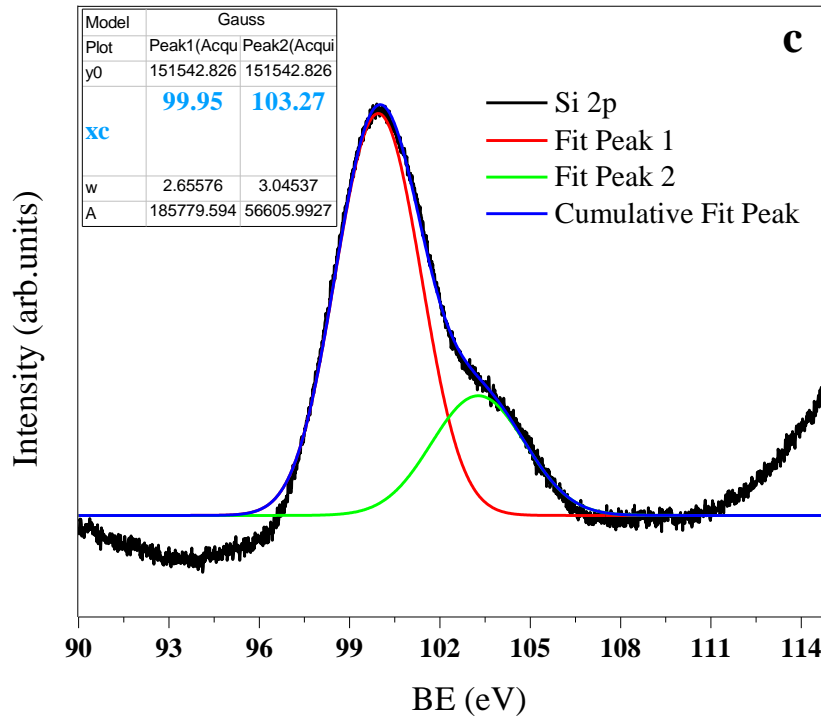


Fig. 5.5: c) Fitted Si 2p XPS peak

Electron Energy Loss Spectroscopy (EELS):

Electron energy loss spectroscopy (EELS) is the study of the vibrational motion of atoms and molecules on and near the surface. Electrons lose energy due to inelastic scattering. Figure 5.6 shows the EELS spectra which depicts that the sample contains Gd, O and Si. But it doesn't show any presence of nitrogen which also agrees with our XPS results. Element specific EELS spectra, allowing the determination of the chemical composition of nanometer thick layers. The EELS spectra showed here depicts no nitrogen incorporation, either in the film or in the crystallites.

Opposite to our results, Kawada et al. [136] were able to produce lanthanum oxynitrides using a similar approach. Their films were deposited by evaporating lanthanum at a substrate temperature of 300°C, and introducing oxygen and nitrogen radicals into a chamber. After a post-deposition thermal annealing (PDA) of the films at 600°C for 30 min, they authors could clearly show the presence of nitrogen in the films. From XPS measurements, they extracted a ratio of oxygen to nitrogen was 82:18 for the nonannealed film. They also found that the nitrogen content decreased after the PDA and ratio of oxygen to nitrogen became 93:7. To understand the discrepancy with

my results, an experimental investigation from M. L. Campell is very useful. [137] He investigated temperature dependent rate constants for the reaction of gas phase lanthanides with N₂O. Generally, the reactions of metal atoms, M, with N₂O is given by:



Such reactions are exothermic due to the formation of stable N₂ and metal oxide molecules. Despite that fact, metal reactions with N₂O have been observed to have significant energy barriers. Using an Arrhenius approach, Campell extracted activation energies of only 2.1 kJ/mol for La but 6.4 kJ/mol for Gd. Thus, the formation of Lanthanum oxynitrides is much more likely than the formation of gadolinium oxynitrides.

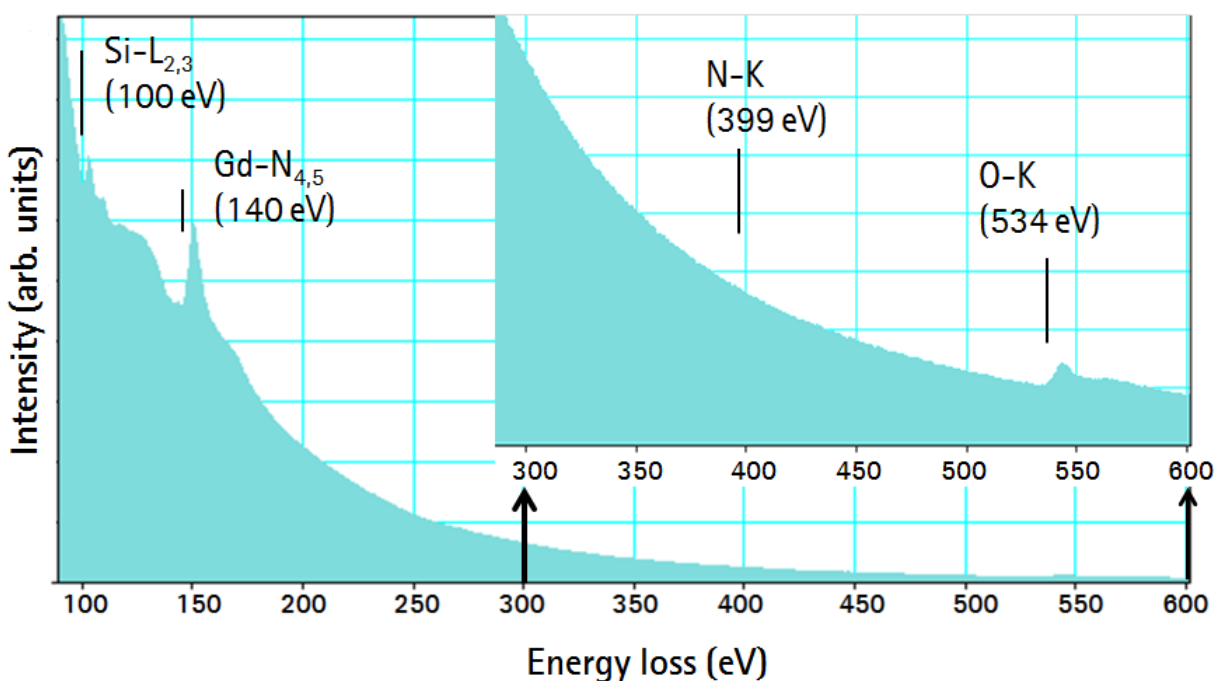


Fig. 5.6: EELS - Plan-view (*Prof. Feldhoff, Institute for Physical Chemistry and Electrochemistry)

5.2 Nitrogen and N₂O plasma during growth

Because the introduction of neutral N₂O gas during layer deposition was not successful, we tried in a second set of experiments the use of activated nitrogen containing gases (N₂O as well as N₂). Plasma excitation is one of the most favored methods due to diverse selecting process parameters.

5.2 Nitrogen and N₂O plasma during growth

A number of operating process parameters must be controlled in order to successfully carry out the nitridation process.

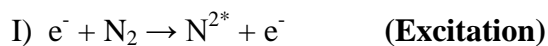
Oxford Scientific radio frequency (RF) plasma source in MBE system is used for this nitridation process. The basic operating principle is that the RF energy is used to create gas plasma from which neutral species are allowed to effuse out into the vacuum chamber. RF energy with a frequency of 13.56 MHz is generated and RF power supply is inductively coupled into the plasma tube. Once the RF supply is turn on, the output power is set to ~50 W. Fine tune of gas flow and RF power is required. Each time the RF power is adjusted or the pressure changed in the source will be tuned again. Power is increased in steps not more than 50 W at a time. Then i allow the temperature to stabilize at each power step increase. This plasma source can mainly operate in two different modes:

Low brightness mode (LBM): when i allow the gas flow by turn on leak valve, the pressure is increased and a dull red glow is noticed in the plasma chamber. This is low brightness mode which indicates capacitive coupling to the RF field.

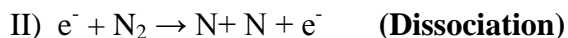
High brightness mode (HBM): When LBM once appears, the pressure will be reduced. When the pressure falls the plasma brightness will suddenly increase to a brighter level which is known as high brightness mode that indicates inductive coupling.

Once the plasma has been successfully ignited i wait for 10-20 minutes for making the temperature stable. All operations of plasma source were performed according to the instructions in the Oxford scientific RF plasma source operating manual.

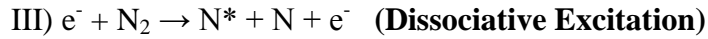
According to F.W.Doss et al. [138] there are several competing reactions that occur while activating N₂ plasma. Incorporating only main reaction steps, it obtained a series of six reactions.



Reaction I shows the electron excitation of the N₂ molecule to any neutral excited molecular states.



The second reaction results in the formation of two ground state atoms



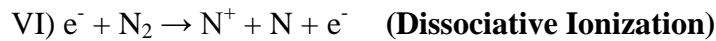
Associated with the break-up of the N_2 molecule into two nitrogen atoms results in the formation of one metastable nitrogen atoms and one ground state N atom.



Reaction IV concerns the ionization of atomic nitrogen.



This reaction describes the ionization of the nitrogen molecule, producing the molecular ion N_2^+



Reaction VI involves both the break-up and subsequent ionization of a nitrogen atom.

5.2.1 Sample Preparation

Gd₂O₃+N₂ Plasma sample preparation

After standard cleaning process Si (111) substrate is introduced into the load lock and after 90 minutes the wafer was transferred to the deposition chamber. Si Substrate annealed at high temperature for the surface preparation process. The substrate temperature were fixed as 720°C and prepared surface for 15 minutes. Clean and well- ordered 7x7 reconstructed surface is observed on RHEED. For the growth process substrate temperature reduced to $T_s \sim 650^\circ\text{C}$ and evaporated commercially available granular Gd_2O_3 material using an electron beam evaporator with a gun power of 11%. Simultaneously for nitridation process, activated N_2 plasma source and set parameters as follows:

- Forward Power = 595 watt
- Reflective power = 0-3 Watt
- Flow rate = 3.03-3.4 sccm
- Substrate Temperature = 650°C
- Partial pressure = $4.3 \cdot 10^{-6}$ Torr
- Duration = 30 minutes

5.2.2 Results

The substrate temperature in the manipulator reduced to 300°C and waited for reaching the base pressure to the power of 10^{-10} Torr. Sample then subjected for further characterization methods.

Gd₂O₃+N₂O Plasma sample preparation

Following the same cleaning and surface preparation steps at 720°C, Gd₂O₃ growth process at 650°C also performed in the previously described manner. Here we made the following changes in the parameters of N₂O plasma.

- Forward Power = 400 W
- Reflected power = 0 W
- Flow rate = 3.03 sccm
- Partial Pressure = $1.6 \cdot 10^{-6}$ Torr
- Duration = 30 minutes

The power had to be reduced because for the used plasma source, if using it with oxygen it is necessary to use not more than 400 W of RF power.

5.2.2 Results

Samples were then characterized using X-ray diffraction, X-ray photoelectron spectroscopy and Atomic force microscopy. The sample thicknesses were estimated using X-ray reflectometry.

X-ray diffraction results:

XRD scan for samples which are nitrided using N₂O and N₂ plasma are shown in fig.5.7. Substrate peaks are in the position where we expect it but there is a change obtained in oxide peak. To be more precise, the sample which is nitrided using N₂O plasma shows a slight shift in Gd₂O₃ (444) peak position which follows the same trend as previous nitridation steps. The peak position for Gd₂O₃ (444) after nitridation is at $\sim 58.4^\circ$. That means a shift of $\sim 0.7^\circ$ which is comparatively lower value compared to the growth under N₂O (2° shift). But the XRD pattern of sample that is nitrided using N₂ plasma doesn't follow the trend like shifting the oxide peak

towards lower 2θ degree. Instead it shows some additional peaks which matches to the formation of polycrystalline GdSi_2 . The additional peak obtained at $2\theta = 29.86^\circ$ matches the formation of GdSi_2 (103) and peak at 62.1° results in the formation of GdSi_2 (215) orientation which has a Pearson symbol of oI12. [139] The thickness of the films were estimated as 21 nm for sample nitrided using N_2 plasma and 9.3 nm for sample nitrided using N_2O plasma. The growth rate was different for these two samples. There is no additional oxygen supply which we followed during the growth of standard Gd_2O_3 . Hence the surface quality is yet to be investigated. All the peak values in XRD and XPS measurements were obtained after peak fitting and the fitted peak were not included in all results.

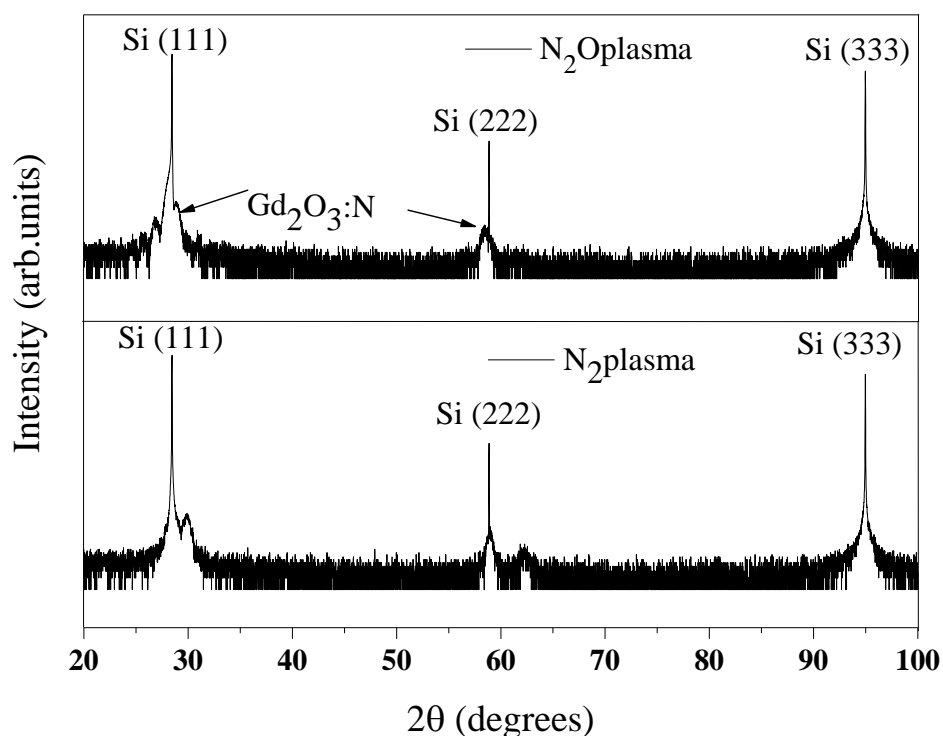


Fig. 5.7: X-ray diffraction pattern of samples nitrided using N_2O and N_2 plasma

Surface morphology:

The influences of nitrogen/nitrous oxide plasma on the surface morphology of Gd_2O_3 films were examined by the AFM, as shown in figure 5.8.

5.2.2 Results

This sample ($\text{Gd}_2\text{O}_3+\text{N}_2$) shows very rough surface in AFM investigations. The root-mean-square (RMS) roughness is estimated as 2.07 nm. In addition to that white clusters are seen on the surface. But the sample nitrided using N_2O plasma gives a RMS roughness of 0.198 nm. Of course, here we have to consider also the differences in layer thickness (21 nm for the rough N_2 -growth, and only 9.3 nm for the smooth N_2O -growth).

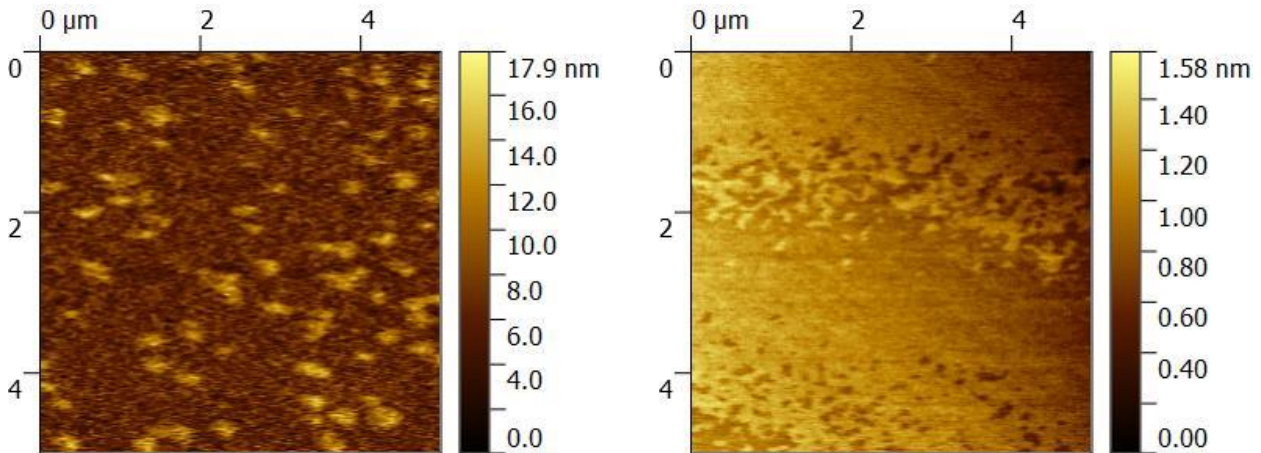


Fig. 5.8: AFM surface morphology of samples nitrided using N_2 (left) and N_2O plasma (right)

XPS results:

The influence of nitrogen in the bonding structure of Gd, O and N were studied using X-ray photoelectron spectroscopy. There is no nitrogen peak in the N 1s level. Here in figure 5.9 depicts the XPS spectra of Gd 4d and O 1s levels of samples nitrided using N_2 and N_2O plasma.

Gd 4d level obtained a peak at 141.9 eV and 142 eV for both samples which shows a shift towards lower binding energy which indicates the bonding of Gd with a lower electronegative element but O 1s level gave a peak at ~531 eV in both conditions agrees with the formation of Gd-O bond. [124] O 1s level shows no nitrogen incorporation whereas Gd peak shift towards lower value of binding energy. Gd 4d and O 1s peak shifts are optimized using C 1s peak.

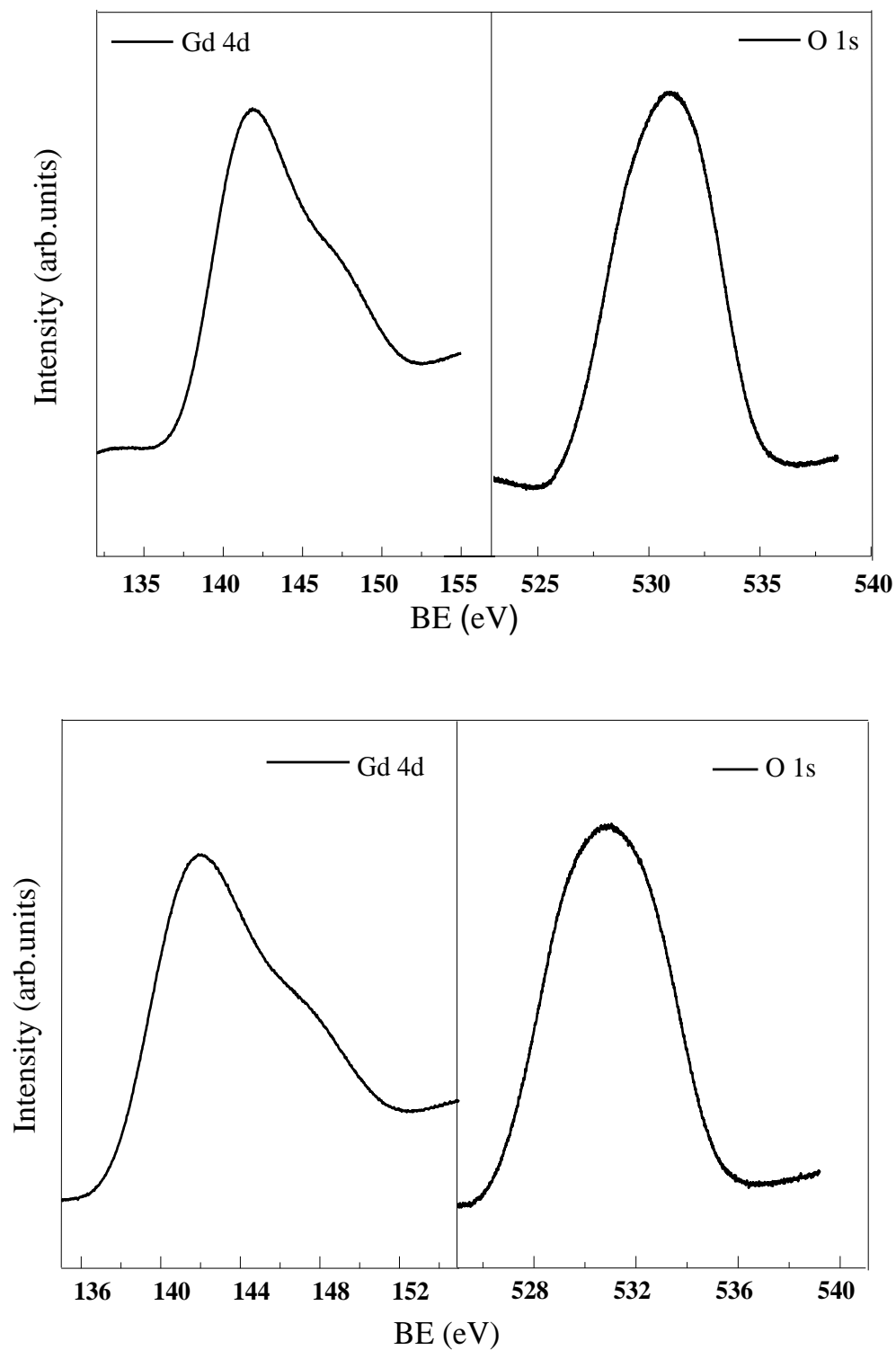


Fig. 5.9: XPS investigations of samples nitrided using N_2O (top) and N_2 plasma (bottom)

5.3 Exposure to activated NH₃

The third approach is the following: First i grow a standard Gd₂O₃ layer using molecular beam epitaxy. That layer will then be exposed to activated NH₃ in a plasma-enhanced chemical vapor deposition (PECVD) system. PECVD is a process used to deposit thin films from a gas state (vapor) to a solid state on a substrate. Chemical reactions are involved in the process, which occur after creation of plasma of the reacting gases. Beck et al. [130] showed different methods for preparing ultrathin silicon oxynitride films for CMOS technology. They demonstrated that growing oxynitride layers by means of PECVD appears the most flexible in this comparison. On top of that, the incorporation of nitrogen in these layers can be the highest by PECVD method. They also claimed that the use of ammonia in a low-temperature process has, however, another consequence, too. Oxynitride layers formed in this way exhibit unusually high concentration of hydrogen. Thus, in order to improve the quality of the dielectric films in question, high temperature annealing (usually RTA) is a solution.

It is known that ammonia (NH₃) can donate an electron pair to form a chemical bond in relation to a reaction. Plasma activated ammonia should even be more reactive, thus the hope was to enforce an exchange reaction in the gadolinium oxide (nitrogen replaces oxygen + filling of vacancies by nitrogen).

Oxford Plasmalab 90 PECVD system is used for our investigations. The main parts of the system are:

- RF generator and network
- Pre-chamber and sample load lock
- Main process chamber
- Temperature controller
- Valve controller and cooling system

5.3.1 Sample preparation

Si (111) substrate was cleaned by using HF and UV/ozone and introduced into the load lock of high vacuum DCA mbe system. Wafer then transferred to the

deposition chamber for the growth process. For the growth of buffer layer on Si (111) substrate the parameters were set as:

Substrate temperature $T_s = 790^\circ\text{C}$

Si evaporation with a gun power = 12.5%

Duration = 10 minutes

Growth of oxide layer on Si (111), parameters were:

Growth temperature = 650°C

Evaporating commercially available granular Gd_2O_3 with a gun power = 11.4 %

Passed additional oxygen using a piezo-leak valve with a partial pressure $P_{\text{O}_2} = 5 \cdot 10^{-7}$ Torr.

Duration = 45 minutes.

Sample is then taken out and carried in a safer way for nitridation process, but there is some possibility of contamination.

Nitridation Parameters:

- Temperature = 400°C
- Pressure = 600 mTorr
- Power = 100 W
- Ar = 200 sccm
- NH_3 = 30 sccm
- Time = 30 minutes

5.3.2 Results

Samples were characterized using X-ray diffraction method, X-ray reflectometry, x-ray photoelectron spectroscopy and Atomic force microscopy (AFM).

Structural Characterization:

Figure 5.10 shows the X-ray diffraction pattern of the sample before and after nitridation process. Before nitridation process the sample shows epitaxially grown gadolinium oxide layer on

5.3.2 Results

Si (111) substrate. The Gd_2O_3 layer on the Si (111) substrate also exhibit single orientation without any indication of disoriented crystallites. The peak at 59.4° corresponds to Gd_2O_3 (444) which match to the literature values. [123] After nitridation process the XRD pattern shown here in red color defines a clear shift in the standard Gd_2O_3 (444) peak. The shifted peak is at 56.5° which gave an idea of approximately 3° shift towards lower 2θ value. There is a change in the intensity and the position of the peak which indicates the changes in the content of the simple cell and dimension of the simple cell respectively. Changes in the interplanar spacing d which points to the effect of doping, decreasing crystal size, etc. The additional peaks that obtained after NH_3 nitridation shows polycrystalline gadolinium silicide formation with different structures. The peaks and their corresponding chemical formulas were obtained from NIMS (National institute of material science) X-ray diffraction database [140] is shown in table 5.1. The thickness of the layer is estimated as ~ 19 nm by using XRR and ellipsometry techniques. Difference of shift from expected value in Gd_2O_3 (222) and Gd_2O_3 (444) is not the same.

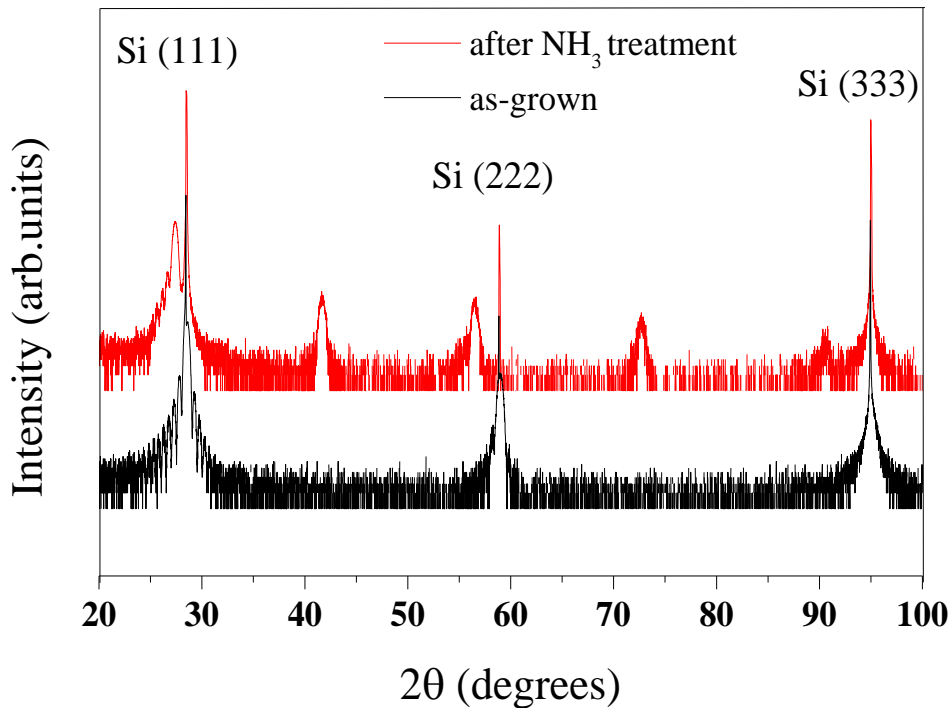


Fig. 5.10: XRD patterns –before and after NH_3 nitridation process

| Peak(°) | Chemical Formula | Miller Indices h k l | d-spacing | Pearson symbol | structure |
|---------|--|-------------------------|-----------|----------------|--|
| 27.4 | Shift in Gd ₂ O ₃ (222) towards lower 2 Θ | | | | |
| 41.66 | Gd ₂ Si ₃ N ₄ O ₃ [141] | 3 1 1 | 0.2171 | tP24 | (Ca _{0.5} La _{0.5}) ₂ Ga ₃ S ₇ |
| 56.5 | Shift in Gd ₂ O ₃ (444) towards lower 2 Θ | | | | |
| 72.75 | Gd ₅ Si ₃ [142] | 3 3 2 | 0.1299 | hP16 | Mn ₅ Si ₃ |
| | GdSi ₂ [139] | 2 1 2 | 0.1084 | hP3 | AlB ₂ |

Table 5.1: XRD peaks with corresponding chemical formula and miller indices

Surface Morphology:

AFM image shows very good surface quality with a root mean square roughness $R_{\text{rms}} = 0.8$ nm. After NH₃ treatment there is an increase in thickness of the layer by ~1nm confirmed by ellipsometry. The expected step height for Si (111) is 0.3 nm. [126] The measured step height after NH₃ exposure is ~ 0.3 nm when the first step is considered. The surface also shows some defects (holes) are shown here in figure 5.11.

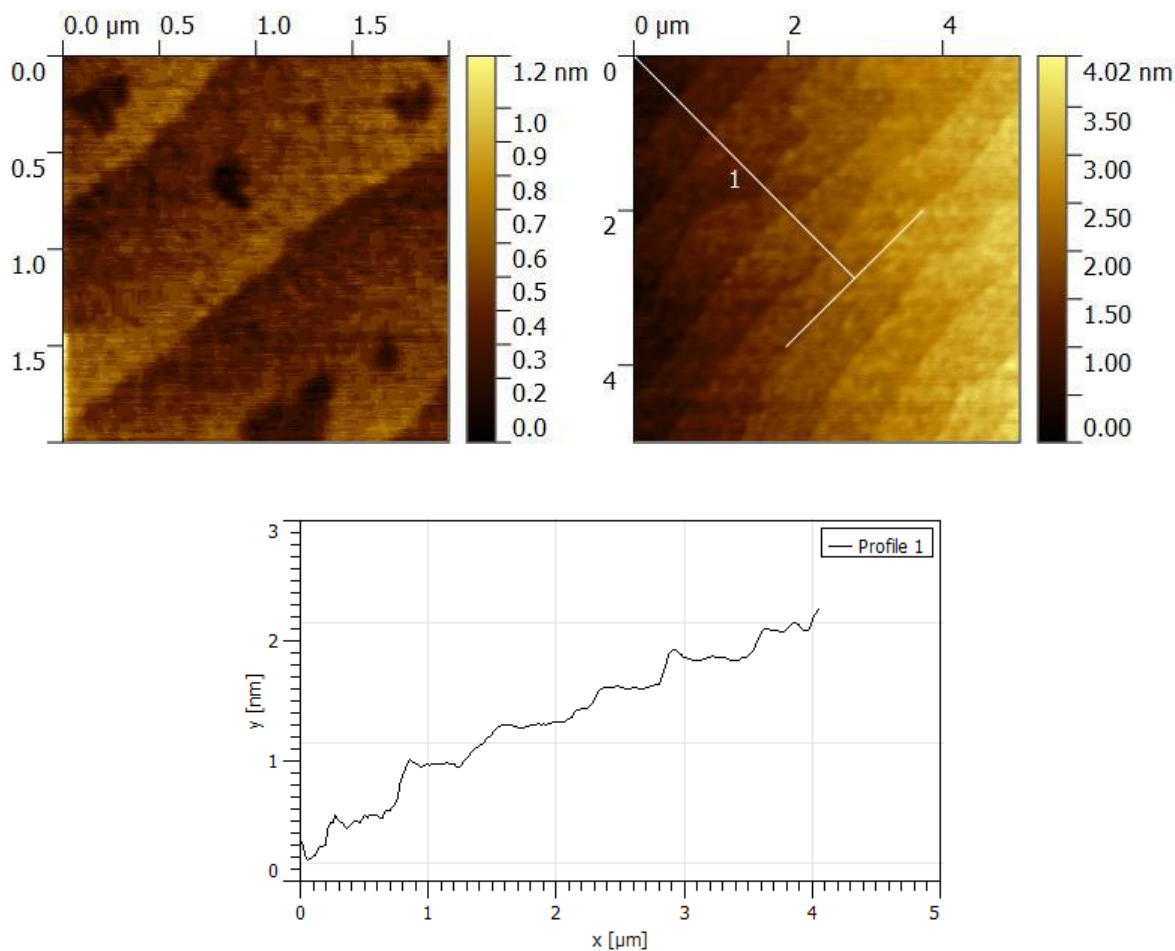


Fig. 5.11: AFM surface morphology after NH_3 nitridation process with white marked area for line scan and scan profile

XPS Results:

Figure 5.12 shows the X-ray photoelectron spectroscopic results of Gd 4d and O 1s levels. The peak obtained at Gd 4d level is ~ 143.2 eV however, these confirm that Gd metal (140.0 eV) is fully oxidized (Gd^{+3} , 143.2 eV) with corresponding chemical shift of 3.2 eV toward higher binding energy and for O 1s level the XPS peak is at ~ 531.1 eV which agrees well with the literature. [124] A chemical shift will occur when there is a change in the binding energy of a core electron of an element due to a change in the chemical bonding of that element. Since there is no such chemical shift is observed here, the possibility of nitrogen incorporation is negligible.

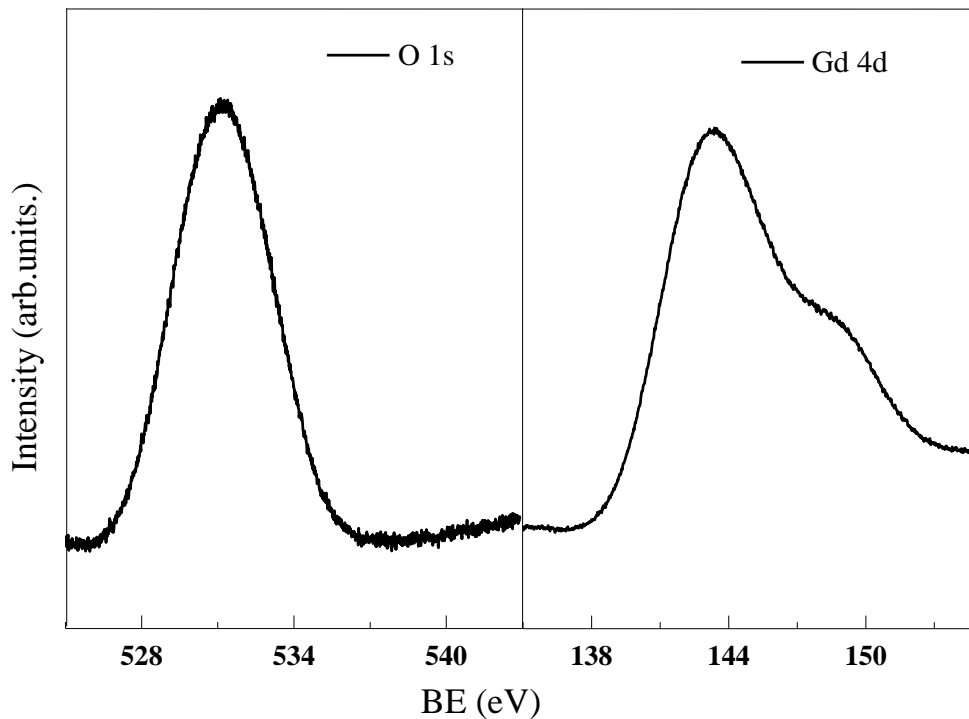


Fig. 5.12: XPS peak of Gd 4d and O 1s levels after nitridation

5.4 Discussion

The incorporation of dopant, that is the incorporation of nitrogen ions by nitridation process is believe to occur by filling the oxygen vacancies or by removing hydroxyl group of ions from Gd_2O_3 . A number of operating process parameters must be monitored and controlled for the successful nitridation process. Different nitridation methods were performed and it found to be very difficult to incorporate nitrogen into the Gd_2O_3 films which were grown epitaxially.

Nitridation using N_2O gas during growth

The basic chemistry while passing N_2O gas is that it decomposes exothermically and reacts with metallic gadolinium in molecular beam epitaxy system resulting in the epitaxial growth of the film which incorporates oxygen and nitrogen along with gadolinium. One of the main advantages

of gas nitridation process is that precise control throughout the growth process by controlling the flow rate of N_2O gas. By different characterization methods the major findings obtained from this nitridation method are:

- XRD results shows a crystalline epitaxial growth (~ 3.5 nm) with a shift in Gd_2O_3 (444) peak toward lower 2θ value. The shift may be due to the incorporation of small amount of nitrogen, OH-groups, or due to some lattice strain during the growth.
- XPS results gave a clear picture that there is no Gd- N bonding whereas it confirms the formation of Gd-O bond. Since there is no chemical shift noticed from XPS investigations, the fact about the amount of nitrogen incorporated is still doubtful.
- TEM investigation shows some interfacial defects inside the film.
- EELS spectroscopy reveals the presence of Gd and O but no nitrogen.

The amount of nitrogen incorporated with this partial pressure of N_2O ($8 \cdot 10^{-7}$ Torr) may be too small to detect by XPS and EELS. The amount of nitrogen may be less than 3 %.

Nitridation using N_2/N_2O plasma during growth

Plasma nitridation is one of the most favored methods due to diverse selecting process parameters. Samples were characterized using X-ray diffraction, X-ray photoelectron spectroscopy and Atomic force microscopy. The results obtained from different characterization methods can be summarized as follows. I obtain epitaxial crystalline growth of Gd_2O_3 on Si (111) which follows the trend of shifting towards lower 2θ degree in N_2O plasma nitridation method. But the trend is different for N_2 plasma nitrided sample. Comparison of results obtained from different characterization method by using N_2 and N_2O plasma is summarized in table 5.2.

Nitridation by activated NH₃ exposure after growth using a PECVD system

X-ray diffraction pattern shows the presence of additional peaks confirmed the formation of polycrystalline GdSi grains. In addition to that there is shift in Gd₂O₃ (222) and Gd₂O₃ (444) peak. AFM image shows very good surface quality with a root mean square roughness $R_{\text{rms}} = 0.8$ nm. After NH₃ treatment there is an increase in thickness of the layer by ~1 nm confirmed by ellipsometry. Gd 4d and O 1s levels in XPS investigation confirms the formation of Gd-O bond. All nitridation process and there results can be summarized as follows (Table 5.3).

| Characterization techniques | N ₂ plasma | N ₂ O Plasma |
|-----------------------------|--|---|
| XRD | <ul style="list-style-type: none"> • Doesn't follow the trend like shifting the oxide peak towards lower 2Θ degree. • Instead it shows some additional peaks which matches to the formation of polycrystalline GdSi₂. • The additional peak obtained at 2Θ=29.861° matches the formation of GdSi₂ (103) and peak at 62.1° results in the formation of GdSi₂ (215). • Thickness = ~21 nm | <ul style="list-style-type: none"> • Shows a slight shift in Gd₂O₃ (444) peak position which follows the same trend as previous nitridation steps. • The peak position for Gd₂O₃ (444) after nitridation is at ~58.4° that means a shift of ~0.7°. • Thickness = ~9.3 nm |
| XPS | <ul style="list-style-type: none"> • No peak in the N 1s level. • Gd 4d level obtained a peak at 142 eV shows a shift towards lower binding energy. • O 1s level gave a peak at ~531 eV confirmed the formation of Gd-O bond. | <ul style="list-style-type: none"> • No N 1s peak. • Gd 4d level obtained a peak at 141.9 eV and shifted towards lower binding energy. • O 1s level peak at ~531 eV. |
| AFM | <ul style="list-style-type: none"> • The root-mean-square (RMS) roughness is estimated as 2.07 nm. • In addition to that white clusters are seen on the surface. | <ul style="list-style-type: none"> • RMS roughness of 0.198 nm. |

Table 5.2: Comparison of results using N₂ and N₂O plasma

| Nitridation Method | Structural evolution | Layer Composition | Surface morphology |
|---|--|--|--|
| N ₂ O gas during growth | <ul style="list-style-type: none"> Crystalline growth. Shift in Gd₂O₃ (444) peak towards lower 2θ degree. | <ul style="list-style-type: none"> Gd-O bond formation. No or less amount of nitrogen incorporation. No traits of nitrogen in EELS spectra. | <ul style="list-style-type: none"> Presence of some defects in TEM images in the interface region. |
| N ₂ /N ₂ O plasma during growth | <ul style="list-style-type: none"> Follows the trend of shifting the oxide peak towards lower 2θ degree (N₂O plasma). Presence of polycrystalline GdSi oriented structures in N₂ plasma mediated growth. | <ul style="list-style-type: none"> Gd 4d level shift to lower BE (~142 eV). O 1s level shows Gd-O bond formation. | <ul style="list-style-type: none"> N₂ plasma- root-mean-square (RMS) roughness-estimated as 2.07 nm RMS roughness of 0.198 nm in N₂O plasma. |
| NH ₃ exposure after growth | <ul style="list-style-type: none"> Polycrystalline structures and shift in oxide peaks | <ul style="list-style-type: none"> Gd 4d and O 1s levels in XPS data confirmed Gd-O bonding. | <ul style="list-style-type: none"> Smooth surface but the presence of voids is detected. |

Table 5.3: Comparison of different nitridation methods

Incorporation of nitrogen into the oxide layer seems to be difficult. The amount of nitrogen incorporated may be too small (<3%) in all these three nitridation process. Ion implantation is another option for nitrogen incorporation which is described in chapter 6.

6 Ion Implantation into epitaxial Gd_2O_3 films

Ion implantation is the process by which ions of a material that are accelerated in an electric field and impacted on a target which causes physical, chemical and electrical changes. The range of the implanted ions in the target depends on the mass of the implanted ions, their energy, mass of the target atoms, the structure of the crystal and the angle of incidence. The basic principle of ion implantation is: [143]

- Generation of ions.
- Ion extraction: ions are extracted from the source due to a high electric field.
- Ion selection: magnetic field mass analyzer selects the appropriate ion.(For some applications, Mass analyzation is not used)
- Ion acceleration: accelerating for giving the ions final kinetic energy.
- Beam scan/disk scan: provides a uniform dose of ions over the wafer surface.

The advantages of the ion implantation process include low process temperature, precise control on dose, short process times, etc. Improvement in the electrical properties of thin films by dopant incorporation has been studied earlier. Sen et al. [27] reported the electrical stability improvement for Lanthanum oxide films by nitrogen incorporation using plasma immersion ion implantation method.

For the nitridation of epitaxially grown Gd_2O_3 layers, i tried different methods which were described in chapter 5. Comparing all these methods, ion implantation seems to be more promising which is detailed in this section. The ion implantation process has wide applications in the doping of semiconductor materials, modification of electronic and photonic materials, etc. Development of accelerator technologies which are capable of delivering high stable and collimated beam currents with a range of few microamperes to 100 mA and incident ion energy ranging from 100 eV to ~10 MeV, have provided a broad and sophisticated technology for integrated circuit (IC) fabrication, electronic devices, optical sensors, imaging devices etc. [144] In addition to the advantages, the ion implantation process also possesses several disadvantages

like channeling, amorphization of the target layer, enhanced diffusion (in particular TED – Transient Enhanced Diffusion), and junction leakage due to implantation damage etc.

A typical ion implanter consists of an ionization chamber where ions are created and an accelerator where they are speed up and boosted enough to impinge on the target. The schematic representation of an ion implanter is shown in figure 6.1. It consists of five main components; (i) the ion source where appropriate ion species are generated; (ii) the analyzer magnet which removes or filters out unwanted ions; (iii) the ion beam accelerator column, which gives the selected ion species its energy; (iv) the horizontal and vertical scanning electrodes which deflect the ion beam electrostatically and allow it to be scanned, across the wafer (v) the target which holds the wafer.

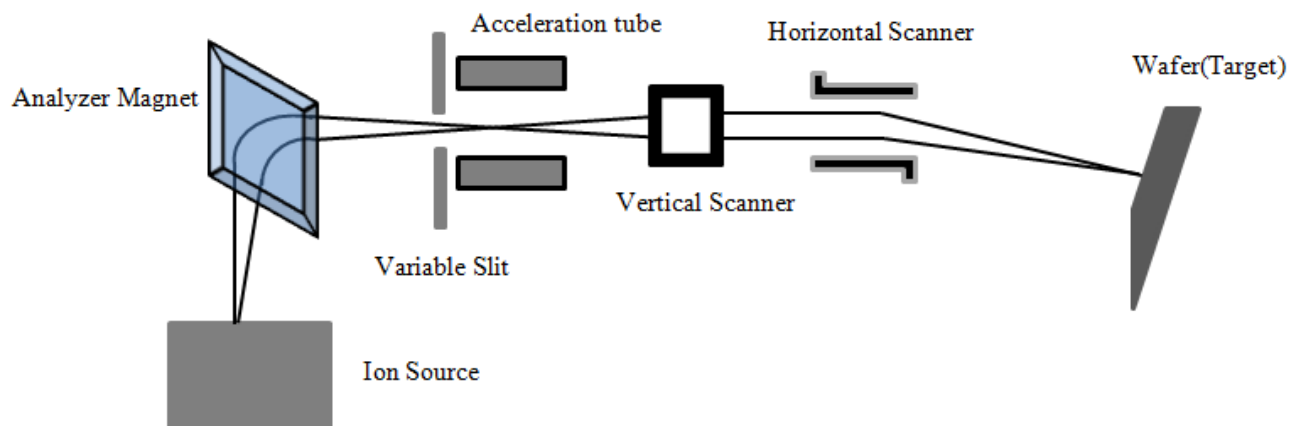


Fig. 6.1: schematic representation of ion implanter

6.1 Ion Implantation process

For the implantation process we use Danfysik A/S, Denmark, Model 1090, 200KV ion implanter and the implantation process was done at Helmholtz-Zentrum Dresden Rossendorf (HZDR), Institute of ion beam physics and materials research.

6.1 Ion implantation process

The ion source is the magnetic plasma discharge/ hot filament that produces a stable beam current. The extracted beam is mass analyzed in a double focusing analyzing magnet. The beam profile monitor and a remotely controlled analyzing slit allow control of the elemental and isotopic purity of the beam. The analyzed beam is post- accelerated to a maximum energy. The accelerator is designed specifically to minimize space charge effects and eliminates expansion of beam in an uncontrolled manner. The beam is then focused such that to minimize instantaneous power loading on the sample surface. With an electromagnetic two-dimensional beam scanning system, the ion beams may be scanned for homogenous exposure over large areas. The tilting and twisting of the sample can be done according to the requirements.

The energy loss mechanism during ion implantation in matter can be explained by two independent processes: nuclear stopping and electronic stopping. Total energy loss is the sum of these two processes.

$$\text{Energy loss rate } \frac{dE}{dx} = -D[S_n(E) + S_e(E)] \quad (6.1)$$

Whereas D is the target atom density, $S_n(E)$ is the nuclear stopping power and $S_e(E)$ is the electronic stopping power.

Nuclear stopping occurs when incident ions interacts with the nucleus of stationary ion. This mechanism is defined as the transfer of energy from an incident ion to a target atom due to inelastic collisions influenced by Coulomb fields that are partially screened by existing electrons. The nuclear energy loss is small at very high energies/velocity. Thus, it tends to dominant towards the end of the range when an ion has lost much of its energy and where nuclear collisions produced most of the damage.

Electronic stopping is the energy loss occurred when the target medium subjected to excite and ionize. The nuclear stopping and electronic stopping strongly depended on the instantaneous energy of the incident ion and on the atomic numbers of the two interacting bodies. Electronic stopping power is dominant in high ion-energy regions, whereas nuclear stopping is dominant in low-energy regions. [145] Figure 6.2 shows schematically the ratio between nuclear and electronic stopping power.

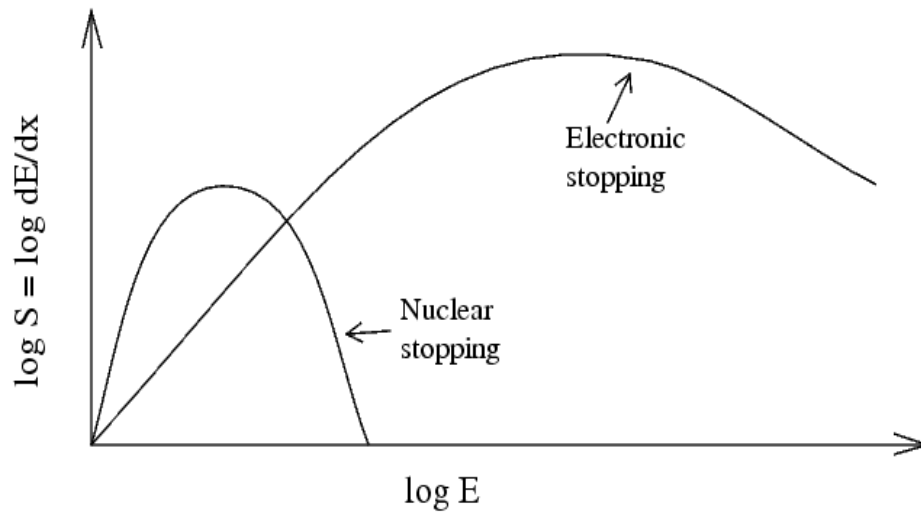


Fig. 6.2: Ratio between nuclear and electronic stopping power

(Image courtesy: <http://beam.helsinki.fi/>)

The ion implantation process may lead to lattice damage - vacancies and interstitial atoms that evolve from simple point defects into complex dislocations or voids, amorphization of the layer, sputtering and ion channeling. Energetic incident ions collide with target atoms, leading to their displacement and the displaced atoms may have energy high enough to displace the target atoms further along its path. Frenkel pair or Frenkel defect is formed when a displaced target atom forms an interstitial and leaves a vacancy behind at its original lattice site. [146] Light ions (lighter than target) with small energy transfer to target atom for each collision generate few displaced target atoms, and ion scattered at large angles. For heavy ions, large energy transfer takes place for each collision and small scattering angle. The displaced atom can further displace other target atoms. Ion channeling occurs when the velocity of the ion is parallel to a major crystal orientation. The presence of screening oxide and a standard tilt angle of 7° reduces the channeling occurring during implantation. Post implantation annealing is needed to activate the implanted ions (bringing them onto a lattice position) and more general to restore the crystallographic structures.

6.1.1 Implantation parameters

Ion implantation process can be carried out successfully by the right choice of implantation parameters. The basic implantation parameters are:

- Dopant species
- Ion beam energy
- Implantation dose or fluence
- Tilt and Twist angle

The penetration depth of the implanted particles is mainly determined by the ion energy, ion species and the composition of target material. The implantation dose determines the number of ions which hit the implantation target. The angle between the wafer surface normal and the ion beam is the tilt angle. A non-zero tilt angle is used to avoid channeling effects.

The implantation parameters were extracted using Stopping and Range of Ions in Matter (SRIM) software. [147] SRIM is a group of programs which calculate interaction of ions with matter. The programs were developed by James F. Ziegler and Jochen P. Biersack around 1983. SRIM is based on a Monte Carlo simulation method, namely the binary collision approximation with a random selection of the impact parameter of the next colliding ion. We need to input the details of incident ion, its mass, energy and tilt angle. In addition to that we need to input the layers of our samples with density, stoichiometry, thickness etc. As the output, it plots the two-dimensional distribution of the ions in the solid, concentration of vacancies, sputtering rate, ionization, phonon production in the target material etc. Transport of ions in matter (TRIM) is the core of SRIM software where we need to add the details of our samples and the incident ion. The basic TRIM window is shown in figure 6.3. The energy of the implanted ion can be varied according to our needs. All simulations in SRIM shown in this chapter were made for implanting nitrogen ions successfully in Gd_2O_3 layer. Considering the sputtering yield and amorphization conditions or

damage events i tried with different energies in order to incorporate the highest possible amount nitrogen in Gd_2O_3 layer and obtained energy of 25 keV with a standard tilt angle of 7° .

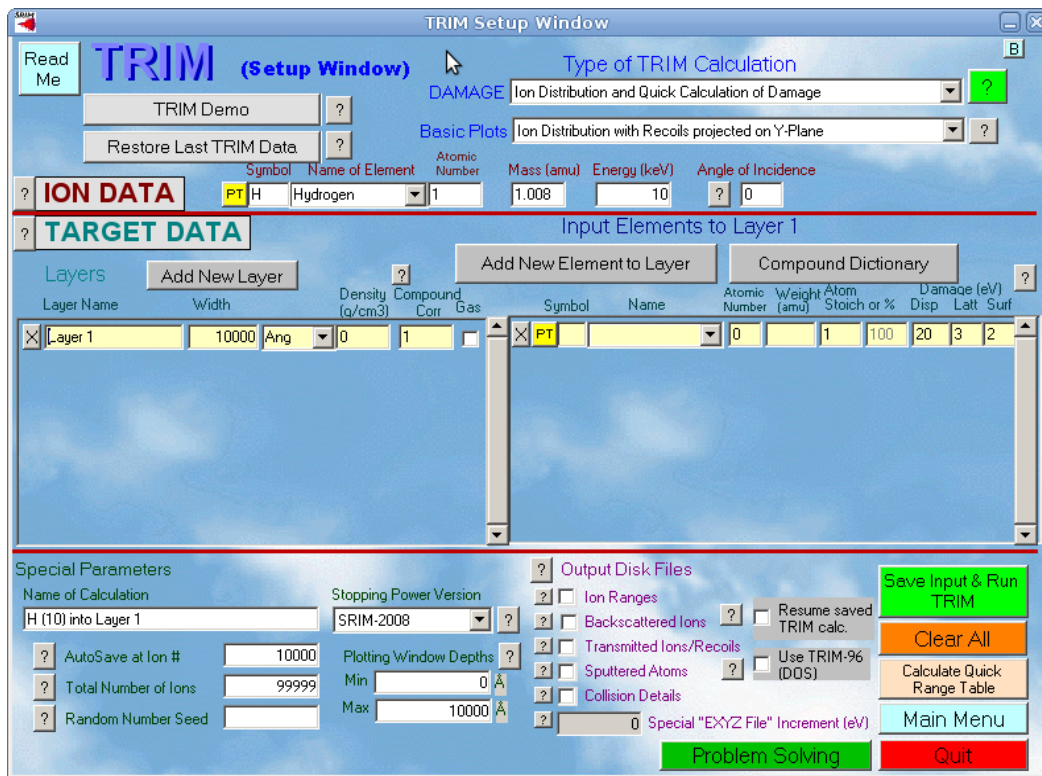


Fig. 6.3: SRIM window for extracting implantation parameters

The layer details that we input here are Si as substrate layer, above that 8 nm thick Si buffer layer then 120 nm thick epitaxially grown Gd_2O_3 layer and on the top 20 nm thick screening oxide (SiO_2) by PECVD method. The implantation profile obtained with energy 25 keV and a tilt angle 7° is shown in figure 6.4. The implantation profile shows the nitrogen ion distribution with the parameters ion range (45.8 nm), skewness (0.1067), straggle (21.3 nm) and kurtosis (2.52). The average penetration depth is called range of ions. Skewness is a measure of symmetry, or more precisely, the lack of symmetry. Kurtosis is a measure of whether the data are heavy-tailed or light-tailed relative to a normal distribution. That is, data sets with high kurtosis tend to have heavy tails.

6.1.1 Implantation parameters

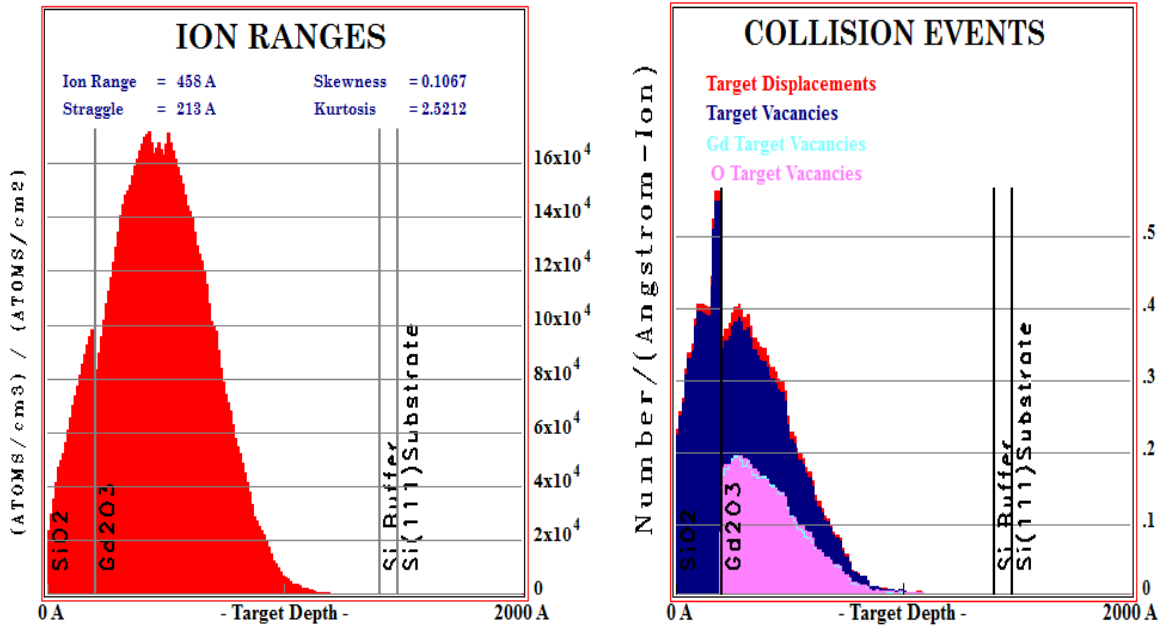


Fig. 6.4: Nitrogen ion distribution profile and damage events on oxide (SiO_2 and Gd_2O_3) layer extracted using SRIM

SRIM also provide the details of damage events. The physics of recoil cascades includes displacement, vacancy, interstitial atoms and replacement collisions. The process where an energetic incident atom knocks a lattice atom off its site is known as displacement. Displacements cause vacancies. Atoms which were knocked out of their original site, and come to a stop in the solid is an interstitial atoms. Also the incident ions, when they stop are considered as interstitial atoms. Target displacements and vacancies in Gd_2O_3 layer is shown in figure 6.4.

When we input the target details, SRIM gives reasonable values as default for displacement energy, surface binding energy and lattice binding energy. Displacement energy is the minimum energy required to hit a target atom far enough away from its lattice site. This minimum energy produces a *Frenkel pair* and a nearby interstitial atom, which is the most fundamental type of damage caused by an ion.

Lattice Binding Energy is needed to remove an atom from its lattice site or it is the energy that every recoiling target atom loses when it leaves its lattice site and recoils in the target. Typically it is about 1-3 eV. The lattice binding energy must be smaller than the displacement energy. SRIM uses the Kinchin-Pease analytic solution for target damage. [148–150]

Target Sputtering:

Sputtering is the removal of near-surface atoms from the target. When a cascade gives a target atom energy greater than the "surface binding energy" of that target, the atom may be sputtered. To actually be sputtered, the atom's energy normal to the surface must still be above the surface binding energy when it crosses the plane of the surface. The sputtering of a surface is described by a "Sputtering Yield", which is defined as the mean number of sputtered target atoms per incident ion. If the target is made of several elements, there is a separate sputtering yield for each element. [151]

Sputtering Yield = (Number of Sputtered Atoms) / (Number of Incident Ions)

For 20 nm SiO₂ and 120 nm thick Gd₂O₃ with nitrogen ion implanted at 25 keV and 7° tilt angle gives a sputtering yield of 1.359 per incident ion. (Obtained from SRIM) So this implantation conditions will sputter off~ 50 nm. The sputter yield also is somewhat lower, but still it has the probability to remove ~49 nm especially the screening oxide. Intermixing between the two layers is found to be negligible from Ion/Recoil distribution plot obtained using SRIM.

Implantation parameters:-

- Implanted species – Nitrogen ion (N⁺)
- Implantation energy – 25 keV
- Dose – 2·10¹⁷, 1·10¹⁷, 5·10¹⁶ atom/cm²
- Tilt angle – 7°
- Temperature – Room temperature

6.1.2 Process Flow

The sample preparation and implantation process were done through a series of processes shown here in figure 6.5

Step 1: wet chemical cleaned 100 mm p-type Si (111) substrate (0.2-0.3 Ωcm) was introduced into the load-lock of MBE system (DCA S 1000).

Si(111)



Step 2:- The wafers were transferred to the deposition chamber and then a Si buffer layer (~8 nm) was grown for 10 minutes at 720°C which shows the transformation of (1x1) surface structure into the (7x7) reconstructed surface. The (7x7) reconstruction indicates clean and well-ordered surface.

Si-buffer layer
Si(111)



Step 3:- The oxide layers with thickness 120 nm were grown by evaporating granular Gd_2O_3 material using an electron beam evaporator. The substrate temperature during growth was set as 650 °C and molecular oxygen with partial pressure $5 \cdot 10^{-7}$ Torr was additionally introduced into the chamber. Surface crystallographic structures were monitored in-situ throughout the process by reflection high-energy electron diffraction (RHEED). The thicknesses of the layers were measured using spectroscopic ellipsometry.

Gd_2O_3
Si-buffer layer
Si(111)



Step 4:- The Gd_2O_3 layers were covered with screening oxide (SiO_2) of 20 nm thickness using PECVD method at $400^\circ C$.

Step 5:- Samples were then subjected to ion implantation. Implantation parameters are energy: 25 keV, fluences: $2 \cdot 10^{17}$, $1 \cdot 10^{17}$, and $5 \cdot 10^{16}$ at/cm^2 , tilt angle: 7° . All implantations were performed at room temperature. The presence of SiO_2 layer and the tilt angle reduces channeling effects in the Gd_2O_3 layer.

Step6:- After the implantation process SiO_2 layer was removed using reactive ion etching (RIE). High energy and high dose nitrogen ion implantation may change the SiO_2 to $SiON$. Hence CHF_3 and O_2 were used in RIE process with a pressure of 0.04 mTorr.

Step7:- Finally, the samples were annealed at $800^\circ C$ in N_2 ambient (1 slm) for 1 minute by rapid thermal annealing (RTA).

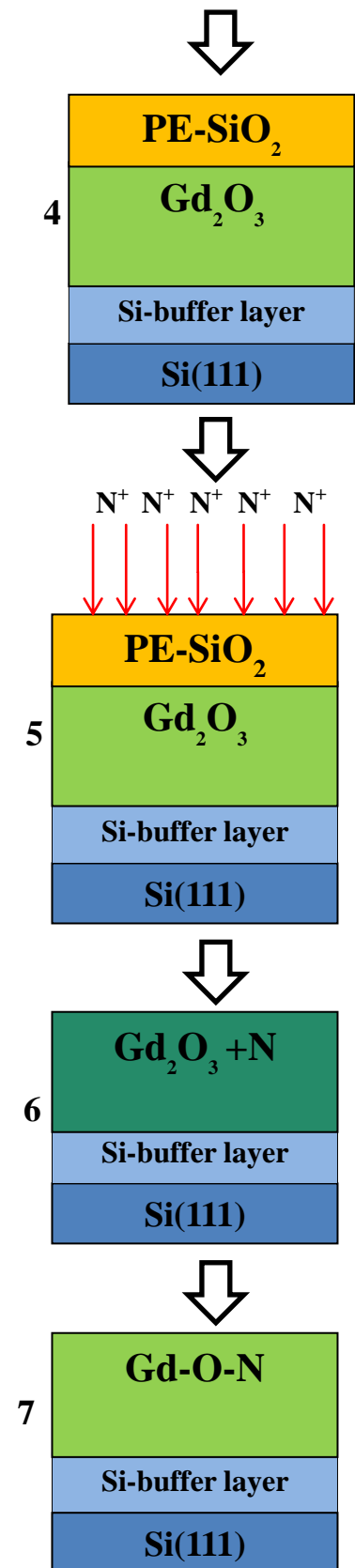


Fig. 6.5: Schematic representation of different process steps

6.1.3 Reactive ion etching

Screening oxide (SiO_2) of 20 nm was deposited on the top of Gd_2O_3 layer. After the implantation process we removed SiO_2 by reactive ion etching method (RIE). High dose and high energy nitrogen ion implantation may change SiO_2 to SiON . Ueno et al. [152] reported the reactive ion etching of silicon oxynitride using CHF_3 . RIE is a type of dry etching technique which combines the plasma and sputter etching process. The RIE process is exclusively anisotropic and etch rate uniformities are typically very good.

ALCATEL-RIE equipment in clean room is used for this process (shown in figure 6.6) with source gases O_2 , Ar, SF_6 , and CHF_3 . The equipment has an RF generator, a matching network and a pumping station as main parts. For removing the 20 nm thick PE- SiO_2 after nitrogen ion implantation we use the following recipe:

- $\text{CHF}_3 = 20$ sccm
- $\text{O}_2 = 2$ sccm
- Pressure = 0.04 mTorr
- Power = 40 W
- Time = 10 minutes



Fig. 6.6: ALCATEL-RIE equipment in clean room

CHF_3 alone has a tendency to readily form fluorocarbon polymers and consequently it is frequently used together with the addition of small amounts of O_2 to suppress this. This changes the nature of the process since the addition of O_2 generates reactive species such as atomic O and atomic Fluorine.

6.1.4 Rapid thermal annealing (RTA)

Ion-implanted crystals will normally contain a great deal of damage in the as-implanted state. Narayan et al. [153] reported that for the recrystallization of amorphous layer, removal of displacement damage and electrical activation of dopants thermal annealing is necessary. When an energetic ion penetrates a solid, it makes collisions with the electrons and the nuclei of the target material. When electronic excitation occurs, energy will be lost as heat. The displacement of atoms from the crystal lattice occurs mainly due to nuclear collisions. Below the critical value of specific damage energy, displaced atoms in the form of simple and complex point defects may cluster to form dislocation loops. [154]

Commercial RTA system is used for our annealing step. Annealing was performed in N₂ ambient with a flow rate of 1slm at 800°C for 1 minute. Czernohorsky et al. [155] reported that the impact of RTA process on structural and electrical properties of crystalline Gd₂O₃ layers grown on Si with different orientations. Due to additional oxygen from the annealing ambient, uncapped Gd₂O₃ layers remain stable only up to 800°C.

6.2 Characterization of N-implanted Gd₂O₃ layers

In this section, I summarize our findings for the samples obtained after different processing steps. The thicknesses of the layers (~120 nm) were measured using spectroscopic ellipsometry. XRD measurements (Bruker, D8 Discover) give an idea about the crystalline properties of the implanted layer. The samples were also investigated with Raman spectroscopy (via Raman microscope from Renishaw) using 633 nm light as excitation. Samples were again loaded into the ultra-high vacuum system (UHV) and transferred to analysis chamber for XPS measurements. Mg K α radiation (h ν =1253.6 eV) was used for the excitation of photoelectrons. XPS data were collected from gadolinium (Gd) 4d, oxygen (O) 1s and nitrogen (N) 1s levels. Cross-sectional TEM (FEI Tecnai G2 F20) investigations were used to explore the changes in Gd₂O₃ layer due to varying doses. The findings after ion implantation are already published. [156]

6.2.1 Structural evolution

TEM Investigation:

First, the samples were investigated using cross-sectional TEM (done by Dr. Dominic Tetzlaff). The bright-field overview image of the Gd₂O₃ with the highest implantation dose shows a very rough surface layer (Figure 6.7 (a)). Additionally, bright areas parallel to the surface / interface are visible in the upper half of the film while the lower area appears to be undisturbed. These cracks present in the Gd₂O₃ layer look similar to the findings of McKenzie et al. [157] in thin GdN layers. These cracks can be found in all implanted Gd₂O₃ films with similar quantities, which are not in dependence of implantation dose. No cracks were found in standard Gd₂O₃ sample without implantation. Therefore, crack formation must occur during nitrogen implantation. Using higher magnification (Figure 6.7 (b)), the thickness of the undisturbed area can be estimated at 45 nm while the disturbed region is about 97 nm thick. The simulated implantation profile is superimposed on the TEM image aligning the interface between silicon oxide and Gd₂O₃ (screening oxide for implantation, removed prior to annealing) at the surface of the layer. The implantation profile matches the thickness of the disturbed region, proving the structural changes are due to the implantation of nitrogen. High-resolution TEM images of the disturbed area (Figure 6.7 (c)) show variations in contrast aligned to the crystal lattice planes with lengths of up to 10 nm. The brighter contrast can be due to lower density or even lack of material compared to the surrounding matrix. Fast Fourier transforms of images of the disturbed and undisturbed regions show no significant differences. Only slight variations of the spot distances are visible indicating small variations of the lattice spacing in the disturbed area. Considering the brighter contrasts in Figure 6.7 (c) it may be due to incorporation of nitrogen results in the reduction of lattice spacing. If we consider instead the formation of voids due to strain [158] the layer can elastically relax around these voids changing the lattice spacing.

In addition, there is an amorphous interfacial double layer (~6 – 7 nm) present (Figure 6.7 (b)) for all samples after annealing. To explore the origin of that interfacial layers, we compare high-resolution TEM images of the interfacial region for an as-grown Gd₂O₃ layer (Figure 6.8 (a)) and a layer after annealing, but without implantation (Figure 6.8 (b)). Two different contrasts with a sharp interface can be seen within the interfacial layer, whereas the bright contrast layer (~ 2.5 nm) is close to the substrate, and the darker contrast layer (~3.7 – 4.5 nm) is close to the Gd₂O₃

layer. As shown earlier for non-optimized Gd_2O_3 growth, these interfacial layers are composed of SiO_2 (at the bottom) followed by a silicate-like layer. [155]

In summary, high-dose implantation of nitrogen into single crystalline Gd_2O_3 followed by RTA leads to the formation of cracks can be compared to the voids/cracks present in the TEM findings of gadolinium nitride layers. [157] The crystal structure is disturbed by the formation of small regions (up to 10 nm wide) parallel to the surface / interface that could either be areas with lower densities due to nitrogen incorporation or even voids.

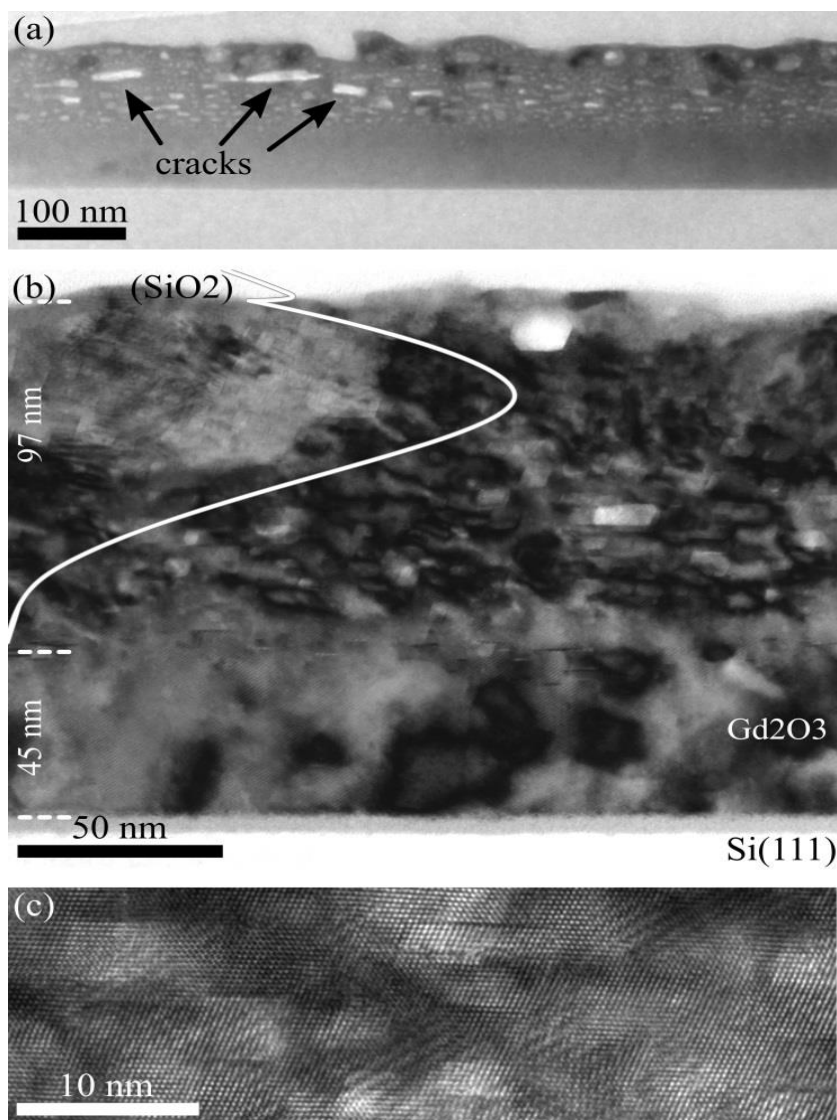


Fig. 6.7: TEM analysis of the sample with highest implantation dose: a) bright-field overview image, b) bright-field with overlaid simulated implantation profile, c) high-resolution image of disturbed area.

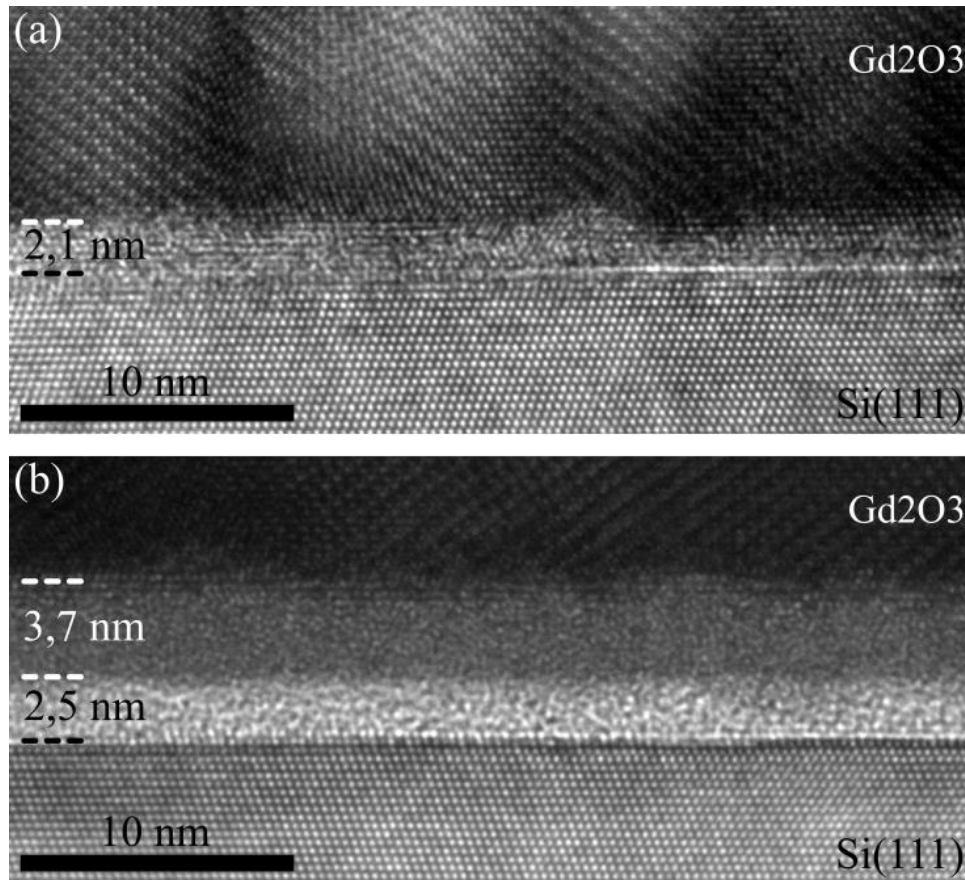


Fig.6.8: Cross-sectional TEM images of a) as grown Gd₂O₃ layer on Si (111), and b) after RTA (800°C, 1 min, N₂ ambient 1 slm)

Raman Spectroscopy:

Next, I use Raman spectroscopy to find the structural changes during the different processing steps, focusing on the sample with the highest implantation dose. Figure 6.9 (a) summarizes some findings. It shows Raman spectra of the layer with the highest implantation dose after different processing steps. The Raman spectra are restricted to 250-400 cm⁻¹ where I expect Gd₂O₃ peak according to the literature value. Also I did some wider scans which do not have any peaks other than silicon. The upper spectrum was obtained from the as-grown Gd₂O₃ layer. Besides the known silicon band at 302 cm⁻¹ [94, 95], I find a band at 361 cm⁻¹ which can be assigned to a vibrational mode in cubic bixbyite Gd₂O₃. [94] That mode intensity nearly disappears after high-dose ion implantation due to partially disturbed crystal structure accompanied by a reduction in the thickness of the remaining crystalline oxide layer. After annealing at 800 °C, a mode in that region clearly appears again, however, it is shifted to lower wave numbers and shows a decrease

in intensity compared to the as-grown case. Thus, the layer has been recrystallized, but in another structure/composition. For pure rocksalt GdN, a Raman peak should be expected at 530 cm⁻¹ and a weak shoulder at 350cm⁻¹. [158] But both these Raman bands are not visible due to the presence of high intensity silicon bands at 520 cm⁻¹.

The Raman results show that the new crystalline phase can neither be Gd₂O₃ nor GdN in their common bulk structures. From the TEM results, it is clear that after implantation the undisturbed Gd₂O₃ layer has still a thickness of around 45 nm. To find answer for the question, why i do not see that part in the Raman spectra (as-implanted sample) i measured the intensity variations of Raman bands of cubic bixbyite Gd₂O₃ in dependence on the thickness of the oxide layer. Crystalline Gd₂O₃ layers which were grown epitaxially on Si (111) substrates with Gd₂O₃ thicknesses between 35 and 155 nm were studied in detail (figure 6.9 (b)). The 155 nm thick oxide layer shows a strong Raman band at 361 cm⁻¹; and the intensity of the band decreases according to the reduction in the thickness of the layer. Sample with 35 nm oxide layer shows no Raman band at 361 cm⁻¹ whereas i observed a very weak peak for the oxide layer with thickness of 42 nm (difficult to see in this scale, hence not included in the results). Only the undisturbed part of the Gd₂O₃ layer shows a Raman peak after implantation, while the implanted region does not deliver any intensity. Since the new peak occurring after implantation and annealing has a much higher intensity and is shifted by a few wave numbers, its origin cannot be attributed to the undisturbed part of the Gd₂O₃ layer, but is caused by the newly formed crystalline upper part of the layer.

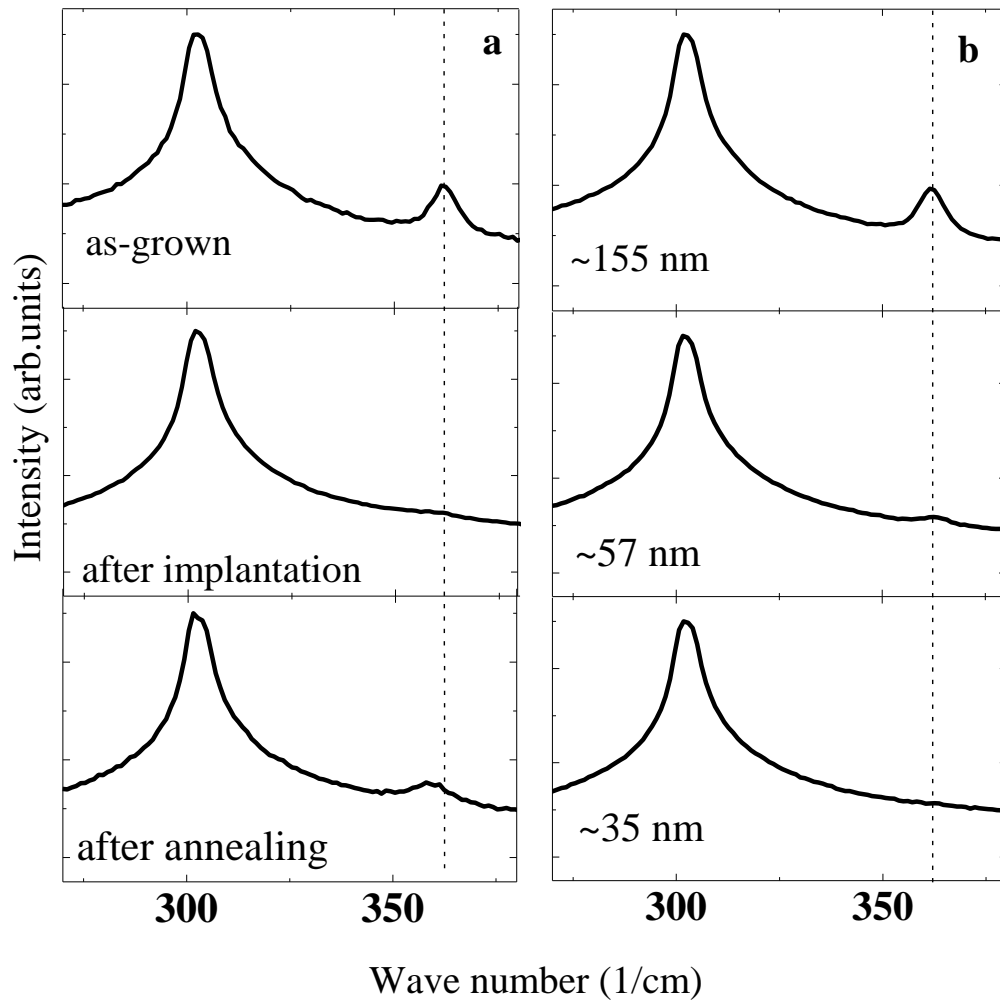


Fig. 6.9: a) Raman spectroscopy of the layer with the highest implantation dose after different processing steps (as indicated) and b) Intensity variations according to thickness for Raman band of Gd₂O₃. The dashed line marked the position of the typical Raman band for Gd₂O₃ (Ref. [94]).

X-ray Diffraction results:

XRD measurements do not exhibit additional phases but i observed a drop in the intensity and broadening of the oxide peak after implantation which should be due to the reduction in thickness of the crystalline oxide layer. (figure 6.10) The strain effects in the Gd₂O₃ layer may additionally be a reason for peak broadening which reduces after RTA.

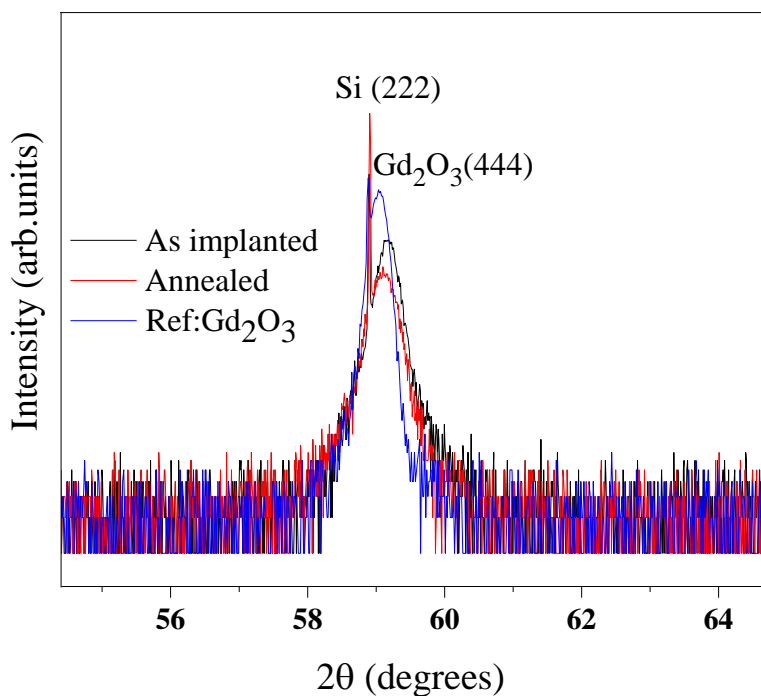


Fig. 6.10: X-ray diffraction pattern of ref. Gd_2O_3 sample, as-implanted and after annealing steps. (All patterns were normalized to the Si (222) peak)

6.2.2 XPS results:

Next, I performed XPS investigations on all samples. The binding energies in the Gd 4d and O 1s levels were estimated using the F 1s peak as an internal reference in all samples. Figure 6.11 a) shows a comparison of the Gd 4d XPS peak of samples having three different doses of nitrogen ion implantation and of a reference Gd_2O_3 sample without ion implantation. The reference Gd_2O_3 sample exhibits a peak at 143.5 eV (Gd bonded to O) which agrees well with earlier investigations. [124] For the implanted sample we can observe a shift towards lower binding energy in dependence on the implantation dose. The sample with highest implantation fluence (or with the highest amount of nitrogen incorporated) shows a peak maximum at 142.3 eV; that is

6.2 Characterization of N-implanted Gd_2O_3 layers

a shift of 1.2 eV towards lower binding energy. Such shift in binding energy indicates that Gd is bonded to a less electronegative element. Electronegativity values of O and N are 3.44 and 3.04, respectively. Thus, the observed peak shift could be due to Gd-N bond formation. The results for the O 1s XPS peaks for the same samples are shown in Figure 6.11 (b). Here it is also observed a shift toward lower binding energies in O 1s peak with respect to the dose. The highest dose implanted sample shows a maximum shift of 1.5 eV. That shift of O 1s level can again be explained by the change of effective negative charges on N and O atoms and the induction effect. When the nitrogen concentration increases in its surrounding, the binding energy of an atom shifts towards a lower value because of the higher surrounding electron density. [159] Hence the observed shift could indicate the formation of Gd-O-N bonding.

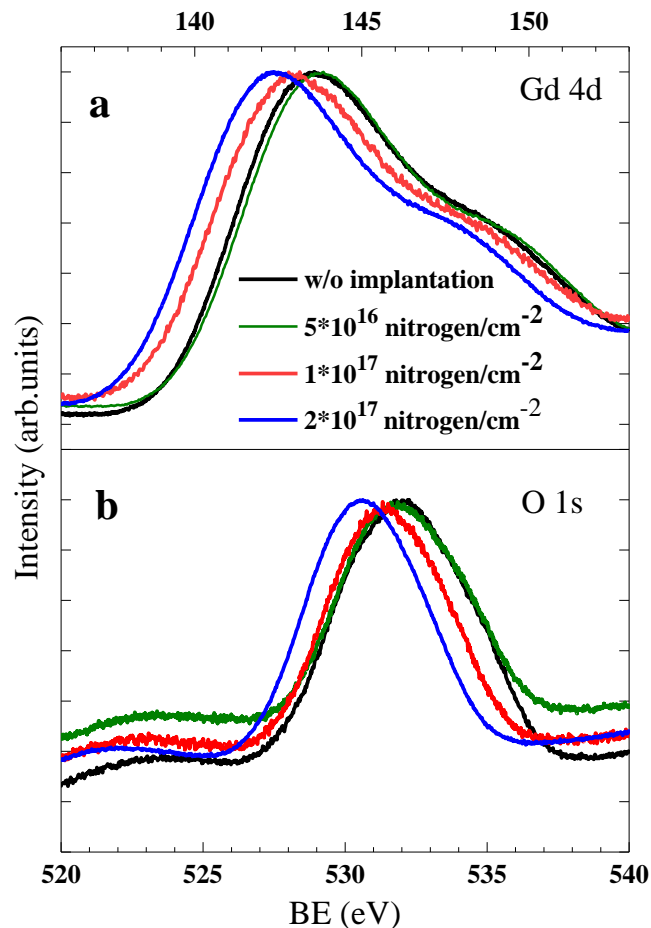


Fig. 6.11: a) Gd 4d and b) O 1s XPS spectra of samples implanted with three different nitrogen doses in comparison to a reference sample without implantation

6.2.3 Band structure:

I use XPS to find band structure changes caused by nitrogen implantation. Figure 6.12 (a) shows the valence band (VB) spectra for high dose implanted sample. The VB offset between the implanted oxide layer and Si was estimated from the known relation [160]

$$\Delta E_V = (E_{CL}^{Ox} - E_V^{Ox}) - (E_{CL}^{Si} - E_V^{Si}) - \Delta E_{CL} \quad (6.2)$$

whereas $E_{CL}^{Ox} - E_V^{Ox}$ is the core level to valence band maximum (VBM) energy difference for the implanted Gd₂O₃ layer and $E_{CL}^{Si} - E_V^{Si}$ is the core level to VBM energy difference for Si. It was reported that the VB offset for single crystalline Gd₂O₃ relative to Si is approximately 2.4 ± 0.2 eV. [21] Here, I obtain VB offsets relative to Si of 1.0 eV, 1.2 eV, and 1.5 eV for high, medium, and low fluence implanted samples, respectively. As shown earlier, already doping of Gd₂O₃ with small amounts of nitrogen leads to a reduction in VB offset with Si (down to 1.7 ± 0.2 eV at $P_{N_2O} \sim 2 \cdot 10^{-6}$ Torr during growth). [21] In case of nitrogen implanted samples I find further reductions in VB offset. According to Ref. [23], the VB offset for GdN to Si should be negligible small. For a better understanding of the effect of nitrogen incorporation on the VB offset of Gd₂O₃ layers on Si, the nature of the VB structure of the binary rare-earth sesquioxides (RES) should be considered. Reports show that in RES the VB maximum is formed mainly by O 2p states. [161,162] Shang et al. [163] demonstrated that when nitrogen is incorporated into different transition metal oxides or rare-earth metal oxides, their upper VB levels are shared between O 2p and N 2p states. As the N 2p states lie above the O 2p states, the VBM shifts towards higher energy, hence VB offset to Si should decrease.

The band gaps of the nitrogen implanted Gd₂O₃ layer using different implantation doses were estimated from the threshold energy of the oxygen 1s plasmon energy loss measurements. [164] As shown in Figure 6.12 (b), the band gap energy for high dose implanted sample is obtained as 2.5 ± 0.2 eV whereas the band gaps are 5.4 ± 0.2 eV and 5.8 ± 0.2 eV for the medium and lowest fluence implanted samples respectively. XPS has a small information depth, i.e. band structure results were obtained from the upper region of the implanted sample and not from the regions with the peak implantation dose. The reported band gap values for epitaxial Gd₂O₃ layers on Si are approximately 5.9 ± 0.2 eV. [7,165] A recent report also shows band gap narrowing for small

6.2 Characterization of N-implanted Gd₂O₃ layers

amounts of nitrogen incorporated into Gd₂O₃ layers; the authors obtained a band gap of 5.2 ± 0.2 eV as the smallest value ($P_{N_2O} \sim 2 \cdot 10^{-6}$ Torr during MBE growth). [21]

The conduction band offset (ΔE_c) can be calculated by using the experimentally obtained values of VB offset and band gap of the oxide layer and the energy gap of the Si substrate

$$\Delta E_c = E_g^{Ox} - \Delta E_v - E_g^{Si} \quad (6.3)$$

For the high fluence implanted layer this yields a value of 0.4 ± 0.2 eV. The XPS investigations reveal that also the conduction band offset between Gd₂O₃ and Si is reduced at high dose nitrogen ion implantation which agrees with the previously reported photoemission investigations on HfSiON gate dielectrics. [16] Jung et al. [166] demonstrated that a reduction in conduction band offset due to nitrogen incorporation can significantly enhance the leakage current conduction in HfO₂. The conduction band offset obtained here disagreed with the previously reported numbers for low nitrogen doped Gd₂O₃ layers which did not show any changes in conduction band offset. [21] It is no wonder that we do not see monotonic changes; the low amount Gd₂O₃:N layers were still single crystalline in the bixbyite structure, whereas our implanted samples show significant structural changes.

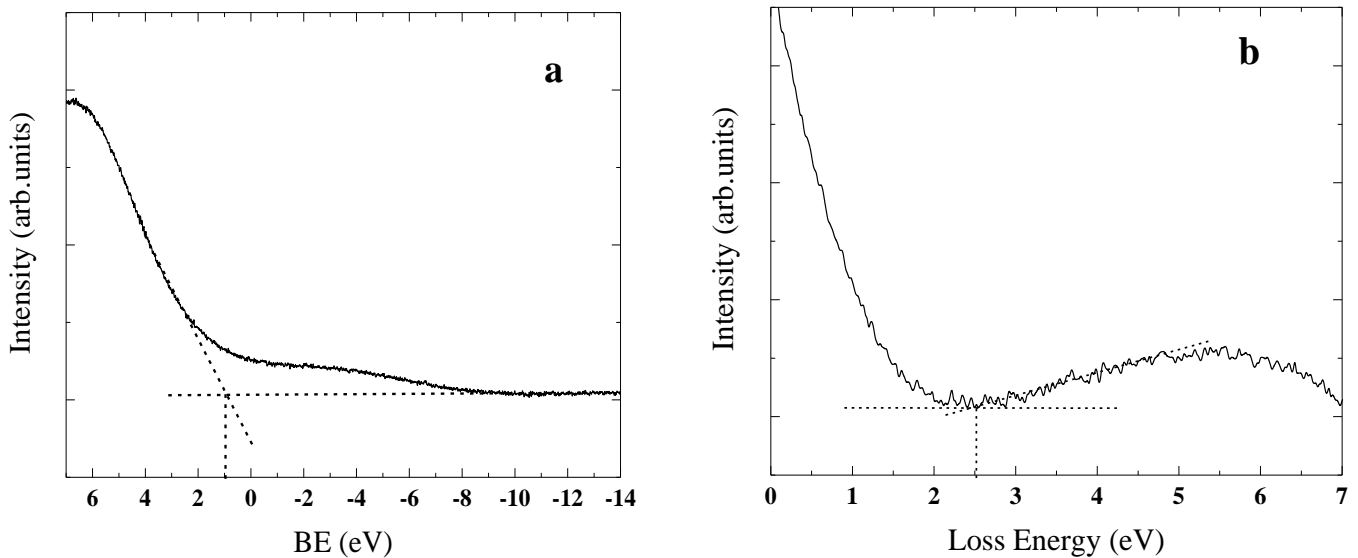


Fig. 6.12: a) Valence band XPS spectra for high dose nitrogen implanted Gd₂O₃, and b) oxygen 1s energy loss spectra for the same sample.

6.2.4 Concentration of Gd, O and N:

Gadolinium, oxygen and nitrogen concentration in high dose implanted sample was obtained using Auger electron spectroscopy (AES), in conjunction with ion sputtering. This characterization was done at the Institute of Energy Research and Physical Technologies, TU Clausthal. For the depth profiling process, i use high dose nitrogen implanted sample with 20 nm SiO₂ and 120 nm Gd₂O₃ which is annealed at 800°C in N₂ ambient for 1 minute.

Sputtering details:

- Ion : Ar⁺
- Energy : 4 keV
- Angle : 38.8° angle of incidence with respect to the surface normal
- Beam current : ~1 μA

Sputter-depth profiling:

The concentration of nitrogen in the interface between SiO₂ and Gd₂O₃ layer and the implanted areas of Gd₂O₃ oxide layer after sputter depth profiling is summarized in table 6.1 and in figure 6.13. Because of the fact that the sputtering rate for Gd₂O₃ is not known, we plotted the depth distribution as a function of sputtering time.

The main observation during sputter depth profiling was the nitrogen distribution in the oxide layer is not uniform. The concentration of nitrogen on the surface of Gd₂O₃ layer or the interface between SiO₂ and Gd₂O₃ layer seems to be around 5 atom %. Going deeper in to the Gd₂O₃ layer i obtained a maximum concentration of 11 atom % of nitrogen. According to the SRIM ion distribution profile, the ion range is at 46.7 nm. The concentration of oxygen seems to be decreasing with increasing nitrogen content which can be explained as a result of preferential oxygen sputtering. It is reported that the incident positive ion causes preferential oxygen sputtering. [167] The atom percentages of all elements were obtained from Auger spectra. (example shown in figure 6.14)

| Sputtered region | Sputtering time(sec.) | Gd (atom %) | O (atom %) | N (atom %) | Ar (atom %) |
|--------------------------------|-----------------------|-------------|-------------|-------------|-------------|
| SiO ₂ | 360 | 54.7 | 39.9 | 5.2 | - |
| Gd ₂ O ₃ | 36 | 54.1 | 39.8 | 3.8 | 2.3 |
| | 72 | 50.7 | 40.2 | 6.9 | 2.2 |
| | 144 | 49.5 | 37.2 | 11.0 | 2.2 |
| | 216 | 48.9 | 39.9 | 8.5 | 2.7 |

Table 6.1: Concentration of Gd, O and N at different sputtering time (Numbers in bold gives maximum nitrogen concentration obtained)

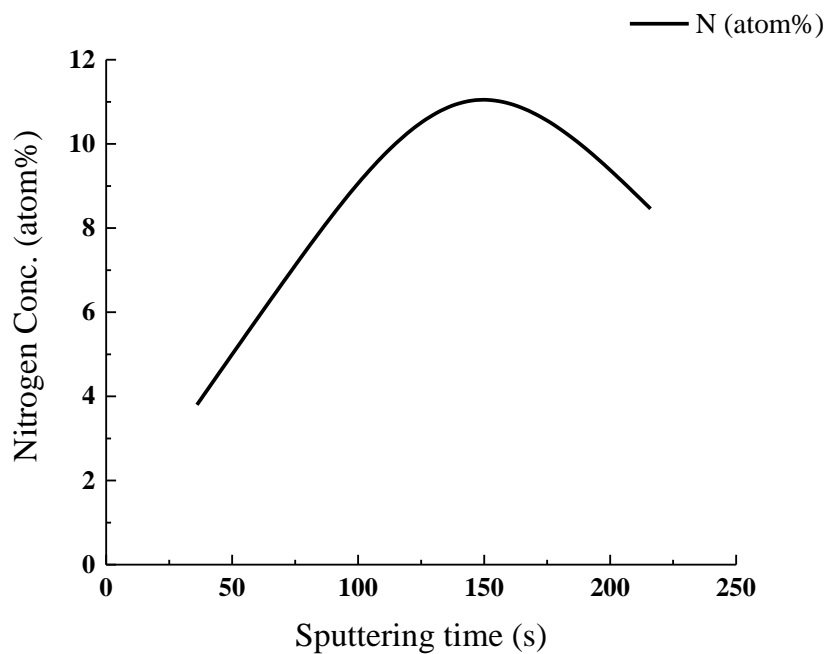


Fig. 6.13: Graph- Sputtering time Vs nitrogen concentration

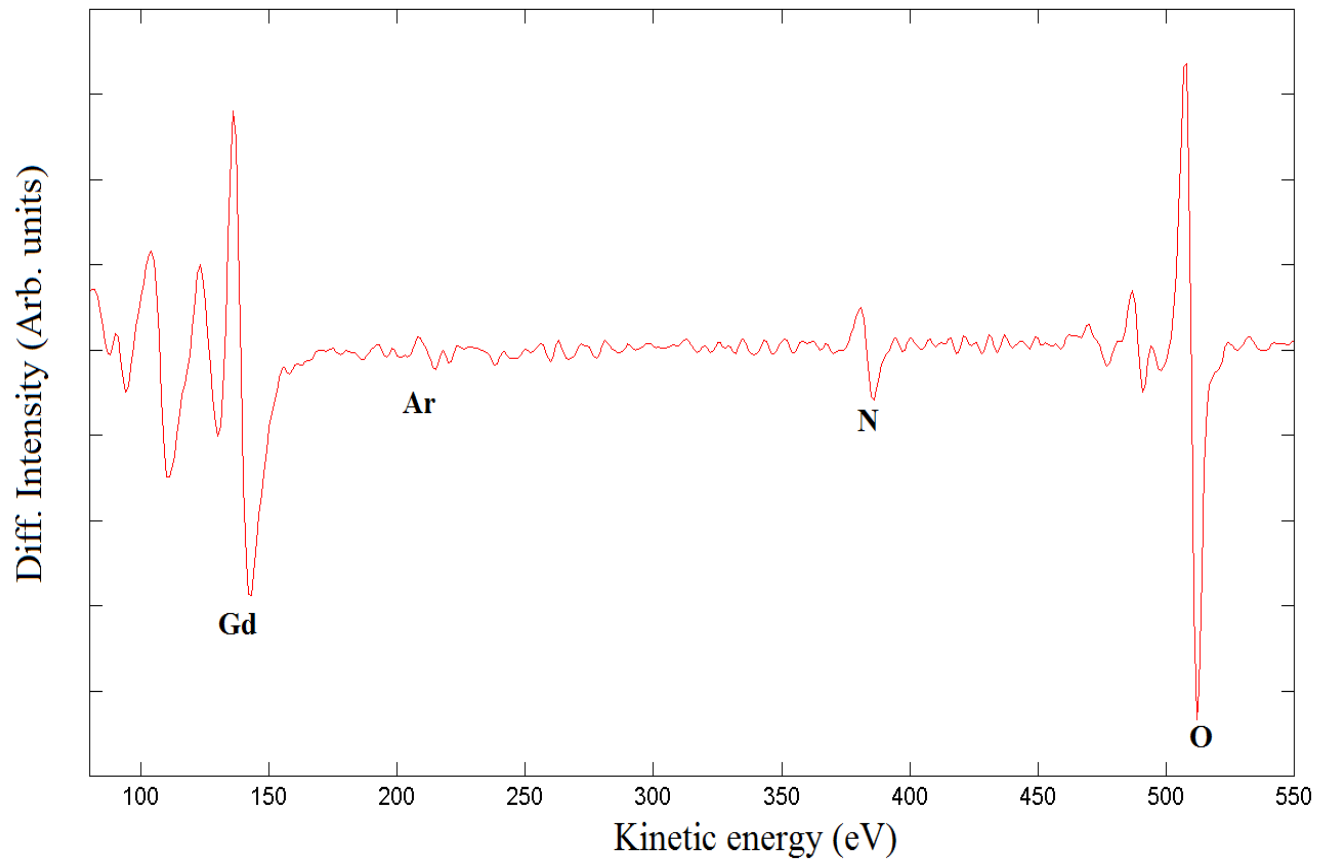


Fig. 6.14: Auger spectra after 72sec sputtering of Gd_2O_3 layer, elements present in the layer were marked in bold letters

6.3 Summary

The effects of nitrogen incorporation by high-fluence ion implantation in epitaxial Gd_2O_3 films on p-type Si (111) followed by annealing have been investigated. The nitrogen incorporation is believed to occur by filling the oxygen vacancies or by removing hydroxyl group ions in Gd_2O_3 . The implantation parameters and the damage events were roughly estimated using SRIM software. The nitrogen content in the oxide layer has been altered by changing the implantation dose.

The 120 nm thick Gd_2O_3 layers were grown using molecular beam epitaxy. Growth were monitored in-situ by reflection high energy electron diffraction (RHEED). Gd_2O_3 layers were covered using 20nm thick screening oxide (SiO_2) deposited by standard PECVD method. Samples were then subjected for nitrogen ion implantation process with 25 keV energy and three different doses ($2 \cdot 10^{17}$, $1 \cdot 10^{17}$, $5 \cdot 10^{16}$ at/cm²). After different processing steps like removing SiO_2 (RIE method) and post implantation annealing (RTA) samples were characterized using different techniques.

TEM structural investigations can be summarized as i) rough surfaces ii) ion implantation results in the formation of cracks in Gd_2O_3 films iii) thickness of the disturbed region is ~97 nm and undisturbed part is ~45 nm iv) implantation profile matches the thickness of the disturbed region v) presence of amorphous interfacial double layer (~6-7 nm) is confirmed and found that it is due to the RTA process in all samples vi) formed cracks are comparable to the TEM findings of GdN.

Raman spectroscopy reveals the occurrence of heavy structural changes. The newly appearing structure is crystalline, but is not in agreement with either bixbyite (Gd_2O_3) or rocksalt (GdN). Raman band at 361 cm^{-1} is found to be the vibrational mode in cubic bixbyite Gd_2O_3 . That mode intensity disappears after high dose ion implantation. The reason for this disappearance is due to partially disturbed crystal structure accompanied by a reduction in the thickness of the remaining crystalline oxide layer. After RTA, the mode appears but shifted to lower wave number due to strain or because of newly formed structures. The decrease in the intensity of this mode after implantation and annealing is studied in detail and found that it is due to the thickness variation of crystalline oxide layer after implantation. The intensity variations of Raman band according to the thickness agrees well with the TEM results.

X-ray diffraction measurements do not show any additional phases but there is a drop in the intensity and broadening of the oxide peaks which also agrees with the thickness variations after high dose ion implantation.

The impact of nitrogen in Gd-O bonding is studied by using x-ray photoelectron spectroscopy. The shift in the Gd and O peak indicates the presence of nitrogen in the layer. The shift in Gd 4d and O 1s levels are according to the implantation dose. That means the sample with high implantation dose or high amount of nitrogen shifts more to lower binding energy.

Layer composition was obtained using Auger electron spectroscopy. By doing sputter depth profiling i obtained a maximum concentration of 11 atom % of nitrogen in Gd₂O₃ layer which was not in complete agreement with the SRIM profile.

The electronic band gap of Gd₂O₃ estimated from O1s plasmon energy loss measurements has found to decrease significantly by the incorporation of nitrogen. Reduction in the valence band and conduction band offset is obtained as a function of fluence. We obtain VB offsets relative to Si of 1.0 eV, 1.2 eV, and 1.5 eV for high, medium, and low fluence implanted samples, respectively. The band gap energy for high fluence implanted sample is obtained as 2.5 ± 0.2 eV. For the high fluence implanted layer conduction band offset yields a value of 0.4 ± 0.2 eV. In addition to the reduction in VB offset the XPS investigations also reveals the reduction in conduction band offset.

7 Summary and Outlook

The ability to integrate crystalline metal oxide dielectric layers into silicon structures can open the way for a variety of novel applications which enhances the functionality and flexibility ranging from high-k replacements in future MOS devices to oxide/silicon/oxide heterostructures for nanoelectronic application in quantum-effect devices. Such an approach will annihilate the risk of re-crystallization, prevent the formation of interfacial layers and enable controllable interface properties. Binary crystalline lanthanide oxides have proved to be a very promising group of dielectrics for epitaxial growth on Si substrates. Molecular beam epitaxy growth is a well-established and high quality method of growing Gd_2O_3 with low lattice mismatch with silicon. The presented work restates the fundamentals of epitaxial growth of gadolinium oxide. But at the same time the presence of oxygen vacancies in rare earth oxides degrades the electrical properties, which can be reduced by nitrogen incorporation. On the other hand, rare-earth nitrides have also been studied for a long time, but only recently it became possible to establish their properties confidently. This group of materials exhibits a versatile set of properties, which in turn have a potentially wide range of applications including electronics, optoelectronics and spintronics. Gadolinium nitride (GdN) is the most thoroughly studied candidate.

Reported results about nitrogen doped Gd_2O_3 with enhanced dielectric properties made to think about nitrogen rich gadolinium oxide i.e. equal amount of nitrogen and oxygen. This idea directed to think about gadolinium oxynitrides. Because Gd_2O_3 and GdN are two well explored materials with completely different properties. Hence the transition between these two materials results in the formation of oxynitrides which was the first stepping stone of this work.

The core part of my PhD thesis is to explore suitable nitridation processes of epitaxially grown Gd_2O_3 on Si (111) substrate. Incorporating nitrogen in high amount into the oxide layer itself is challenging. In this work four different nitridation methods and the properties of nitrogen rich layers were studied in detail. The Gd_2O_3 growth was always performed using the same growth parameters in an MBE system. Nitridation by using N_2O gas ambient during growth does not incorporate enough amount of nitrogen to break Gd-O bond to form Gd-O-N bond. But it shows a shift in Gd_2O_3 (444) peak in XRD measurement which may be due to some strain effects. The next step was to use activated nitrogen as a nitridation source.

Using activated nitrogen and N₂O plasma from the plasma source in MBE system also resulted in the same way like shift in XRD peaks but does not constitute any changes in the layer composition, whereas N₂O plasma results in gadolinium silicide formation also.

Exposed to plasma- activated NH₃ after Gd₂O₃ growth, which also agrees with the previous nitridation results. The main observation was the formation of polycrystalline structures and shift (XRD results) in oxide peaks. Gd 4d and O 1s levels in XPS data confirmed Gd-O bonding.

Fourth nitridation method was nitrogen ion implantation into epitaxially grown Gd₂O₃ on Si (111) substrate which seems to be more promising. Ion implantation parameters were extracted using SRIM software which results to conclude the implantation parameters are energy: 25 keV and three different implantation doses ($2 \cdot 10^{17}$, $1 \cdot 10^{17}$, and $5 \cdot 10^{16}$ atom /cm²) to vary the nitrogen content in the oxide layer.

The nitrogen content in the oxide layer has been altered by changing the implantation dose. The impact of nitrogen in Gd-O bonding is studied by using x-ray photoelectron spectroscopy. The shift in the Gd and O peak indicates the presence of nitrogen in the layer. In addition to that AES-sputter depth profiling gives a maximum nitrogen concentration of ~ 11 atom % in the oxide layer. Raman spectroscopy reveals the occurrence of heavy structural changes. The newly appearing structure is crystalline, but is not in agreement with either *bixbyite* (Gd₂O₃) or *rocksalt* (GdN). The electronic band gap of Gd₂O₃ estimated from O1s plasmon energy loss measurements has found to decrease significantly by the incorporation of nitrogen. Reduction in the valence band and conduction band offset is obtained as a function of dose.

Apart from the above observations there is a lot more that can be performed in the future. The nitrogen distribution in the oxide layer is not uniform. It is really important to achieve a uniform nitrogen distribution in the oxide layer will also give idea about the stoichiometry of gadolinium oxynitride layers. Another important thing is the concentration of nitrogen in the oxide layer. We observed a maximum concentration of 11 atom % in the layer which should also be increased in future work.

References

- [1] G. E. Moore, Cramming More Components onto. Integrated Circuits, *Electronics* 38 (1965) 114.
- [2] M. Bohr, The evolution of scaling from the homogeneous era to the heterogeneous era, In *Proceedings of the Technical Digest of the IEEE International Electron Devices Meeting, Washington, DC, USA, 5–7 December (2011)*.
- [3] K. J. Kuhn, U. Avci, A. Cappellani, M. D. Giles, M. Haverty, S. Kim, R. Kothyar, S. Maraipatrani, D. Nikomov, and C. Pawashe, The ultimate CMOS device and beyond. In *Proceedings of the Technical Digest of the IEEE International Electron Devices Meeting, San Francisco, CA, USA, 10–13 December (2012)* 171.
- [4] Y. S. Chen, H. Y. Lee, P. S. Chen, C. H. Tsai, P. Y. Gu, T. Y. Wu, K. H. Tsai, S. S. Sheu, W. P. Lin, C. H. Lin, P. F. Chiu, W. S. Chen, F. T. Chen, C. Lien, and M. J. Tsai, Challenges and opportunities for HfO_x based resistive random access memory, *Electron Devices Meeting (IEDM), 2011 IEEE International, Washington, DC (2011)* 31.3.1.
- [5] R. D. Clark, Emerging applications for high k materials in VLSI technology, *Materials* 7 (2014) 2913.
- [6] H. J. Osten, A. Laha, M. Czernohorsky, E. Bugiel, R. Dargis, and A. Fissel, Introducing crystalline rare-earth oxides into Si technologies, *Physica Status Solidi (a)* 205 (2008) 695.
- [7] M. Badylevich, S. Shamuilia, V. V. Afanas'ev, A. Stesmans, A. Laha, H. J. Osten, and A. Fissel, Investigation of the electronic structure at interfaces of crystalline and amorphous Gd₂O₃ thin layers with silicon substrates of different orientations, *Applied Physics Letters* 90 (2007) 252101.
- [8] M. C. Lemme, H. D. B. Gottlob, T. J. Echtermeyer, M. Schmidt, H. Kurz, R. Endres, U. Schwalke, M. Czernohorsky, D. Tetzlaff, and H. J. Osten, Complementary metal oxide semiconductor integration of epitaxial Gd₂O₃, *Journal of Vacuum Science and Technology B* 27 (2009) 258.
- [9] J. Robertson, K. Xiong, and S. J. Clark, *Defects in high-k gate dielectric stacks*, NATO Science Series, edited by E. Gusev (Springer, The Netherlands), 2006.
- [10] K. Xiong, J. Robertson, and S. J. Clark, Passivation of oxygen vacancy states in HfO₂ by nitrogen, *Journal of Applied Physics* 99 (2006) 44105.

- [11] K. Tse, D. Liu, K. Xiong, and J. Robertson, Oxygen vacancies in high-k oxides, *Microelectronic Engineering* 84 (2007) 2028.
- [12] M. R. Visokay, J. J. Chambers, A. L. P. Rotondaro, A. Shanware, and L. Colombo, Application of HfSiON as a gate dielectric material, *Applied Physics Letters* 80 (2002) 3183.
- [13] D. G. Park, H. J. Cho, I. S. Yeo, J. S. Roh, and J. M. Hwang, Boron penetration in p+ polycrystalline-Si/Al₂O₃/Si metal–oxide–semiconductor system, *Applied Physics Letters* 77 (2000) 2207.
- [14] L. Miotti, C. Driemeier, F. Tatsch, C. Radtke, V. Edon, M. C. Hugon, O. Voldoire, B. Agius, and I. J. R. Baumvol, Atomic transport in LaAlO₃ films on Si induced by thermal annealing, *Electrochemical and Solid State Letters* 9 (2006) F49.
- [15] S. Jeon, C. J. Choi, T. Y. Seong, and H. Hwang, Electrical characteristics of ZrO_xN_y prepared by NH₃ annealing ZrO₂, *Applied Physics Letters* 79 (2001) 245.
- [16] S. Sayan, N. V. Nguyen, J. Ehrstein, J. J. Chambers, M. R. Visokay, M. A. Quivedo-Lopez, L. Colombo, D. Yoder, I. Levin, D. A. Fischer, M. Paunesco, O. Celik, and E. Garfunkel, Effect of nitrogen on band alignment in HfSiON gate dielectrics, *Applied Physics Letters* 87 (2005) 212905.
- [17] B. Sen, H. Wong, B. L. Yang, A. P. Huang, P. K. Chu, V. Filip, and C. K. Sarkar, Nitrogen incorporation into hafnium oxide films by plasma immersion ion implantation, *Japanese Journal of Applied Physics* 46 (2007) 3234.
- [18] C. H. Choi, S. J. Rhee, T. S. Jeon, N. Lu, J. H. Sim, R. Clark, M. Niwa, and D. L. Kwong, Thermally stable CVD HfO_xN_y advanced gate di-electrics with poly-Si gate electrode, *Electron Devices Meeting, 2002. IEDM '02, San Francisco, CA, USA* (2002) 857.
- [19] X. B. Lu, Z. G. Liu, Y. P. Wang, Y. Yang, X. P. Wang, H. W. Zhou, and B. Y. Nguyen, Structure and dielectric properties of amorphous LaAlO₃ and LaAlO_xN_y films as alternative gate dielectric materials, *Journal of Applied Physics* 94 (2003) 1229.
- [20] C. S. Kang, H. J. Cho, K. Onishi, R. Nieh, R. Choi, S. Gopalan, S. Krishnan, J. H. Han, and J. C. Lee, Bonding states and electrical properties of ultrathin HfO_xN_y gate dielectrics, *Applied Physics Letters* 81 (2002) 2593.
- [21] A. R. Chaudhuri, A. Fissel, and H. J. Osten, Investigation of band offsets and dc leakage properties of nitrogen doped epitaxial Gd₂O₃ thin films on Si, *Journal of Applied Physics* 113 (2013) 184108.

- [22] F. Natali, N. O. V. Plank, J. Galipaud, B. J. Ruck, H. J. Trodahl, F. Semond, S. Sorieul, and L. Hirsch, Epitaxial growth of GdN on silicon substrate using an AlN buffer layer, *Journal of Crystal Growth* 312 (2010) 3583.
- [23] H. J. Trodahl, A. R. H. Preston, J. Zhong, B. J. Ruck, N. M. Strickland, C. Mitra and W. R. L. Lambrecht, Ferromagnetic redshift of the optical gap in GdN, *Physical Review B* 76 (2007) 85211.
- [24] P. Wachter and E. Kaldis, Magnetic interaction in GdN and $\text{GdN}_{1-x}\text{O}_x$, *Journal of Magnetism and Magnetic Materials* 15-18 (1980) 305.
- [25] J. C. Wang, Y. R. Ye, Y. H. Wu, C. F. Ai, and W. F. Tsai, *International Journal of Nanotechnology* 11 (2014) 135.
- [26] A. R. Chaudhuri, A. Fissel, V. R. Archakam, and H. J. Osten, Improving dielectric properties of epitaxial Gd_2O_3 thin films on silicon by nitrogen doping, *Applied Physics Letters* 102 (2013) 22904.
- [27] B. Sen, B. L. Yang, H. Wong, C. W. Kok, M. K. Bera, P. K. Chu, A. Huang, K. Kakushima, and H. Iwai, Electrical Stability Improvement for Lanthanum Oxide Films by Nitrogen Incorporation using Plasma Immersion Ion Implantation, *Electron Devices and Solid-State Circuits EDSSC 2007* (2007) 637.
- [28] <http://geology.com/articles/rare-earth-elements/>.18. Febr. 2017 19:32:27 GMT
- [29] G. V. Samsonov (Ed.), *The oxide handbook*, second ed., IFI/Plenum, New York, 1982.
- [30] J. Robertson, and K. Xiong, *Electronic structure and band offsets of lanthanide oxides*, Springer-Verlag Berlin Heidelberg, 2007.
- [31] G. R. Choppin, *Chemical properties of the rare earth elements*. Ch. 1. Elsevier, Amsterdam, 1989.
- [32] M. Foëx, and J. P. Traverse, Investigations about crystalline transformation in rare earths sesquioxides at high temperatures, *Rev. Int. Hautes Temp. Refract* 3 (1966) 429.
- [33] H. Bergmann (Ed.), *Gmelin Handbuch der Anorganischen Chemie, Seltenerdelemente, Teil C1*, Springer-Verlag, Berlin, p.85, 1974.
- [34] L. Eyring, *The binary rare earth oxides*, in *handbook of physics and chemistry of rare earths*, North Holland, Amsterdam, 1979.
- [35] A. F. Wells, *Structural inorganic chemistry*. Oxford Science Publications, Oxford, fifth ed., 1984.

-
- [36] G. Adachi, and N. Imanaka, The binary rare earth oxides, *Chemical Reviews* 98 (1998) 1479.
- [37] H. S. Momose, S. Nakamura, T. Ohguro, T. Yoshitomi, E. Morifuji, T. Morimoto, Y. Katsumata, and H. Iwai, Study of the manufacturing feasibility of 1.5-nm direct-tunneling gate oxide MOSFETs: uniformity, reliability, and dopant penetration of the gate oxide, *IEEE Transaction on Electron Devices* 45 (1998) 691.
- [38] J. L. Zhang, J. S. Yuan, Y. Ma, and S. Oates, Modeling of direct tunneling and surface roughness effects on C–V characteristics of ultra-thin gate MOS capacitors, *Solid State Electronics* 45 (2001) 373.
- [39] H. H. Ko, L. B. Chang, M. J. Jeng, P. Y. Kuei, and K. Y. Horng, Properties of thermal gadolinium oxide films on silicon, *Japanese Journal of Applied Physics* 44 (2005) 3205.
- [40] A. K. Jonsson, G. A. Niklasson, and M. Veszelei, Electrical properties of ZrO₂ thin films, *Thin Solid Films* 402 (2002) 242.
- [41] D. O. Lee, P. Roman, C. T. Wu, P. Mumbauer, M. Brubaker, R. Grant, and J. Ruzyllo, Mist deposited high-k dielectrics for next generation MOS gates, *Solid-State Electronics* 46 (2002) 1671.
- [42] Y. C. Quan, J. E. Lee, H. Kang, Y. Roh, D. Jung, and C. W. Yang, Formation of reliable HfO₂/HfSi_xO_y gate-dielectric for metal-oxide-semiconductor devices, *Japanese Journal of Applied Physics* 41 (2002) 6904.
- [43] Y. Zhang, A. Navrotsky, H. Li, L. Li, L. L. Davis, and D. M. Strachan, Energetics of dissolution of Gd₂O₃ and HfO₂ in sodium alumino-borosilicate glasses, *Journal of Non-Crystal Solids* 296 (2001) 93.
- [44] L. Kang, B. H. Lee, W. J. Qi, Y. Jeon, R. Nich, S. Gopalan, K. Onishi, and J. C. Lee, Electrical characteristics of highly reliable ultrathin hafnium oxide gate dielectric, *IEEE Electron Device Letters* 21 (2000) 181.
- [45] A. Chin, Y. H. Wu, S. B. Chen, C. C. Liao, and W. J. Chen, High quality La₂O₃ and Al₂O₃ gate dielectrics with equivalent oxide thickness 5-10 angstrom, *Symposium on VLSI Technology* (2000) 16.
- [46] J. K. Yang, M. G. Kang, and H. H. Park, Interface control of Gd₂O₃/GaAs system using pre-deposition of Gd metal on GaAs substrate with native oxides, *Thin Solid Films* 420-421 (2002) 571.

- [47] H. J. Osten, J. P. Liu, H. J. Müssig, and P. Zaumseil, Epitaxial, high-K dielectrics on silicon: the example of praseodymium oxide, *Microelectronic Reliability* 41 (2001) 991.
- [48] V. Mikhelashvili, G. Eisenstein, and F. Edelmann, Characteristics of electron-beam-gun-evaporated Er_2O_3 thin films as gate dielectrics for silicon, *Journal of Applied Physics* 90 (2001) 5447.
- [49] V. A. Rozhkov, A. Y. Trusova, and I. G. Berezhnoy, Silicon MIS structures using samarium oxide films, *Thin Solid Films* 325 (1998) 151.
- [50] P. Delugas, and V. Fiorentini, Dielectric properties of two phases of crystalline lutetium oxide, *Microelectronics Reliability* 45 (2005) 831.
- [51] W. Cai, S. E. Stone, J. P. Pelz, L. F. Edge, and D. G. Schlom, Conduction band energies and hot-electron transport characteristics of epitaxial $\text{Sc}_2\text{O}_3 / \text{Si}$ (111) studied by ballistic electron emission microscopy and internal photoemission, *Applied Physics Letters* 91 (2007) 42901.
- [52] G. Adachi, N. Imanaka, and Z. C. Kang, *Binary rare earth oxides*, Kluwer Academic Publishers, New York., 2004.
- [53] J. Wang, T. Ji, Y. Zhu, Z. Fang, and W. Ren, Band gap and structure characterization of Tm_2O_3 films, *Journal of Rare Earths* 30 (2012) 233.
- [54] A. Laha, H. J. Osten, and A. Fissel, Impact of Si substrate orientations on electrical properties of crystalline Gd_2O_3 thin films for high-K application, *Applied Physics Letters* 89 (2006) 143514.
- [55] A. Bartos, K. P. Lieb, M. Uhrmacher, and D. Wiarda, Refinement of atomic positions in bixbyite oxides using perturbed angular correlation spectroscopy, *Acta Crystallographica Section B Structural Science* 49 (1993) 165.
- [56] F. Natali, B. J. Ruck, N. O. V. Plank, H. J. Trodahl, S. Granville, C. Meyer, and W. R. L. Lambrecht, Rare-earth mononitrides, *Progress in Materials Science* 58 (2013) 1316.
- [57] J. P. Dismukes, W. M. Yim, J. J. Tietjen, and R. E. Novak, Vapor deposition of semiconducting mononitrides of scandium, yttrium. and the rare-earth elements, *RCA Review* 31 (1970) 680.
- [58] H. A. Eick, N. C. Baenziger, and L. Eyring, The Preparation, Crystal Structure and Some Properties of SmN , EuN and YbN , *Journal of the American Chemical Society* 78 (1956) 5987.

- [59] R. Marchand, K. A. Gschneidner, and L. Eyring, Handbook on the physics and chemistry of rare earths, Amsterdam, Elsevier, 1998, p.51.
- [60] M. A. Scarpulla, C. S. Gallinat, S. Mack, J. S. Speck, and A. C. Gossard, GdN (111) heteroepitaxy on GaN (0 0 0 1) by N₂ plasma and NH₃ molecular beam epitaxy, Journal of Crystal Growth 311 (2009) 1239.
- [61] H. Yoshitomi, S. Kitayama, T. Kita, O. Wada, M. Fujisawa, and H. Ohta, Optical and magnetic properties in epitaxial GdN thin films, Physical Review B 83 (2011) 155202.
- [62] O. Vogt, and K. Mattenberger, Handbook on the physics and chemistry of rare earths, Elsevier Science, Amsterdam, 1993.
- [63] R. A. Cutler, and A. W. Lawson, Synthesis and magnetic behavior of GdN, Journal of Applied Physics 46 (1975) 2739.
- [64] F. Leuenberger, A. Parge, W. Felsch, K. Fauth, and M. Hessler, GdN thin films: Bulk and local electronic and magnetic properties, Physical Review B 72 (2005) 14427.
- [65] S. Granville, B. J. Ruck, F. Budde, A. Koo, D. J. Pringle, and F. Kuchler, Semiconducting ground state of GdN thin films, Physical Review B 73 (2006) 235335.
- [66] R. Vidyasagar, S. Kitayama, H. Yoshitomi, T. Kita, T. Sakurai, and H. Ohta, Study on spin-splitting phenomena in the band structure of GdN, Applied Physics Letters 100 (2012) 232410.
- [67] H. R. Child, M. K. Wilkinson, J. W. Cable, W. C. Koehler, and E. O. Wollan, Neutron diffraction investigation of the magnetic properties of compounds of rare-earth metals with group V anions, Physical Review 131 (1963) 922.
- [68] P. Wachter, Physical properties of stoichiometric GdN single crystals, Results in Physics 2 (2012) 90.
- [69] K. Wörhoff, L. T. H. Hilderink, A. Driessen, and P. V. Lambeck, Silicon oxynitride: A versatile material for integrated optics applications, Journal of The Electrochemical Society 149(8) (2002) F85.
- [70] G. D. Wilk, R. M. Wallace, and J. M. Anthony, High- κ gate dielectrics: Current status and materials properties considerations, Journal of Applied Physics 89 (2001) 5243.
- [71] S. Guha, E. P. Gusev, H. O. Schmidt, M. C. Copel, L. A. Ragnarsson, N. A. Bojarczuk, and P. Ronsheim, High temperature stability of Al₂O₃ dielectrics in silicon: Interfacial metal diffusion and mobility degradation, Applied Physics Letters 81 (2002) 2956.

- [72] T. L. Felmlee, and L. Eyring, On the ternary system Samarium-Nitrogen-Oxygen and the question of lower oxides of Samarium, *Inorganic Chemistry* 7 (1968) 660.
- [73] Y. R. Ye , Y. H. Wu , J. C. Wang, and C. S. Lai, Robust nitrogen plasma immersion ion implantation treatment on gadolinium oxide resistive switching random access memory, *Nanoelectronics Conference (INEC), 2013 IEEE 5th International, Singapore (2013)* 300.
- [74] M. Eckert, Max von Laue and the discovery of X-ray diffraction in 1912, *Annalen der Physik* 524 (2012) A83.
- [75] W. H. Bragg, and W. L. Bragg, The reflection of X-rays by crystals, *Proceedings of the Royal Society A* 88 (1913) 428.
- [76] M. Birkholz, *Thin Film Analysis by X-Ray Scattering*, WILEY-VCH Verlag GmbH&Co.KGaA, 2005.
- [77] S. Terada, H. Murakami, and K. Nishihagi (Ed.), *Thickness and density measurement for new materials with combined X-ray technique*, 2001.
- [78] C. Wyon, D. Delille, J. P. Gonchond, F. Heider, L. Kwakman, S. Marthon, I. Mazor, A. Michallet, D. Muyard, L. P. Gallice, J. C. Royer, and A. Tokar, In-line monitoring of advanced microelectronic processes using combined X-ray techniques, *Thin Solid Films* 84 (2004) 450.
- [79] H. Kiessig, Interferenz von Röntgenstrahlen an dünnen Schichten, *Annalen der Physik* 10 (1931) 769.
- [80] C. Buzea, and K. Robbie, State of the art in thin film thickness and deposition rate monitoring sensors, *Reports on Progress in Physics* 68 (2005) 385.
- [81] A. Einstein, Über einen die Erzeugung und Verwandlung des Lichtes betreffenden heuristischen Gesichtspunkt, *Annalen der Physik* 17(6) (1905) 132.
- [82] C. C. Chusuei, and D. W. Goodman, *X-Ray photoelectron Spectroscopy*, third ed., *Encyclopedia of Physical Science and Technology*, 2002.
- [83] J. Bergengren, Über die Röntgenabsorption des phosphors, *Zeitschrift für Physik* 3 (1920) 247.
- [84] A. E. Lindh, Zur Kenntnis des K-Röntgenabsorptionsspektrums von Chlor., *Zeitschrift für Physik* 6 (1921) 303.
- [85] D. J. O'connor, B. A. Sexton, and R. St. C. Smart (Ed.), *Surface analysis method in materials science*, Springer-Verlag, Heidelberg, 1992.

- [86] J. F. Watts, and J. Wolstenholme, *An Introduction to Surface Analysis by XPS and AES*, Wiley-VCH Verlag GmbH, 2005.
- [87] L. E. Davis, N. C. MacDonald, P. W. Palmberg, G. E. Riach, and R. E. Weber, *Handbook of Auger Electron Spectroscopy*, second ed., Physical Electronics Industries Inc., Eden Prairie, MN, 1976.
- [88] *Handbook of analytical methods for materials*, Materials evaluation and engineering Inc, Plymouth, MN 55441.
- [89] C. V. Raman, and K. S. Krishnan, A new type of secondary radiation *Nature*, *Nature* 121 (1928) 501.
- [90] G. Landsberg, and L. Mandelstam, Eine neue Erscheinung bei der Lichtzerstreuung in Krystallen, *Naturwissenschaften* 16 (1928) 557.
- [91] D. A. Skoog, F. J. Holler, and S. R. Crouch, *Principles of instrumental analysis*, sixth ed., Cengage Learning, 2006.
- [92] H. H. Willard, L. L. Meritt Jr., J. J. Dean, and F. A. Settle Jr., *Instrumental methods of analysis*, seventh ed., CBS Publisher & Distributors, New Delhi, 1988.
- [93] E. Smith, and G. Dent, *Modern Raman spectroscopy: a practical approach*, John Wiley & Sons, England, 2005.
- [94] C. Le Luyer, A. Garcia-Murillo, E. Bernstein, and J. Mugnier, Waveguide Raman spectroscopy of sol-gel Gd_2O_3 thin films, *Journal of Raman Spectroscopy* 34 (2003) 234.
- [95] S. V. Gaisler, O. I. Semenova, R. G. Sharafutdinov, and B. A. Kolesov, Analysis of Raman spectra of amorphous-nanocrystalline silicon films, *Physics of the Solid State* 46 (2004) 1528.
- [96] J. Ferraro, *Introductory Raman Spectroscopy*, second ed., Academic Press, 2003.
- [97] P. Vandenabeele, *Practical Raman Spectroscopy - An Introduction*, John Wiley & Sons, 2013.
- [98] P. Hawkes, Recent advances in electron optics and electron microscopy, *Ann. Fondation Louis de Broglie* 29-1 (2004).
- [99] E. Ruska, *The development of the electron microscope and of electron microscopy*, 1986.
- [100] F. Haguenu, P. W. Hawkes, J. L. Hutchison, B. S. Jeunemaître, G. T. Simon, and D. B. Williams, Key events in the history of electron microscopy, *Microscopy and Microanalysis* 9 (2003) 96.
- [101] M. Knoll, and E. Ruska, Das Elektronenmikroskop, *Zeitschrift für Physik* 78 (1932) 318.

- [102] D. B. Williams, and C. B. Carter, *Transmission Electron Microscopy*, Springer Science+Business Media, LLC, 2009.
- [103] P. J. Eaton, and P. West, *Atomic force microscopy*, Oxford and New York Oxford University Press, 2010.
- [104] T. L. Alford, L. C. Feldman, and J. W. Mayer, *Fundamentals of nanoscale film analysis*, New York and London Springer, 2007.
- [105] W. R. Bowen, and N. Hilal, *Atomic force microscopy in process engineering: An introduction to AFM for improved processes and products*, first ed., Butterworth-Heinemann / IChemE series, Amsterdam, 2009.
- [106] S. N. Magonov (Hrsg.), and M.-H Whangbo (Hrsg.), *Surface analysis with STM and AFM: Experimental and theoretical aspects of image analysis*, Weinheim and New York VCH, 1996.
- [107] D. K. Schroder, *Semiconductor material and device characterization*, third ed., IEEE Press and Wiley, 2006.
- [108] M. A. Herman, W. Richter, and H. Sitter, *Epitaxy Physical principles and Technical implementation*, springer -Verlag Berlin Heidelberg, 2004.
- [109] J. R. Arthur, *Molecular beam epitaxy*, *Surface Science* 500 (2002) 189.
- [110] M. A. Herman, and H. Sitter, *Molecular Beam Epitaxy Fundamentals and Current Status*, springer -Verlag Berlin Heidelberg, 1996.
- [111] M. Volmer, and A. Weber, *Keimbildung in übersättigten Gebilden*, *Zeitschrift für Physikalische Chemie* 119 (1926) 277.
- [112] F. C. Frank, and J. H. van der Merwe, *One-Dimensional Dislocations. I. Static Theory*, In *Proceedings of the Royal Society of London. Series A, Mathematical and Physical Sciences* 198 (1949) 205.
- [113] I. N. Stranski, and L. Krastanov, *Zur Theorie der Orientierten Ausscheidung von Ionenkristallen aufeinander*, *Sitzungsber. Akad. Wiss. Wien. Math.-Naturwiss* 146 (1938) 797.
- [114] G. Biasiol, and L. Sorba (Ed.), *Molecular beam epitaxy: principles and applications*, Edizioni ETS, Pisa, Italy, 2001.
- [115] M. Nolan, S. Grigoleit, D. C. Sayle, S. C. Parker, and G. W. Watson, *Density functional theory studies of the structure and electronic structure of pure and defective low index surfaces of ceria*, *Surface Science* 576 (2005) 217.

- [116] G. Seguini, E. Bonera, S. Spiga, G. Scarel, and M. Fanciulli, Energy-band diagram of metal/Lu₂O₃/silicon structures, *Applied Physics Letters* 85 (2004) 5316.
- [117] J. Kwo, M. Hong, A. R. Kortan, K. L. Queeny, Y. J. Chabal, R. L. Opila, D. A. Müller, S. N. G. Chu, B. J. Sapteja, T. S. Lay, J. P. Mannaerts, T. Boone, H. W. Krautter, J. J. Krajewski, A. M. Sergnt, and J. M. Rosamilia, Properties of high κ gate dielectrics Gd₂O₃ and Y₂O₃ for Si, *Journal of Applied Physics* 89 (2001) 3920.
- [118] A. Fissel, H. J. Osten, and E. Bugiel, Towards understanding epitaxial growth of alternative high-k dielectrics on Si(001): Application to praseodymium oxide, *Journal of Vacuum Science and Technology B* 21 (2003) 1765.
- [119] "Semi" SemiSource 2006: A supplement to Semiconductor International. Reference Section: How to Make a Chip. Adapted from Design News. Reed Electronics Group., 2005.
- [120] Michiharu Tabe, UV ozone cleaning of silicon substrates in silicon molecular beam epitaxy, *Applied Physics Letters* 45 (1984) 1073
- [121] M. Czernohorsky, E. Bugiel, H. J. Osten, A. Fissel, and O. Kirfel, Impact of oxygen supply during growth on the electrical properties of crystalline Gd₂O₃ thin films on Si (001), *Applied Physics Letters* 88 (2006) 152905.
- [122] J. X. Wang, A. Laha, A. Fissel, D. Schwendt, R. Dargis, T. Watahiki, R. Shayduk, W. Braun, T. M. Liu, and H. J. Osten, Crystal structure and strain state of molecular beam epitaxial grown Gd₂O₃ on Si (1 1 1) substrates: a diffraction study, *Semiconductor Science and Technology* 24 (2009) 4.
- [123] H. J. Osten, M. Czernohorsky, R. Dargis, A. Laha, D. Kühne, E. Bugiel, and A. Fissel, Integration of functional epitaxial oxides into silicon: From high-K application to nanostructures, *Microelectronic Engineering* 84 (2007) 2222.
- [124] A. Laha, H. J. Osten, and A. Fissel, Influence of interface layer composition on the electrical properties of epitaxial Gd₂O₃ thin films for high-K application, *Applied Physics Letters* 90 (2007) 113508.
- [125] J. F. Moulder, W. F. Stickle, P. E. Sobol, and K. D. Bomben, *Handbook of X-ray photoelectron spectroscopy*, Eden Prairie, MN Physical Electronics, 1995.
- [126] R. S. Becker, J. A. Golovchenko, E. G. Mcrae, and B. S. Swartzentruber, Tunneling images of atomic steps on the Si (111) 7 x 7 surface, *Physical Review Letter* 55 (1985) 2028.

- [127] G. Niu, B. Vilquin, N. Baboux, C. Plossu, L. Becerra, G. St. Groins, and G. Hollinger, Growth temperature dependence of epitaxial Gd_2O_3 films on $\text{Si}(1\ 1\ 1)$, *Microelectronic Engineering* 86 (2009) 1700.
- [128] H. D. B. Gottlob, T. Echtermeyer, T. Mollenhauer, J. K. Efavi, M. Schmidt, T. Wahlbrink, M. C. Lemme, H. Kurz, M. Czernohorsky, E. Bugiel, H. J. Osten, and A. Fissel, CMOS Integration of Epitaxial Gd_2O_3 High-K Gate Dielectrics, *Solid State Electronics* 50 (2006) 979.
- [129] L. Liu, J. P. Xu, F. Ji, J. X. Chen, and P. T. Lai, Improved memory characteristics by NH_3 -nitrided GdO as charge storage layer for nonvolatile memory applications, *Applied Physics Letters* 101 (2012) 33501.
- [130] R. B. Beck, and A. Jakubowski, Ultrathin oxynitride films for CMOS technology, *Journal of Telecommunications and Information Technology* 1 (2004) 62.
- [131] L. Pauling, *Nature of the chemical bond*, 1940.
- [132] K. A. Ellis, and R. A. Buhrman, Nitrous oxide (N_2O) processing for silicon oxynitride gate dielectrics, *IBM Journal of Research and Development* 43 (1999) 287.
- [133] C. D. krzeminski, Modelling of silicon oxynitridation by nitrous oxide using the reaction rate approach, *Journal of Applied Physics* 114 (2013) 224501.
- [134] A. Fissel, D. Kühne, E. Bugiel, and H. J. Osten, Cooperative solid-vapor-phase epitaxy: An approach for fabrication of single crystalline insulator/Si/insulator nanostructures, *Applied Physics Letters* 88 (2006) 153105.
- [135] G. Jaksa, B. Stefane, and J. Kovac, XPS and AFM characterization of aminosilanes with different numbers of bonding sites on a silicon wafer, *Surface and Interface Analysis* 45 (2013) 1709.
- [136] N. Kawada, M. Ito, and Y. Saito, Thermal stability of lanthanum oxynitride ultrathin films deposited on silicon substrates, *Japanese Journal of Applied Physics* 45 (2006) 9197.
- [137] M. L. Campbell, Temperature dependent rate constants for the reactions of gas phase lanthanides with N_2O , *Journal of Chemical Physics* 111 (1999) 562.
- [138] F. W. Doss, C. Biloiu, and E. scime, Nitrogen plasma source for molecular beam epitaxy of gallium nitride. Dept .of Phys. west Virginia Unv.WV26506.
- [139] S. Auffret, J. Pierre, B. L. Andron, R. Madar, E. Houssay, D. Schmitt, and E. Siaud, Magnetic properties versus crystal structure in heavy rare-earth silicides RSi_{2-x} , *Physica B* 173 (1991) 265.

- [140] Yibin Xu, Masayoshi Yamazaki, and Pierre Villars, Inorganic Materials Database for Exploring the Nature of Material, Japanese Journal of Applied Physics 50 (2011) 11RH02
- [141] R. Marchand, A. Jayaweera, P. Verdier, and J. Lang, Preparation and characterization of new oxynitrides in Ln-Si-ON system-melilites $\text{Ln}_2\text{Si}_3\text{O}_3\text{N}_4$ and cuspidines $\text{Ln}_4\text{Si}_2\text{O}_7\text{N}_2$, Comptes Rendus Hebdomadaires Des Seances De L Academie Des Sciences Serie C 283 (1976) 675.
- [142] F. Canepa, S. Cirafici, F. Merlo, and A. Palezona, Electrical resistivity measurements on some R_5Si_3 phases: R = Gd, Tb, Yb, Lu and Y, Journal of Magnetic Materials 118 (1993) 182.
- [143] K. D. Hirschman, Silicon processes: ion implantation ([http://web.utk.edu/~prack/Thin films/implant-1.pdf](http://web.utk.edu/~prack/Thin%20films/implant-1.pdf)).
- [144] S. B. Felch, M. I. Current, and M. C. Taylor, Ion implantation for semiconductor devices: The largest use of industrial accelerators, Proceedings of PAC2013, Pasadena, CA USA (2013) 740.
- [145] J. H. Liang, and K. Y. Liao, Energy losses of ions implanted in matter, Journal of Materials Research 11 (1996) 2876.
- [146] S. M. Sze, Semiconductor devices, physics and technology, Wiley, 2nd ed., 2001.
- [147] J. P. Biersack, and K. G. Haggmark, A Monte Carlo computer program for the transport of energetic ions in amorphous targets, Nuclear Instruments and Methods 174 (1980) 257.
- [148] G.H. Kinchin, and R. S. Pease, The displacement of atoms in solids by radiation, Reports on Progress in Physics 18 (1955) 1.
- [149] P. Sigmund, A note on integral equations of the kinchin-pease type, Radiation Effects 1 (1969) 15.
- [150] M. J. Norgett, M. T. Robinson, and I. M. Torrens, A proposed method of calculating displacement dose rates, Nuclear Engineering Design 33 (1974) 50.
- [151] J. F. Ziegler, J. P. Biersack, M. D. Ziegler, SRIM- The stopping and range of ions in matter: www.srim.org, 2008.
- [152] K. Ueno, T. Kikkawa, and K. Tokashiki, Reactive ion etch characteristics of silicon oxynitride formed plasma enhanced chemical vapor deposition, Journal of Vacuum Science & Technology B13 (1995) 1447.

- [153] J. Narayan, O. W. Holland, R. E. Eby, J. J. Wortman, V. Ozguz, and G. A. Rozgonyi, Rapid thermal annealing of arsenic and boron-implanted silicon, *Applied Physics Letters* 43 (1983) 957.
- [154] J. Narayan, and O. W. Holland, Rapid thermal annealing of ion-implanted semiconductors, *Journal of Applied Physics* 56 (1984) 2913.
- [155] M. Czernohorsky, D. Tetzlaff, E. Bugiel, R. Dargis, H. J. Osten, H. D. B Gottlob, M. Schmidt, M. C. Lemme, and H. Kurz, Stability of crystalline Gd₂O₃ thin films on silicon during rapid thermal annealing, *Semiconductor Science and Technology* 23 (2008) 35010.
- [156] A. Joseph, D. Tetzlaff, J. Schmidt, R. Böttger, T. F. Wietler, H. J. Osten, Formation and properties of high-dose nitrogen implanted epitaxially grown Gd₂O₃ on silicon, *Journal of Applied Physics* 120 (2016) 144103.
- [157] W. R. McKenzie, P. R. Munroe, F. Budde, B. J. Ruck, S. Granville, and H. J. Trodhal, TEM characterisation of GdN thin films, *Current Applied Physics* 6 (2006) 407.
- [158] S. Granville, C. Meyer, A. R. H. Preston, B. M. Ludbrook, B. J. Ruck, H. J. Trodahl, T. R. Paudel, and W. R. L. Lambrecht, Vibrational properties of rare-earth nitrides: Raman spectra and theory, *Physical Review B* 79 (2009) 54301.
- [159] M. C. Poon, C. W. Kok, H. Wong, and P. J. Chan, Bonding structures of silicon oxynitride prepared by oxidation of Si-rich silicon nitride, *Thin Solid Films* 462-463 (2004) 42.
- [160] M. Kim, and H. J. Osten, X-ray photoelectron spectroscopic evaluation of valence band offsets for strained Si_{1-x}Ge_x, Si_{1-y}C_y, and Si_{1-x-y}Ge_xC_y on Si(001), *Applied Physics Letters* 70 (1997) 2702.
- [161] R. Grillen, S. J. Clark, and J. Robertson, Nature of the electronic band gap in lanthanide oxides, *Physical Review B* 87 (2013) 125116.
- [162] F. Arai, S. Kimura, and M. Ikezawa, Resonant photoemission study of electronic structure of rare-earth sesquioxides, *Journal of the Physical Society of Japan* 67 (1998) 225.
- [163] G. Shang, P. W. Peacock, and J. Robertson, Stability and band offsets of nitrogenated high-dielectric-constant gate oxides, *Applied Physics Letters* 84 (2004) 106.
- [164] F. G. Bell, and L. Ley, Photoemission study of SiO_x (0≤x≤2) alloys, *Physical Review B* 37 (1988) 8383.

- [165] A. Laha, E. Bugiel, H. J. Osten, and A. Fissel, Crystalline ternary rare earth oxides with capacitance equivalent thickness below 1 nm for high-k application, *Applied Physics Letters* 88 (2006) 172107.
- [166] H. S. Jung, H. K. Kim, J. H. Kim, S. J. Won, D. Y. Cho, J. Lee, S. Y. Lee, C. S. Hwang, J.M. Park, W. H. Kim, M. W. Song, N. I. Lee, and S. Heo, Electrical and bias temperature instability characteristics of n-type field-effect transistors using HfO_xN_y gate dielectrics, *Journal of The Electrochemical Society* 157 (2010) G121.
- [167] T. Mizutani, Preferential sputtering of oxygen from SiO_2 by low-energy ion beam and neutral beam bombardment, *Japanese Journal of Applied Physics* 30 (1991) L628.

Publication

1. A. Joseph, D. Tetzlaff, J. Schmidt, R. Böttger, T. F. Wietler, H. J. Osten: Formation and properties of high-dose nitrogen implanted epitaxially grown Gd₂O₃ on silicon, Journal of Applied Physics 120 (2016) 144103.

Conference presentations

1. A. Joseph, D. Tetzlaff, J. Schmidt, R. Böttger, T.F. Wietler, H.J. Osten: Properties of high-dose nitrogen implanted epitaxially grown Gd₂O₃ on silicon, German MBE-Workshop, Garching, Germany, 13- 14 October 2016
2. A. Joseph, D. Tetzlaff, J. Schmidt, R. Böttger, T.F. Wietler, H. J. Osten: Properties of high-dose nitrogen implanted epitaxially grown Gd₂O₃ on silicon, EMN Meeting on Epitaxy, Budapest, Hungary, 04.-08 September 2016.

Acknowledgement

To acquire my dream there are bunches of people who gave their hands as support. Initially i thank to Hannover School of Nanotechnology for giving this opportunity and funding.

I would like to express my sincere gratitude and earnest appreciation to my mentor and my supervisor Prof. Dr. H. J. Osten. He guided me with full of patience and support throughout this three years of my PhD. He molded me always with corrections and provided right solutions whenever I stopped in my way.

Next i would like to thank to my Co-supervisor and Co-referee Prof. Dr. Tobias F. Wietler for his immense support and care throughout the journey. I would also like to express my heart filled thanks to my Co-referee Prof. Dr. Jan Schmidt for his remarks and support.

My sincere thanks to Dr. Roman Böttger and Dr. Gerhard Lilienkamp for their large support in processing and characterization steps to consummate my dream.

Next I thank to Prof. Dr. Andreas Fissel for investing some energy to clear my doubts. Likewise, I express my heart filled thanks to all my colleagues Dr. Eberhard Bugiel, Dr. Ayan Roy Chaudhuri, Dr. Dominik Schwendt, Dr. Dominic Tetzlaff, Dr. Jan Krügener, Dipl.-Ing. Jan Schmidt, Dipl. -Ing. Matthias Möllers, MSc. Andreas Grimm and MSc. Gustav Wetzl. My special thanks to Dr. Fritz Schulze Wischeler.

Also, my sincere thanks to Sabine Galle, Tanja Helmbrecht, Andrea Lissel, Guido Glowatzki, Bernd Koch, Hartmut Schwarz and Detlef Zech for all aides in the institute.

Last but not the least heaps of gratitude to Sigrid Guttner and family for always stand with me and being a part of my family. Lots and Lots of thanks to all members of my family and a special thanks to my husband and parents for your valuable love and support as usual.

Curriculum Vitae

| | |
|----------------|--|
| Name | Anit Joseph |
| Date of birth | 27.05.1989 |
| Place of birth | Thrissur, Kerala, India |
| Marital status | Married |
| year 2013 | Leibniz Universität Hannover, Institut für Materialien und Bauelemente der Elektronik |
| 2010-2012 | Masters in Electronics, BPC College Piravom, M.G. University |
| 2007-2010 | Bachelors in Electronics, IHRD college Vadakkenchery, Calicut University |
| 2005-2007 | Higher Secondary (Plus two), GHSS Pattikkad, Kerala |
| 2005 | SSLC (10th std.), St.Clar's CGHSS, Thrissur, Kerala |

